DOKUZ EYLÜL UNIVERSITY
GRADUATE SCHOOL OF NATURAL AND APPLIED SCIENCES

OPTIMIZING THE DESIGN PARAMETERS OF CONDENSING BOILER BY NUMERICAL, EXPERIMENTAL AND ARTIFICIAL NEURAL NETWORKS METHODS

by
Hasan AVCI

September, 2023
İZMİR

OPTIMIZING THE DESIGN PARAMETERS OF CONDENSING BOILER BY NUMERICAL, EXPERIMENTAL AND ARTIFICIAL NEURAL NETWORKS METHODS

A Thesis Submitted to the
Graduate School of Natural and Applied Sciences of Dokuz Eylül University
In Partial Fulfillment of the Requirements for the Degree of Doctor of Philosophy in Mechanical Engineering, Energy Program

by
Hasan AVCI

September, 2023
İZMİR

Ph.D. THESIS EXAMINATION RESULT FORM

We have read the thesis entitled **"OPTIMIZING THE DESIGN PARAMETERS OF CONDENSING BOILER BY NUMERICAL, EXPERIMENTAL AND ARTIFICIAL NEURAL NETWORKS METHODS"** completed by HASAN AVCI under supervision of **PROF.DR. DİLEK KUMLUTAŞ** and we certify that in our opinion it is fully adequate, in scope and in quality, as a thesis for the degree of Doctor of Philosophy.

.....

Prof.Dr. Dilek KUMLUTAŞ

Supervisor

.....	.....
Prof. Dr. Yalçın ÇEBİ	Asst. Prof. Dr. Özay AKDEMİR
Thesis Committee Member	Thesis Committee Member
.....	.....
Assoc. Prof. Dr. Mustafa Turhan ÇOBAN	Prof. Dr. Aydoğan ÖZDAMAR
Examining Committee Member	Examining Committee Member

Prof. Dr. Okan FISTIKOĞLU

Director

Graduate School of Natural and Applied Sciences

ACKNOWLEDGMENT

I would like to thank Prof. Dr. Dilek KUMLUTAŞ, my doctoral thesis supervisor and project executive, for her guidance and support throughout my academic life and work.

This thesis was supported by The Scientific and Technological Research Council of Turkey (TUBİTAK) and Türk Demirdöküm Fabrikaları A.Ş. with the 5180092 & 3130798 encoded 1505 and 1501 projects. I want to express my appreciation for participating in these projects.

I want to thank my project team colleague Dr. Özgün ÖZER, M.Sc. Utku Alp YÜCEKAYA, M.Sc. Ahmet Yakup CUMBUL, and M.Sc. Semih YILMAZ, who have always supported me.

Also, I would like to express and show my gratitude to Prof. Dr. Yalçın ÇEBİ and Asst. Prof. Dr. Özay AKDEMİR for their support during my research.

I want to express my endless gratitude to my lifemate, Specialist Dr. Ceylan AVCI, who has always been with me and supported me with endless love and patience. Special thanks to my father, mother, brother, and whole family, who never forgave their support and made me come to this day.

Hasan AVCI

OPTIMIZING THE DESIGN PARAMETERS OF CONDENSING BOILER BY NUMERICAL, EXPERIMENTAL AND ARTIFICIAL NEURAL NETWORKS METHODS

ABSTRACT

This doctoral thesis addresses the use of numerical, experimental, and artificial intelligence methods to investigate and optimize the design parameters of the condensing boiler and its main components. The main objective of the thesis is to determine the design parameters of condensing boilers, which affect the appliance's performance, efficiency, and generated heat transfer during the boiler development process. Experimental setups are built up, experimental results validate numerical models, and they are used for training the artificial neural networks. Finally, the design parameters of the condensing boiler can be optimized in terms of emissions, heat transfer and fluid dynamics.

Small capacity wall hang condensing boilers (20-35 kW) are generally designed and manufactured. It is not easy to develop a big capacity condensing boiler with low NOx emissions in terms of technical to meet the EN15502 standard requirements. In this thesis, a 153 kW wall hang boiler is developed and manufactured according to the results of numerical and experimental studies. The determined optimum parameters of the combustion values provide the 153 kW maximum input load with 31.45 mg/kWh NO_x emission. The high-capacity and low-emission wall-hang condensing boiler prototype has been successfully completed.

Keywords: Condensing boiler, computational fluid dynamics and heat transfer (CFDHT), artificial neural networks (ANNs), NO_x emission

YOĞUŞMALI BOYLER TASARIM PARAMETRELERİNİN SAYISAL, DENEYSEL VE YAPAY SİNİR AĞLARI YÖNTEMLERİ İLE OPTİMİZE EDİLMESİ

ÖZ

Bu doktora tezi, yoğuşmalı kazan ve ana bileşenlerinin tasarım parametrelerini araştırmak ve optimize etmek için sayısal, deneysel ve yapay zekâ yöntemlerinin kullanımını ele almaktadır. Tezin temel amacı, kazan geliştirme sürecinde cihazın performansını, verimliliğini ve üretilen ısı transferini etkileyen yoğuşmalı kazanların tasarım parametrelerini belirlemektir. Deney düzenekleri oluşturulmuş olup deneysel sonuçlar ile sayısal modeller doğrulanmış ve yapay sinir ağlarının eğitimi için kullanılmıştır. Son olarak yoğuşmalı kazanın tasarım parametreleri atık gaz emisyonları, ısı transferi ve akışkanlar dinamiği açısından optimize edilebilmiştir.

Genel olarak küçük kapasiteli duvar tipi yoğuşmalı kazanlar (20-35 kW) tasarlanıp üretilmektedir. EN15502 standardı gerekliliklerini sağlayacak düşük NO_x emisyonlu, büyük kapasiteli yoğuşmalı kazan geliştirmek teknik açıdan kolay değildir. Bu tezde sayısal ve deneysel çalışmaların sonuçlarına göre 153 kW'lık duvar tipi yoğuşmalı kazan geliştirilmiş ve üretilmiştir. Yanma değerlerinin belirlenen optimum parametreleri ile 153 kW maksimum giriş yükünü 31,45 mg/kWh NO_x emisyonu ile sağlanmıştır. Tez kapsamında yüksek kapasiteli ve düşük emisyonlu duvar tipi yoğuşmalı kazan prototipi başarıyla tamamlanmıştır.

Anahtar kelimeler: Yoğuşmalı kazan, hesaplamalı akışkanlar dinamiği ve ısı transferi (HADIT), yapay sinir ağları (YSA), NO_x emisyonu

CONTENTS

Page

Ph.D. THESIS EXAMINATION RESULT FORM ii
ACKNOWLEDGMENT iii
ABSTRACT iv
ÖZ v
CONTENTS vi
LIST OF FIGURES x
LIST OF TABLES xviii
LIST OF SYMBOLS xxii
ABBREVIATIONS xxiv

CHAPTER ONE - INTRODUCTION 1

1.1 Literature Survey 2
1.2 Application of Condensing Boilers 8
1.3 Main Parts of Condensing Boilers 10
1.3.1 Heat Engine 10
1.3.2 Condensation and Flue Drainage System 14
1.3.3 Electronic Management System 14
1.4 Aim and Motivation 15

CHAPTER TWO - THEORETICAL INVESTIGATION OF CONDENSING BOILER 17

2.1 Working Principle of Condensing Boilers 17
2.2 Boundary Diagrams 18
2.3 The Mathematics of Computational Fluid Dynamics and Heat Transfer for Condensing Boilers 23

CHAPTER THREE - NUMERICAL INVESTIGATION OF CONDENSING BOILER 27

3.1 Numerical Investigation of the Condensing Boiler 27

3.1.1 The Results and Discussion of the Numerical Investigation of the Condensing Boiler 32

3.2 The Numerical Investigation of the Flue Gas's Flow Characteristics for the Different Heat Exchanger Designs 36

3.2.1 The Results and Discussion of the Numerical Investigation of the Flue Gas's Flow Characteristics for the Different Heat Exchanger Designs ... 43

3.2.1.1 The Variation of the Fin Height 43

3.2.1.2 The Variation of the Fin Thickness 48

3.3 The Numerical Investigation of the Flow Characteristics of the Flue Gas Movement Inside the Combustion Unit Modelling with the Air Domain and Flue Gas Domain 50

3.3.1 The Results and Discussion of the Numerical Investigation of the Flow Characteristics of the Flue Gas Movement Inside the First Basic Control Volume Modelling with the Air Domain and Flue Gas Domain 55

3.3.2 The Results and Discussion of the Numerical Investigation of the Flow Characteristics of the Flue Gas Movement Inside the Second Basic Control Volume Modelling with the Air Domain and Flue Gas Domain 56

3.4 The Investigation of the Impact of Design Parameters of the Condensing Boiler's Heat Exchanger on Boiler Performance 61

3.4.1 The Results and Discussion of the Investigation of the Impact of Design Parameters of the Condensing Boiler's Heat Exchanger on Boiler Performance 67

3.5 The Investigation of Thermal Performance of the Internally Channels Type of the Finned Tube Heat Exchanger Used for Condensing Boiler 70

3.5.1 The Results and Discussion of the Investigation of Thermal Performance of the Internally Channels Type of the Finned Tube Heat Exchanger Used for Condensing Boiler 75

CHAPTER FOUR - EXPERIMENTAL INVESTIGATION OF CONDENSING BOILER 79

4.1 The Experimental Investigation of the Flow Characteristics of the Flue Gas Movement Inside the Combustion Unit Modelling with the Air Domain and Flue Gas Domain 80

4.2 The Experimental Investigation of Thermal Performance of the Internally Channels Type of the Finned Tube Heat Exchanger Used for Condensing Boiler 87

4.3 The 23 kW Condensing Boiler Experiments 91

4.3.1 The Effects of the Air-Gas Equivalence Ratio on the Boiler Performance 95

4.3.2 The Effects of the Fan Speed on the Boiler Performance 101

4.3.3 The Determination of Optimum Design Point 106

4.4 The 153 kW Condensing Boiler Experiments 112

CHAPTER FIVE - OPTIMIZATION STUDIES OF CONDENSING BOILER 122

5.1 Optimization of Design Parameters of the Finned tube Heat Exchangers by Artificial Neural Networks for the Condensing Boilers 123

5.1.1 The Results and Discussion of the Optimization of Design Parameters of the Finned Tube Heat Exchangers by Artificial Neural Networks for the Condensing Boilers 127

5.2 Optimization of the Emission and Performance Parameters of the Wall-Hang Condensing Boiler by Artificial Neural Networks Trained with Real-world Data 134

5.2.1 The Artificial Neural Network Study for the Estimation of CO_2 Emission of the Condensing Boiler with Real-world Data 135

5.2.2 The Artificial Neural Network Study for the Estimation of CO Emission of the Condensing Boiler with Real-world Data 136

5.2.3 The Artificial Neural Network Study for the Estimation of NO Emission of the Condensing Boiler with Real-world Data 138
5.2.4 The Artificial Neural Network Study for the Estimation of NO_2 Emission of the Condensing Boiler with Real-world Data 139
5.2.5 The Artificial Neural Network Study for the Estimation of Q_c and P_{ch} Performance of the Condensing Boiler with Real-world Data 140
5.2.6 The Results and Discussion of the Cascade Structure of Artificial Neural Network Study for the Condensing Boiler with Real-world Data 142

CHAPTER SIX - CONCLUSIONS 146

REFERENCES 150

LIST OF FIGURES

Page

Figure 1.1 Condensing boiler schematic 4

Figure 1.2 Condensing boiler schematic 5

Figure 1.3 Numerical model of the sand-casting aluminium heat exchanger 6

Figure 1.4 Boiler's general design and the main zones considered for modelling discretisation..... 7

Figure 1.5 Heat engine sample for gas-fired condensing boilers 10

Figure 1.6 Types of heat exchanger for a heat engine of the gas-fired condensing boiler a) stainless steel coil tube heat exchanger b) sand casting aluminium heat exchanger c) aluminium finned tube coil heat exchanger 11

Figure 1.7 The components of gas-air mixing system a) fan b) venture c) gas valve 13

Figure 1.8 The burners for gas-fired condensing boilers..... 13

Figure 2.1 The working diagram of the condensing boiler 18

Figure 2.2 The wall-hang condensing boiler 19

Figure 2.3 The floor-standing condensing boiler 19

Figure 2.4 The boundary diagram of the wall-hang condensing boiler (WHBc)..... 20

Figure 2.5 The schematic view of condensing boiler inside 21

Figure 2.6 The boundary diagram of WHBc's heat engine..... 22

Figure 2.7 Definition of a control volume..... 23

Figure 2.8 The surface forces that act on a surface element within the control volume 25

Figure 3.1 The numerical three-dimensional model of the flue gas's air volume 29

Figure 3.2 The cross-section and dimension details of the finned heat exchanger .. 30

Figure 3.3 The mesh structure for the numerical model..... 30

Figure 3.4 The boundary conditions for the numerical model 32

Figure 3.5 The streamlines inside the internal air volume of the combustion unit .. 33

Figure 3.6 The air flow distribution at the upper region of the internal air volume of the combustion unit 34

Figure 3.7 The air flow distribution at the lower region of the internal air volume of the combustion unit 35

Figure 3.8 The temperature distribution of the internal air volume in the combustion unit..... 35

Figure 3.9 The numerical three-dimensional model of the flue gas's air volume 38

Figure 3.10 The cross-sectional schematic view of the designed heat exchanger for the condensing region 38

Figure 3.11 The cross-sectional schematic view of the finned tube heat exchangers arrayed in the condensing zone 39

Figure 3.12 The mesh structure for the numerical models 41

Figure 3.13 The boundary conditions for the numerical models..... 42

Figure 3.14 The streamlines for 1.5 mm fin thickness in the middle region of the condensing zone's internal air volume; a) representation of the middle region of the internal air volume of the condensing zone b) streamlines for 4 mm fin length c) streamlines for 6 mm fin length d) streamlines for 8 mm fin length e) streamlines for 10 mm fin length..... 45

Figure 3.15 The streamlines for 2 mm fin thickness in the middle region of the condensing zone's internal air volume; a) streamlines for 4 mm fin length

b) streamlines for 6 mm fin length c) streamlines for 8 mm fin length d) streamlines for 10 mm fin length 46

Figure 3.16 The streamlines for 2.5 mm fin thickness in the middle region of the condensing zone's internal air volume; a) streamlines for 4 mm fin length b) streamlines for 6 mm fin length c) streamlines for 8 mm fin length d) streamlines for 10 mm fin length 47

Figure 3.17 The schematic view of the general operation principle for the condensing boiler with a heat recovery device..... 51

Figure 3.18 The three-dimensional numerical model for the internal volume of the first basic heat recovery device..... 51

Figure 3.19 The schematic view of the control volume 52

Figure 3.20 The mesh structure for the numerical model..... 53

Figure 3.21 The comparison graph for experimental and numerical results of the pressure drops..... 54

Figure 3.22 The streamlines inside the internal volume of the first basic heat recovery device at the 9.5 m/s fluid velocity modelling with the air and flue gas domain..... 55

Figure 3.23 The schematic view of the control volume of the second basic heat recovery model..... 57

Figure 3.24 The three-dimensional numerical model for the internal volume of the second basic heat recovery device 57

Figure 3.25 The mesh structure for the numerical model of the second basic heat recovery device 58

Figure 3.26 The streamlines inside the internal volume of the second basic heat recovery device 59

Figure 3.27 The detail streamlines inside the control volume of the basic heat recovery device 59

Figure 3.28 Schematic representation of the working principle of the heat engine unit of a condensing wall-hang heating appliance 62

Figure 3.29 The modelled internal volume of the heat engine 63

Figure 3.30 The numerical model and boundary conditions 64

Figure 3.31 Schematic representation of the heat transfer regions of the heat engine unit of a condensing wall hang boiler. 72

Figure 3.32 Three-dimensional numerical models with different internal channel numbers 73

Figure 3.33 Mesh structure of numerical models 73

Figure 3.34 General cross-sectional view of heat exchanger structure with the single internal channel 74

Figure 3.35 Schematic representation of boundary conditions for numerical models 75

Figure 3.36 General view of new finned tube heat exchanger with eight channels .. 77

Figure 4.1 The schematic view of the experimental setup for the first basic heat recovery model's control volume 81

Figure 4.2 The experimental setup for the first basic heat recovery model's control volume 81

Figure 4.3 The schematic view of the second experimental setup for the first basic heat recovery model's control volume with flue gas 83

Figure 4.4 The second experiment setup for the first basic heat recovery model’s volume with flue gas 83

Figure 4.5 The third experimental setup for the second heat recovery model's control volume with flue gas 86

Figure 4.6 The detailed view of the heat engine with single internal channel heat exchanger a) technical view of the single channel heat exchanger b) the cross-section of heat engine design c) the top view of the heat engine prototype with single internal channel heat exchanger 88

Figure 4.7 The prototype of the wall-hang condensing boiler with the single-channel heat exchanger 89

Figure 4.8 The detailed view of the heat engine with eight internal channels heat exchanger a) the cross-section of eight channels heat exchanger b) the cross-section of heat engine design c) the top view of the heat engine prototype with eight internal channels heat exchanger 90

Figure 4.9 The prototype of the wall-hang condensing boiler with the eight channels heat exchanger 91

Figure 4.10 The gas/air mixing system of the wall-hang condensing boiler 92

Figure 4.11 Schematic view of experimental setup 93

Figure 4.12 The experimental setup for the 23 kW condensing boiler 93

Figure 4.13 The variation graph of input heat load when changing the air-gas equivalence ratio for natural gas 96

Figure 4.14 The variation graph of input heat load when changing the air-gas equivalence ratio for G20 gas 96

Figure 4.15 The variation graph of CO emission when changing the air-gas equivalence ratio for natural gas 97

Figure 4.16 The variation graph of CO emission when changing the air-gas equivalence ratio for G20 gas 97

Figure 4.17 The variation graph of NO emissions when changing the air-gas equivalence ratio for natural gas 98

Figure 4.18 The variation graph of NO emissions when changing the air-gas equivalence ratio for G20 gas..... 99

Figure 4.19 The variation graph of NO_2 emissions when changing the air-gas equivalence ratio for natural gas 100

Figure 4.20 The variation graph of NO_2 emissions when changing the air-gas equivalence ratio for G20 gas..... 100

Figure 4.21 The variation graph of input heat load when changing the fan speed for natural gas 101

Figure 4.22 The variation graph of input heat load when changing the fan speed for G20 gas..... 102

Figure 4.23 The variation graph of CO emission when changing the fan speed for natural gas 103

Figure 4.24 The variation graph of CO emission when changing the fan speed for G20 gas..... 104

Figure 4.25 The variation graph of NO emission when changing the fan speed for natural gas 105

Figure 4.26 The variation graph of NO emission when changing the fan speed for G20 gas..... 104

Figure 4.27 The variation graph of NO_2 emission when changing the fan speed for natural gas 105

Figure 4.28 The variation graph of NO_2 emission when changing the fan speed for G20 gas..... 105

Figure 4.29 The variation graph of NO when changing the modulation ratio of condensing boiler a) φ values are shown, and b) φ values are not shown 107

Figure 4.30 The variation graph of NO_2 when changing the modulation ratio of condensing boiler a) φ values are shown, and b) φ values are not shown 108

Figure 4.31 The variation graph of Q_c when changing the air-gas equivalence ratio for 5500 rpm 109

Figure 4.32 The variation graph of Qc when changing the air-gas equivalence ratio for 1700 rpm 110

Figure 4.33 The aluminium heat exchanger for 153 kW wall-hang condensing boiler 113

Figure 4.34 The design of the heat engine for the 153 kW wall-hang condensing boiler 114

Figure 4.35 The prototype of the designed burner 114

Figure 4.36 The internal view of the heat engine's prototype 116

Figure 4.37 The internal view of the heat engine's prototype 117

Figure 4.38 The variation graph of emissions when changing the modulation ratio of 23 kW wall-hang condensing boiler a) NO emission b) NO_2 emission 119

Figure 4.39 Combustion unit surface temperature measurements at rated operating condition 120

Figure 5.1 The histogram graph of relative errors in the training of the artificial neural network 126

Figure 5.2 The structure selected for ANN modelling 127

Figure 5.3 The scatter plot of the total heat transfer (Q_T) on the inner surface of the tube 129

Figure 5.4 The scatter plot of the maximum temperature on the fins (Tmax) 130

Figure 5.5 The scatter plot of the total heat transfer ($\bar{Q}_T$) per unit volume of the heat exchanger 131

Figure 5.6 The scatter plot of the pressure drops (ΔP) between the inlet and outlet of the internal volume 132

Figure 5.7 The selected structure for ANN modelling of the CO_2 emission 135

Figure 5.8 The decision flow diagram of the usage of the normalisation method to the data set 137

Figure 5.9 The selected structure for ANN modelling of the CO emission 138

Figure 5.10 The selected structure for ANN modelling of the NO emission 139

Figure 5.11 The selected structure for ANN modelling of the NO_2 emission 140

Figure 5.12 The selected structure for ANN modelling of the Q_c and P_{ch} 141

Figure 5.13 The cascade structure for ANN modelling for the wall-hang condensing boiler 142

Figure 5.14 The scatter plot of relative error at the training process for the cascade operation of artificial neural networks 142

LIST OF TABLES

Page

Table 3.1 Thermophysical properties of air 31

Table 3.2 The temperature values in each helical coil 31

Table 3.3 Design parameters for twelve different designs 40

Table 3.4 The effect of fin height variation on numerical results for 1.5 mm fin thickness 44

Table 3.5 The effect of fin height variation on numerical results for 2 mm fin thickness 44

Table 3.6 The effect of fin height variation on numerical results for 2.5 mm fin thickness 47

Table 3.7 The effect of fin thickness variation on numerical results for 4 mm fin height 48

Table 3.8 The effect of fin thickness variation on numerical results for 6 mm fin height 48

Table 3.9 The effect of fin thickness variation on numerical results for 8 mm fin height 49

Table 3.10 The effect of fin thickness variation on numerical results for 10 mm fin height 49

Table 3.11 The inlet velocities for the boundary condition of the air domain 52

Table 3.12 The comparison of the results for modelling the air and flue gas inside the first basic control volume 56

Table 3.13 The comparison of the results for the different control volumes modelled with the flue gas domain 60

Table 3.14 The composition of the combustion gases @ G20 (100% CH_4) & Phi =0.75 65

Table 3.15 The variation of design parameters 66

Table 3.16 Sort of design cases in terms of the fin thickness and their maximum and minimum values of output parameters 68

Table 3.17 Optimized design cases in terms of their target criteria 68

Table 3.18 Optimum design case (Q_T, $\bar{Q}_T$ max.; ΔP min.) 69

Table 3.19 The results of the analysis for the numerical models 76

Table 4.1 The experimental results of the first basic control volume at various fan voltages 82

Table 4.2 The second experimental results of the first basic control volume with flue gas 84

Table 4.3 The comparison of the experimental results for the air and flue gas inside the first basic control volume 85

Table 4.4 The third experimental results of the second basic control volume with flue gas 86

Table 4.5 The comparison of the experimental results for the air and flue gas inside the first basic control volume 87

Table 4.6 The variation of design parameters 93

Table 4.7 Experimental results of all design points 95

Table 4.8 The emissions for the variation of Q_c when changing the air-gas equivalence ratio for 5500 rpm 109

Table 4.9 The emissions for the variation of Q_c when changing the air-gas equivalence ratio for 1700 rpm 110

Table 4.10 Experimental results of initial and optimum design points 111

Table 4.11 The comparison of emissions and input heat loads between initial and optimum design points 112

Table 4.12 The performance and emission values for maximum input load (nominal input load, Q_n) 120

Table 4.13 The performance and emission values for minimum input load (Q_{min}) 120

Table 4.14 The NO_x measurement results according to EN15502..... 121

Table 5.1 The comprasion of performance by different ANN topologies..... 125

Table 5.2 The input values of the estimation dataset 128

Table 5.3 The comparison of results for total heat transfer (Q_T) on the inner surface of the tube..... 128

Table 5.4 The comparison of results for the maximum temperature on the fins (T_{max}) 129

Table 5.5 The comparison of results for the total heat transfer ($\bar{Q}_T$) per unit volume of heat exchanger 130

Table 5.6 The comparison of results for the pressure drop (ΔP) between the inlet and outlet of internal volume 131

Table 5.7 Comparison of the parametric result evaluated numerically and using ANN model for best design case 132

Table 5.8 Comparison of errors by different ANN configurations of CO_2 emission 135

Table 5.9 Comparison of errors by different ANN configurations of CO emission 137

Table 5.10 Comparison of errors by different ANN configurations of NO emission 138

Table 5.11 Comparison of errors by different ANN configurations of NO_2 emission 139

Table 5.12 Comparison of errors by different ANN configurations of Q_c and P_{ch} . 141

Table 5.13 The input parameters and values of estimation data sets 143

Table 5.14 The comparison of results for the CO_2 emissions 143

Table 5.15 The comparison of results for the CO emissions 143

Table 5.16 The comparison of results for the NO emissions 144

Table 5.17 The comparison of results for the NO_2 emissions..... 144

Table 5.18 The comparison of results for the Qc 145

Table 5.19 The comparison of results for the P_{ch} 145

LIST OF SYMBOLS

C_p	: Specific heat (J kg^{-1} K^{-1})
d	: Tube inside diameter (mm)
d_{in}	: Inner diameter (mm)
d_{out}	: Outer diameter (mm)
D_h	: Coil diameter (mm)
dS	: Elemental surface area
f	: Weisbach friction factor
g	: Gravitational constant, 9.81 (m s^{-2})
h	: Heat transfer coefficient (W $m^{-2}K^{-1}$)
h_f	: Fin height (mm)
k	: Thermal conductivity coefficient (W $m^{-1}K^{-1}$)
L	: Fin lenght (mm)
$\vec{n}$	: Normal vector
R	: Average accuracy
S	: Total entropy (kJ K^{-1})
s	: Fin spacing (mm)
T	: Temperature (K)
t_f	: Fin thickness (mm)
T_{in}	: Inlet temperature (K)
T_f	: Film Temperature (K)
T_{max}	: Maximum temperature on the fins (°C)
u	: One dimensional velocity component (m s^{-1})
U_m	: Mean velocity (m s^{-1})
Q_c	: Working input load (kW)
Q_{min}	: Minimum input load (kW)
Q_n	: Nominal input load (kW)
Q_T	: Total heat transfer on the inner surface of the tube (W)
$\bar{Q}_T$	: the total heat transfer per unit volume (W mm^{-3})

V	: Volume (m^3)
Δ_p	: Pressure drops (Pa)
α	: Thermal diffusivity ($m^2\ s^{-1}$)
ν	: Kinematic viscosity ($m^2\ s^{-1}$)
μ	: Dynamic viscosity ($kg\ m^{-1}\ s^{-1}$)
ρ	: Density ($kg\ m^{-3}$)
τ	: Time scale
σ	: Standard deviation of the relative error
$\vec{v}$	: Flow velocity ($m\ s^{-1}$)
φ	: air-gas equivalence ratio (fuel/air)
Ω	: Total mass (kg)

ABBREVIATIONS

AI	: Artificial Intelligence
ANN	: Artificial Neural Network
ANNs	: Artificial Neural Networks
CFD	: Computational Fluid Dynamics
CFDHT	: Computational Fluid Dynamics and Heat Transfer
DNS	: Direct Numerical Simulation
Er	: Relative Error
FD	: Finite Difference
FE	: Finite Element
FV	: Finite Volume
G20	: Pure Methane Gas
GAR	: Gas Appliance Regulation
LPG	: Liquid Petroleum Gas
MRE	: Mean Relative Error
NG	: Natural Gas
HVAC	: Heating, Ventilation and Air Conditioning
ErP	: Energy Related Products
NASA	: National Aeronautics and Space Administration of USA
R&D	: Research and Development
RMS	: Root Mean Square
WHBc	: Wall-Hang Condensing Boiler
WHBcs	: Wall-Hang Condensing Boilers

CHAPTER ONE
INTRODUCTION

The heating industry is advancing rapidly, and condensing boilers are leading the way in providing energy-efficient, eco-friendly, and cost-effective solutions. These cutting-edge heating systems represent a significant departure from conventional boilers, revolutionizing how we think about heating our homes and businesses.

Boilers that condense are gaining popularity as they effectively harness heat from combustion, leading to a substantial decrease in energy wastage and greenhouse gas emissions. These boilers embody the continual drive towards sustainability in the heating industry and offer a feasible alternative to conventional heating setups.

Transitioning from conventional boilers to condensing ones is crucial for a sustainable and efficient future. Traditional boilers waste much energy by releasing it into the environment as heat during combustion. On the other hand, condensing boilers recover this lost heat, resulting in maximum energy utilization. This leads to decreased energy consumption and greenhouse gas emissions, which aligns with global efforts to combat climate change. In addition to reducing heating costs for homeowners and businesses, it reflects our shared commitment to reducing our carbon footprint, preserving energy resources, and promoting a greener and more responsible approach to heating our homes and buildings. Some regulations are applied to decrease the emissions (CO, NO, NO_2, and NO_x) and increase the efficiency of gas-fired condensing boilers. EN 15502 (EN 15502 -1:2012+A1:2015, 2015), Ecodesign and Energy Labelling Directive (Ecodesign and Energy Labelling, 2019), Energy-related Products (ErP) (Energy-related Products, 2009), and Gas Appliance Regulation (GAR) (Gas Appliances Regulation, 2016) are the European Union regulations that apply to gas appliances, including gas-fired condensing boilers.

For gas-fired condensing boilers to be placed on the European and Turkish markets, manufacturers must ensure that their products meet the requirements outlined in the European regulation mentioned above, including safety, efficiency, emissions, and environmental standards. This often involves testing and certification by accredited bodies. Researchers, designers, and manufacturers must research new components,

combustion systems and working conditions for gas-fired condensing boilers to meet these requirements.

1.1 Literature Survey

Individual or central heating is the heat generated for hot water demand and heating at buildings or living spaces and consumed in the same independent section (Türkeri, 2007). Condensing boiler appliances are part of individual heating systems and are increasing their usage due to the widespread natural gas infrastructure in our country and Europe.

With an increasing concern about environmental changes, emissions and costs for clients, condensing technology offers an efficient heating solution for various applications. Many regulations have been made about the energy efficiency of appliances used for heating the residence space. Since September 2015, the ErP directive has enforced condensing technology when using natural gas in newly built and refurbished houses. Wall-hang non-condensing boilers have been forbidden in our country since April 2018 with the implementation of ErP regulations. The goal of the ErP directive is to increase the energy efficiency of energy-related products.

The energy efficiency, condensate and emissions are important design parameters for boilers used in living spaces according to regulations and directives. The producers of condensing boilers have to do detailed engineering studies to adapt the existing wall-hang non-condensing heating appliances to a condensed version and design new condensing appliances per the related regulations.

In the literature, many studies focused on the burner combustion characteristic, which means increasing combustion stability and emission reduction. A study conducted by Specchia and Toniato (2009) analysed premixed burners designed for natural gas combustion with a low environmental impact. Their research specifically focused on the combustion performance of structured burners in real operating conditions, utilising a commercial domestic boiler. The findings indicated that offered burners displayed superior CO emission performance compared to commercial

burners. However, NO emissions increased under the same operating conditions (Specchia and Toniato, 2009).

According to research by Lee et al. (2011), a multi-hole premixed burner with a cylindrical shape was assessed for a condensing gas boiler. The study analysed the burner's hole diameter, arrangement, and equivalence ratio. The findings revealed that the cylindrical burner exhibited minimal CO and NO_x emissions, measuring under 30 ppm and 40 ppm (Lee, Kum, and Lee, 2011a).

In 2014, a study was conducted by Zhang and colleagues on a premixed burner utilised in commercial environments. Their goal was to enhance the gas mixing system. Their findings indicated that the uniformity of the gas mixing system outlet significantly impacted the emission (Zhang, Lui, and You, 2014).

Numerical analyses and optimization of burner combustion reactions inside the wall-hang condensing boilers should be investigated separately, and their outputs are defined as boundary conditions for numerical studies of the boiler’s heat engine.

The most important components are the heat exchanger and flow baffles for wall-hang condensing boilers. They play a significant role in the thermal performance, efficiency, and emissions. In the literature, many experimental studies exist, and they have investigated the heat transfer and thermal performance of the air domain of various finned tube heat exchangers (Kim, Youn and Webb, 1999; Du and Wang, 2000; Wang, Lee and Sheu, 2001; Perrotin and Clodic, 2003; Keawkampro et al., 2021; Kiatpachai et al. 2022; Maghsoudali, Rastegarkoutenaei, Sahami and Bandpy, 2023). These studies are only performed for specific experiment conditions and different application areas.

However, little experimental research investigates whole condensing boilers under the combustion reaction. Lee et al. (2011b) experimentally examined the effects of the determined design parameters of the heat engine on the condensing gas-fired boiler’s performance, as shown in Figure 1.1. Upper heat exchangers, lower heat exchangers, and coils and baffle arrangements were selected as design parameters. By utilising the most efficient heat exchangers, the heating efficiency of this boiler increased by 10%

compared to a traditional model. When operating at an equivalence ratio of 0.70, the NO_x and CO emissions were approximately 30 ppm and 160 ppm, respectively. While it was important to note that reducing CO emissions was ideal, the pollutant emission of this boiler was considered acceptable when compared to the performance of a condensing boiler (Lee, Kum, and Lee, 2011b).

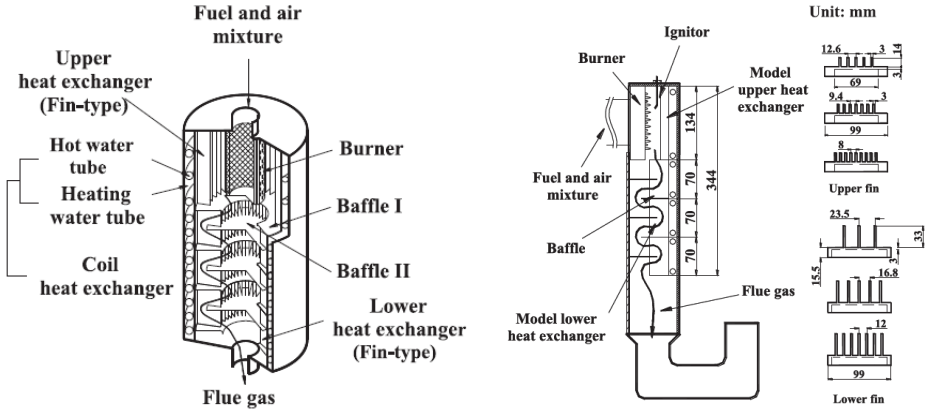


Figure 1.1 Condensing boiler schematic (Lee, Kum, and Lee, 2011b)

Balanescu and Homutescu (2017) performed an experimental study on combustion system optimization in the case of a 36 kW condensing boiler (Figure 1.2). The condensing system under analysis was a premixed type, comprising an air blower, gas valve, fuel gas-air mixer, and cylindrical multi-hole burner. In addition to obtaining the desired nominal heat output, it was crucial to have a wide heat output range for flexibility in accommodating varying loads. Thus, reducing the minimum heat output of the boiler was imperative. The maximum and minimum heat output was influenced by the maximum and minimum airflow entering the combustion system, regulated by the minimum nozzle area in the fuel gas-air mixer. Four different fuel gas-air mixers were experimented with to determine the best solution for the combustion system under consideration.

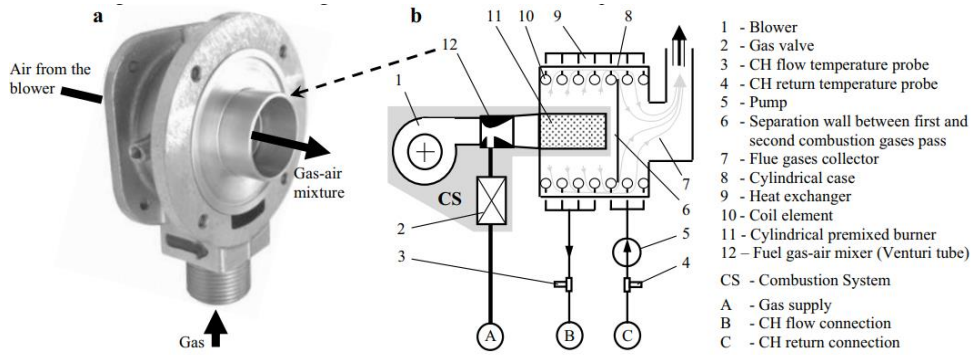


Figure 1.2 Condensing boiler schematic (Balanescu and Homutescu, 2017)

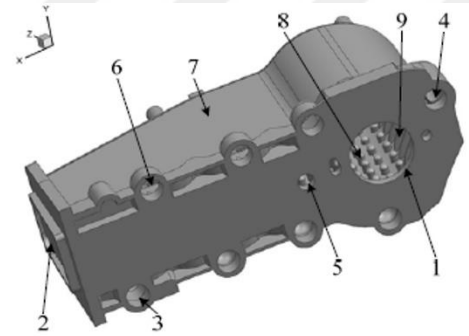
Another study by Balanescu and Homutescu (2018) investigated condensing boiler performance experimentally in real operating conditions. 25 kW condensing boiler was performed. If the condensing boiler system was replaced instead of a traditional one, the maximum fuel saving could be 17.5% (Balanescu and Homutescu, 2018).

Besides the experimental studies, numerical methods have to be used to investigate the flow and heat transfer distributions inside the condensing boilers. In the literature, there are a lot of numerical studies regarding various types of heat exchangers used for different applications and areas, such as cooling, heat recovery and so on (Tutar and Akkoca, 2004; Bilirgen, Dunbar and Levy, 2013; Alimoradi, Olfati and Maghareh, 2017; Dhumal and Havaldar, 2021; Rostami and Ganji, 2023). Evaluating the numerical studies of the finned tube heat exchanger design in literature used for gas-fired heat engines, there is a detailed study by Wais (Wais, 2010). The optimization study of the radial finned tube heat exchanger investigated the effect of the different flow rates and wing profiles on performance. It is acceptable that the fin profile determines the characteristic and direction of the flow. Three-dimensional models with different air velocity values and fin shapes were developed to improve the heat transfer characteristics between the finned tube and air. The average airflow temperature in the outlet volume was calculated and compared for different models.

Nevertheless, a few research articles investigated heat and flow characteristics inside gas-fired heat engines of condensing boilers via numerical methods. Karaaslan et al. (2013) made the numerical model of the sand-casting aluminium heat engine used for condensing combi boilers. They investigated the heat transfer and flow

characteristics in the case of the fin and without fin designs (Karaaslan, Çalışır, Yılmazoğlu, Yılmaz and Başkaya, 2013).

The shape of wall fin patterns significantly impacts flue gas flow, affecting the performance of a condensing boiler's heat exchanger. A study was conducted by Cao and You (2017) to determine the best pattern for wall fins in flue gas channels for stand-casting aluminium heat exchangers (Figure 1.3). It was found that circular fins, which are commonly used, do not provide optimal heat transfer efficiency between the fin and flue gas due to reduced effective contact time. Instead, using elliptical fins was found to be more effective. Elliptical fins delayed the detachment point, increased the effective heat transfer area by 7.6%, and increased the average heat transfer coefficient by 12.1%.



1-Flue gas inlet, 2-Flue gas outlet, 3-water inlet, 4-water outlet, 5-outfall, 6-water turn port, 7-shell, 8-pin fin, 9- H-fin

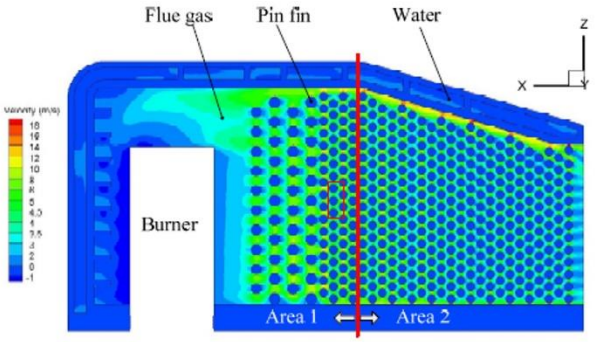


Figure 1.3 Numerical model of the sand-casting aluminium heat exchanger (Cao and You, 2017)

Antonescu and Stanescu (2017) presented the numerical and computational modelling of a condensing boiler made of an aluminium-finned tubed tube exchanger (Figure 1.4). Validation of computational results was made by comparison with the

experimental results. The geometry modelling considered the discretisation of the heat exchanger in several zones, characterised by homogenous flue gas flow speed, flow geometry and heat transfer characteristics (mainly feature length).

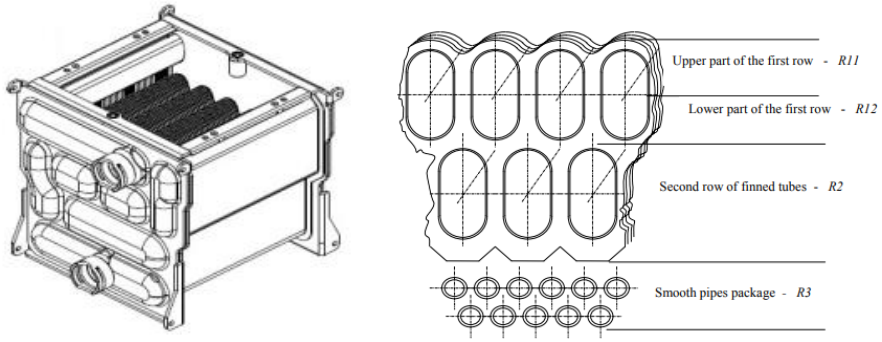


Figure 1.4 Boiler's general design and the main zones considered for modelling discretisation (Antonescu and Stanescu, 2017)

When analysing the effects of a limited number of design parameters on thermal systems, numerical methods are often preferred. Nonetheless, to evaluate the impact of a broader range of design parameters and speed up the analysis process, it is recommended to integrate these methods with prediction techniques. Thermal problems are often resolved by analysing input and output parameter correlations. These correlations involve complex and non-linear relationships between independent variables. In such situations, Artificial Intelligence (AI) can be a valuable tool for efficiently estimating and optimising the outputs. Artificial intelligence has many applications, including design, optimization, heat exchangers, multi-phase fluid flows, and combustion systems (Shang, 2005; Cheng, Huang, Pang and Zhang, 2018; Vidyadhar, Mahesh, Malpani, Sapre and Kulkarni, 2019; Zoebiry and Humfeld, 2021). One of the AI methods is the Artificial Neural Network (ANN)

Mohanraj et al. have reviewed ANN applications for thermal analysis of heat exchangers (Mohanraj, Jayaraj and Muraleedharan, 2015). In literature, ANN methods were used to model finned tube heat exchangers to estimate control volume temperatures, heat transfer rate, and pressure variance. These heat exchangers are commonly employed in refrigeration, air conditioning, and heat pump applications

(Pacheco-Vega, Diaz, Sen, Yang and Mcclain, 2001; Wu, Zhang, Tao, He, and Tao, 2008; Singh, Aute and Radermacher, 2009).

The literature uses the ANN method for heat exchanger modelling and optimization studies (Giannetti et al., 2020; Xie et al., 2022; Kamsuwan et al., 2023). Xie et al. used artificial neural networks to optimize the vortex generator design for fin and tube heat exchangers (Xie et al., 2022). Zhang et al. optimized heat transfer and pressure drop of a fin and tube heat exchanger using Computational Fluid Dynamic (CFD) simulation and neural networks, considering inlet air velocity and design parameters (Xie et al., 2023). No studies in the literature have investigated the design parameters of heat engines for condensing wall-hung boilers using the ANN method to analyse heat transfer and performance output.

1.2 Application of Condensing Boilers

The history of condensing boilers is a story of innovation and environmental awareness in the heating technology industry. The idea of condensing boilers can be traced back to the 1970s when scientists and engineers started looking for ways to enhance the efficiency of traditional boilers. Before this, traditional boilers released a significant amount of heat as wasted gases, inefficient and harmful to the environment.

In the 1980s, there was a significant advancement in materials and combustion technology, leading to the creation of boilers that could capture and use wasted heat. Condensing boilers were developed to recover heat from exhaust gases by condensing water vapour in flue gases. This innovation increased energy efficiency and reduced harmful emissions into the atmosphere.

During the 1990s, condensing boilers gained popularity due to their ability to save energy and natural gas lines to become widespread. Governments and environmental organisations promoted them as a sustainable heating option. As energy efficiency regulations became stricter and climate change became a bigger concern in the 21st century, condensing boilers were quickly adopted. Today, they are widely used in residential and commercial heating, helping to reduce energy consumption and carbon footprints.

Condensing boilers are heating systems that are highly efficient and widely used in both residential and commercial applications. They offer significant advantages over traditional non-condensing boilers, such as increased energy efficiency and reduced emissions. Below are some primary applications where condensing boilers are commonly used.

Residential Heating: Condensing boilers are popular for heating and providing hot water in residential spaces. They use natural gas, propane, or oil to offer efficient and reliable heat to households.

Commercial Buildings: Condensing boilers are commonly installed in commercial buildings, including offices, schools, hospitals, and apartments, for space heating and hot water supply for showers, kitchens, and laundry facilities.

Industrial Applications: Industries that require a significant amount of hot water or steam can use condensing boilers to fulfil their heating needs. Food processing, manufacturing, and chemical production commonly rely on these boilers.

District Heating: Condensing boilers are often utilised in district heating systems, where a central plant generates and distributes heat to multiple buildings through a network of pipes. This is an efficient method for providing heating to entire communities.

Greenhouse Heating: In agriculture, especially in greenhouse operations, condensing boilers are utilised to maintain optimal temperatures for plant growth. These boilers are energy-efficient and assist in reducing heating costs for large greenhouse facilities.

Renewable Energy Integration: Condensing boilers can be used as a backup heat source when renewable energy sources like solar panels or heat pumps are not producing enough energy.

Boiler Replacement: As part of energy efficiency upgrades in existing buildings, older non-condensing boilers are replaced with condensing boilers. This reduces energy consumption and flue gas emissions.

1.3 Main Parts of Condensing Boilers

There are three main parts for all gas-fired condensing boilers. These are heat engine, condensation and flue gas drainage system and electronic management system.

1.3.1 Heat Engine

Gas-fired condensing boilers operate on the fundamental principle of a heat engine, which transforms thermal energy into useful heat. These engines operate within the laws of thermodynamics, which govern heat flow from hot to cold areas. Gas-fired condensing boilers utilise this principle to extract the maximum energy from the fuel source. Figure 1.5 shows the heat engine sample used for gas-fired condensing boilers. It consists of several key components. These are heat exchangers, fans (blowers), venture, burners, gas valves, igniters, electrodes, and flame detectors.

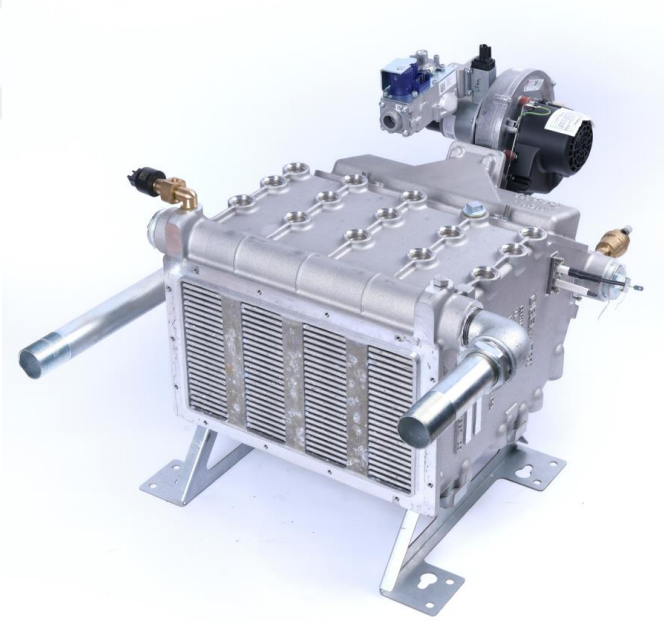


Figure 1.5 Heat engine sample for gas-fired condensing boilers

The most important component is the heat exchanger for the heat engine. They significantly affect condensing boilers' thermal performance, efficiency, and emission. The combustion reaction occurs inside the heat engine, and the generated heat is

transferred to the water domain by the heat exchanger and flow baffles. These components are made of generally stainless steel and aluminium materials. Their geometries and manufacturing technologies are also important regarding total heat transfer, pressure drop and emissions. Besides the performance values of the condensing boiler, the cost of the appliance is an essential parameter for design. As understood, many input and output parameters need to be optimized.

The most used types of heat exchangers are given in Figure 1.6. Conventional condensing boilers generally use the stainless-steel coil tube heat exchanger (Figure 1.6.a). This type of heat exchanger has limited extended surfaces. Nowadays, aluminium heat exchangers (Figure 1.6.b, c) are used to develop new WHBc due to their cost and free machining. Extended surfaces are created easily for aluminium heat exchangers.

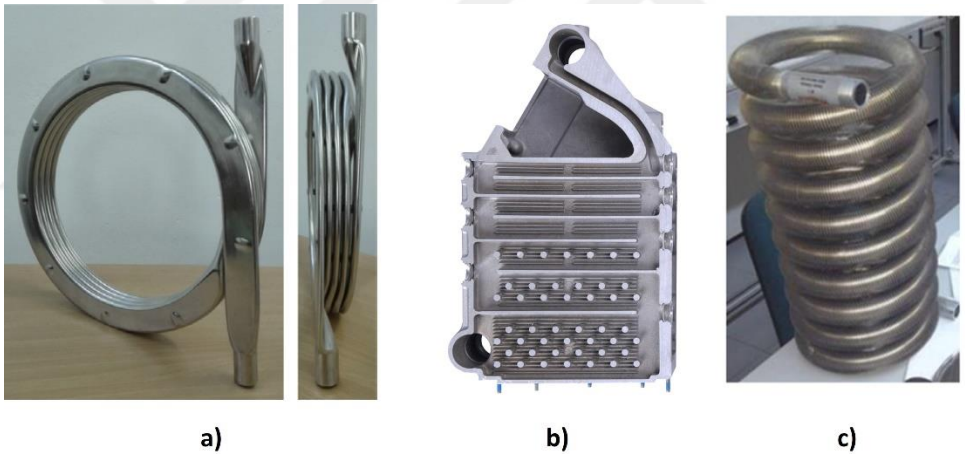


Figure 1.6 Types of heat exchanger for a heat engine of the gas-fired condensing boiler a) stainless steel coil tube heat exchanger (Balanescu and Homutescu, 2018) b) sand casting aluminium heat exchanger c) aluminium finned tube coil heat exchanger

Heat exchangers enable the efficient transfer of heat generated from combustion to water, which can be used for heating. Several types of heat transfer are involved in the operation of condensing boilers.

Conduction is heat transfer through direct contact between materials at different temperatures. In a heat engine, conduction occurs within the heat exchanger. The heat exchanger is a component that separates the combustion gases from the water being

heated. As hot combustion gases pass through the heat exchanger's metal surfaces, they transfer heat to the metal. In turn, the metal conducts heat to the water that flows outside the heat exchanger. This process efficiently heats the water without mixing the two substances (combustion gases and water).

Convection is transferring heat by moving fluids (liquids or gases). In a heat engine, convection moves the heated water throughout the heating system. As water is heated within the heat exchanger, it becomes less dense and rises. This creates a natural circulation pattern where the heated water rises while cooler water from the system returns to the heat exchanger to be reheated. This circulation ensures that the entire heating system is supplied with warm water.

Radiation is the transfer of heat through electromagnetic waves. The flame produced during combustion emits infrared radiation, which can heat the surfaces of the heat exchanger. The hot surfaces then transfer heat to the water through conduction and convection.

The latent heat of flue gas is a unique feature of condensing boilers. When the water vapour in the combustion gases condenses back into liquid form, it releases significant heat. This heat, known as the latent heat of vaporisation, is a key factor in the high efficiency of condensing boilers. The heat exchanger is designed to maximise the condensation of water vapour from the combustion gases, capturing this additional heat energy.

The combination of these heat transfer processes makes condensing boilers highly efficient because they recover heat that would otherwise be wasted in non-condensing boilers. By utilising conduction, convection, and the latent heat of vaporisation, condensing boilers can achieve efficiency above 90%, making them an environmentally friendly and cost-effective choice for heating systems. Additionally, condensing boilers produce lower emissions and can help reduce energy consumption and heating costs.

Fuel and air are mixed at a specific ratio by a gas-air mixing system. Fan, venture, and gas valve are the main components of this system (Figure 1.7). This system

provides the fuel/air mixture. The venture is assembled to the fan's inlet, and the fan supplies the fresh air. The venture is a mechanical part, and its inlet diameter and shape determine the air ratio of fresh air for each fan speed. The gas valve is connected to one side of the venture, providing the fuel (natural gas, liquid petroleum gas, test gases) for each fan speed. Additionally, the gas valve has a mechanical adjustment point to regulate the air-gas equivalence ratio (φ).

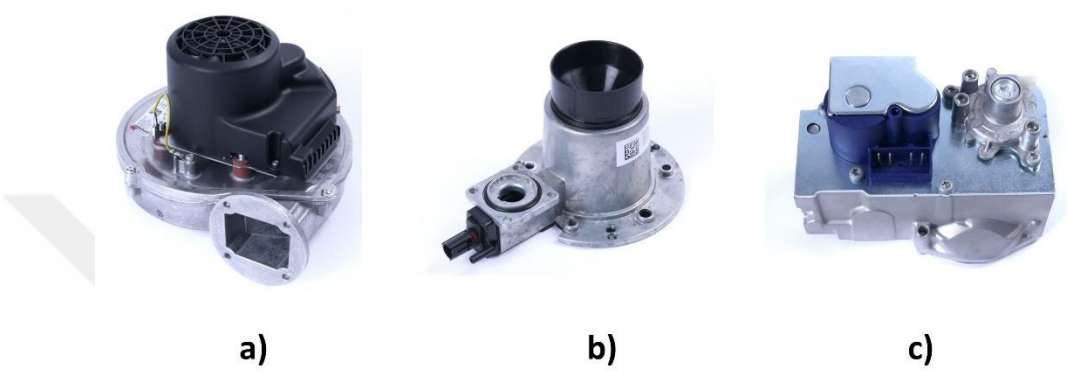


Figure 1.7 The components of gas-air mixing system a) fan b) venture c) gas valve

Burners ignite the fuel-air mixture in gas-fired condensing boilers, affecting the system's overall efficiency and emissions (Figurec1.8). Multi-hole burners represent a significant advancement in combustion technology. These burners enhance fuel and air mixing by utilising numerous small holes or nozzles for fuel and air injection into the combustion chamber, resulting in a more efficient and uniform combustion process. The combustion chamber's multiple injection points create turbulent flow, promoting complete combustion and reducing harmful emissions such as CO and NO_x.

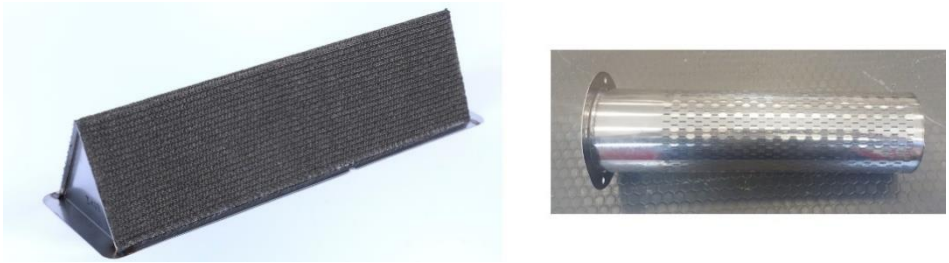


Figure 1.8 The burners for gas-fired condensing boilers

1.3.2 Condensation and Flue Drainage System

The condensation and flue drainage systems of gas-fired condensing boilers are crucial features that cannot be overlooked. They significantly enhance efficiency and offer a solution to the acidic condensate problem by utilising the latent heat in water vapour. When water vapour condenses, it creates a slightly acidic liquid because water (H_2O) reacts with the byproduct of combustion, carbon dioxide (CO_2), to form carbonic acid (H_2CO_3). It is important to safely manage this acidic condensate to avoid harm to the boiler.

Drainage systems designed specifically for flue gas are available. These systems collect and safely discharge the acidic condensate created during the condensation process. Effective condensate management is essential to safeguard the boiler and comply with environmental regulations governing the disposal of acidic wastewater.

1.3.3 Electronic Management System

Electronic management systems are responsible for controlling and adjusting the boiler's operation. This system in gas-fired condensing boilers serves as the brains behind the operation. They are designed to control various aspects of the boiler's performance, ensuring efficient and precise heating. These systems incorporate advanced sensors, processors, and control algorithms to manage critical functions like combustion, temperature regulation, and system monitoring.

Electronic management systems regulate fuel and air mixture in the combustion chamber, optimising the combustion process to maximise energy extraction and minimise emissions such as CO and NO_x. They have a significant advantage in their capacity to regulate the output of boilers. This allows boilers to modify their heating capacity according to the immediate need, ensuring that they work optimally even when handling partial loads.

These systems ensure efficient operation and comfort by maintaining a consistent water temperature in the boiler. They prevent energy waste by monitoring temperature fluctuations and preventing excessive cycling.

Electronic management systems can detect overheating, gas leaks, or malfunctions, enhancing operational safety and reducing accidents.

1.4 Aim and Motivation

The aim of this thesis is to determine and optimize the design parameters of the condensing boiler, which affect the appliance's performance, efficiency, emissions, and generated heat transfer. Experimental setups were built to define boundary conditions of numerical simulations, and their results were used to validate the numerical models. On the other hand, newly developed prototypes of heat exchangers and heat engines for condensing boilers were experimentally tested.

Numerical models were created for the main components of condensing boilers and for the whole boiler operation to investigate in detail. Many design cases were defined to evaluate the effects of design parameters on performance and emissions parametrically. Artificial neural networks were trained with numerical results and estimated the output parameters of the finned tube heat exchanger used in condensing the boiler's heat engine.

The evaluation of the real-world operating conditions of the 23 kW condensing boiler was investigated experimentally. All tests are performed according to the EN15502 standard. These results defined the optimum working parameters (air-gas equivalence ratio (φ) and fan speed) to minimise the NO, NO_x and CO emissions at specific input loads. These real-world operating values are used to create artificial neural networks to estimate the output parameters of the condensing boiler.

Small capacity wall hang condensing boilers (20-35 kW) are generally designed and manufactured. It is not easy to develop a big capacity condensing boiler with low NO_x emissions in terms of technical to provide the EN15502 standard requirements. When the combustion region is bigger, the NO_x formation occurs more than the small one due to the high flue gas temperatures. Finally, the 153 kW condensing boiler was developed and prototyped with all the results of the studies performed with this thesis scope. The development tests were completed according to standards and regulations.

The Scientific and Technological Research Council of Turkey partially supported this thesis (as projects grant no: TUBITAK-TEYDEB 5180092 & 3130798).

CHAPTER TWO
THEORETICAL INVESTIGATION OF CONDENSING BOILER

Condensing boilers are a modern heating technology that is more energy-efficient and environmentally friendly than traditional boilers, making them widely popular for residential and commercial use. The principle of condensing boilers is to recover latent heat from combustion, which would otherwise go to waste flue gas. This is done through innovative heat exchanger design and advanced materials, resulting in high thermal efficiencies. Condensing boilers are essential for sustainable and energy-efficient solutions in combating climate change and reducing energy consumption and emissions.

This theoretical investigation delves into the working principle, design considerations and boundary diagrams, the fundamentals and mathematics of computational fluid dynamics and heat transfer for numerical simulations.

2.1 Working Principle of Condensing Boilers

Condensing boilers are highly efficient equipment that utilises residual heat from combustion gases, including the latent heat of water vapour, to heat water for heating or industrial use.

Figure 2.1 shows the working principle of condensing boilers. Cold water is indicated as return water, which is heated and supplied to the heating system or application. Zone I is the combustion region of the boiler where the fuel (natural gas, LPG, different testing gases and so on) is burnt out and turns to flue gas form. Flue gases pass from Zone I to Zone II, and Zone II has the first heat exchanger coil in a high-temperature region. This heat exchanger transfers the heat from flue gas to water. They are passed through Zone III, which has the second coil of the heat exchanger. Flue gases are cooled below dew point temperature and start condensation at that region. The rest of the flue gases are discharged into the ambient. Therefore, the flue gas's remaining heat, including latent heat, preheats the water, increasing the energy efficiency of the process.

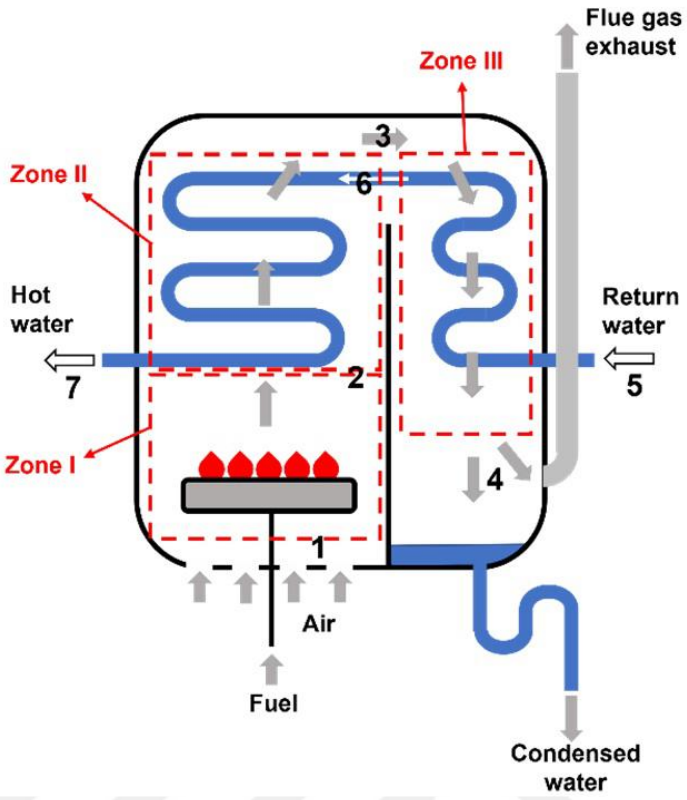


Figure 2.1 The working diagram of the condensing boiler (Ramirez and Taglioni, 2023)

2.2 Boundary Diagrams

Condensing boilers used for residential heating have two types in terms of application. These are wall-hang and floor-standing. The wall-hang condensing boilers are commonly used for domestic heating systems, as shown in Figure 2.2. Generally, they have various capacities (from 15 kW up to 160 kW) with a single heat engine. The floor-standing boilers are used for commercial and industrial heating systems, as shown in Figure 2.3. A special room or basement is needed for this type of boiler, and they have big capacities from 70 kW up to 1500 kW with a single heat engine.



Figure 2.2 The wall-hang condensing boiler (Riello, 2023a)



Figure 2.3 The floor-standing condensing boiler (Riello, 2023b)

Both types of condensing boilers have the same heat engine and combustion system technology. The only difference is the installation type to wall or floor.

A general representation of the boundary diagram is given for the wall-hang condensing boiler (WHBc) in Figure 2.4. Gas, air, electricity, and cold water are inputs, and flue gas, condensate water, waste heat, and hot water are outputs of this appliance. Basically, thermodynamic analysis of the wall-hang condensing boiler could be done to determine the effects of inputs on the output parameters of the boiler for its equilibrium state. But these analyses do not explain how heat transfers from the flue gas to the water domain.

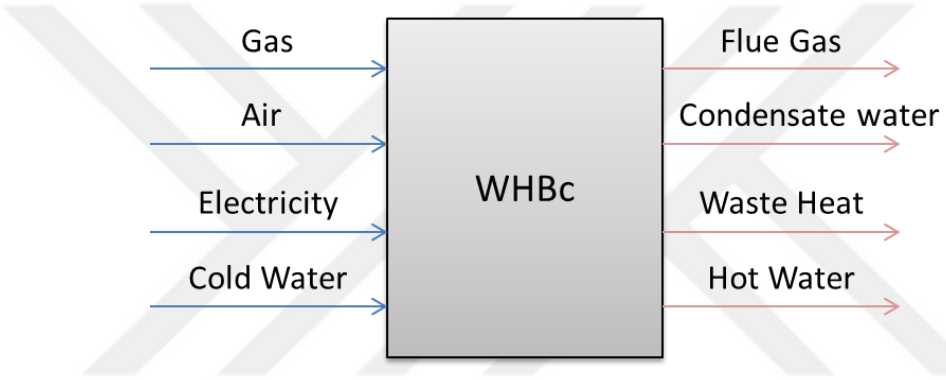


Figure 2.4 The boundary diagram of the wall-hang condensing boiler (WHBc)

The boundary diagrams and conditions should be created according to the forms of heat transfer inside the boiler to investigate the wall hang condensing boiler's performance in detail. A schematic view of the condensing boilers' inside is shown in Figure 2.5.

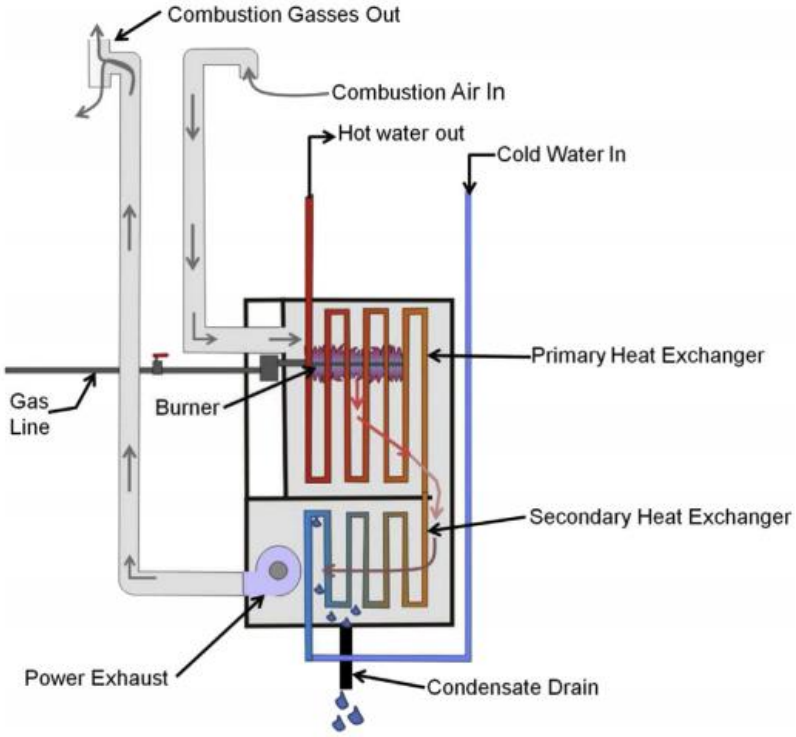


Figure 2.5 The schematic view of condensing boilers' inside (Satyavada and Baldi, 2018)

There are two different regions. The combustion chamber, where chemical combustion starts, and flue gas occurs at high temperatures for the first time. This region includes a burner and primary heat exchanger as a main component. Another region is related to the condensation phenomena. Every region has distinct heat transfer mechanisms. Therefore, the whole heat engine of the condensing boiler is modelled so complex. Regions should be evaluated separately and linked between them with an end-to-end process.

The heat engine (combustion system) is the main module of WHBc, which produces heat from natural gas or liquid gas and transfers it to the water domain. The heat engine has two different regions, shown in Figure 2.6. And their characteristics are mentioned above. The combustion chamber is indicated with a red dot rectangular area. It includes a burner, ignition electrodes, heat exchanger and outlet of water parts. Gas and air are mixed at venture with a specific ratio. This ratio is adjusted by the fan and gas valve. The mixture is directly led to the burner. The burner's task is to enable combustion via ignition electrodes. Spark is produced by an ignition electrode from

electricity. After the sparking, the combustion reaction starts, and the flue gas formation takes place in that region. Heat is transferred to water and ambient by radiation, convection, and conduction. In the combustion chamber, a large amount of thermal energy diffuses with the heat transfer by radiation.

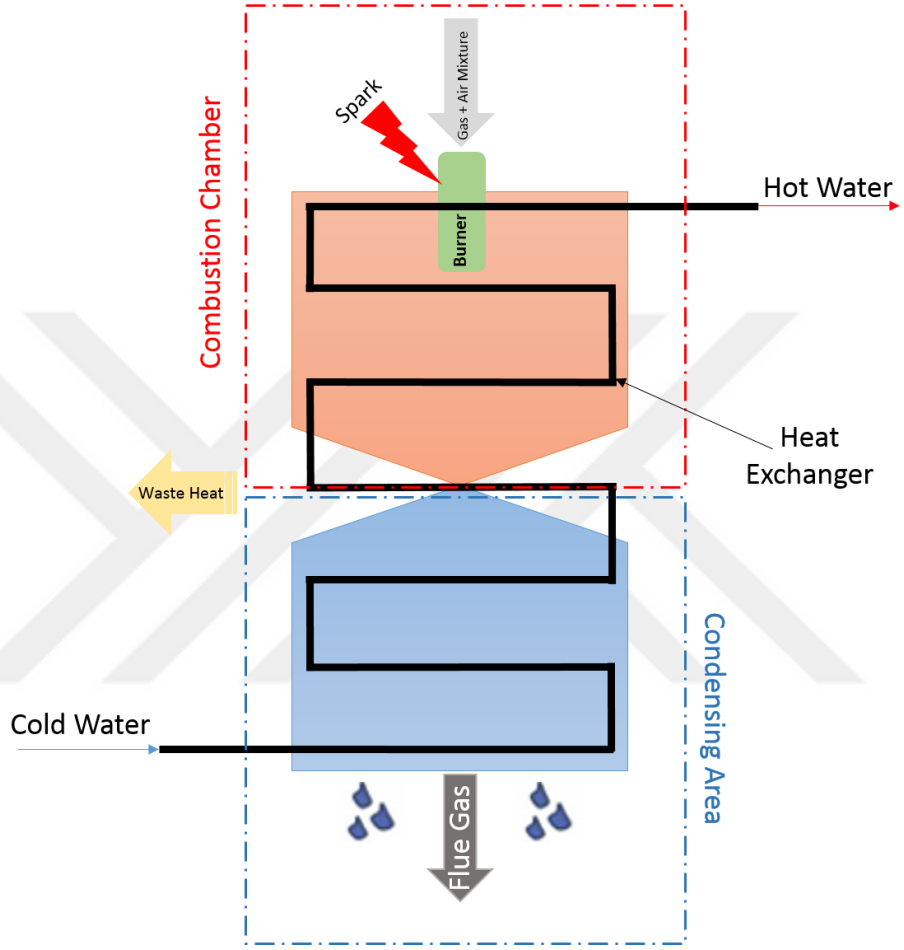


Figure 2.6 The boundary diagram of WHBc's heat engine

The condensing region is indicated with a blue dot rectangular area. It includes baffles, a heat exchanger, condensate drains and an inlet of water parts. The flue gas is directed to the exhaust pipe by baffles and heat exchanger. The flue gas has latent heat coming from the hot water vapour. To gain energy, water vapour must condense. The condensing region cools the steam through a specially designed heat exchanger. The energy gained is used to preheat the cold heating water. The hot water then passes into the combustion chamber, which is heated further to reach the desired temperature.

2.3 The Mathematics of Computational Fluid Dynamics and Heat Transfer for Condensing Boilers

The basis of Computational Fluid Dynamics and Heat Transfer (CFDHT) is the continuity, momentum, and energy equations, which are the basic fluid dynamics and heat transfer equations. These three fundamental conservation laws form the basis for all fluid dynamics, expressed mathematically: The conservation of mass, momentum, and energy.

CFDHT applications use various solution methods: Finite difference (FD), finite volume (FV), and finite element (FE). The ANSYS program employed in this thesis applies the finite volume method for numerical simulations, as represented in Chapter 3.

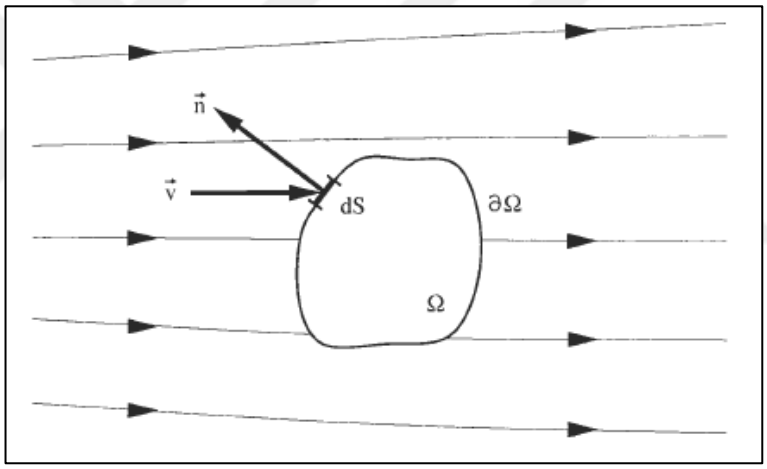


Figure 2.7 Definition of a control volume (Blazek, 2001)

The continuity equation can be derived by considering a finite control volume, as illustrated in Figure Figure 2.7. The flow velocity is represented by $\vec{v}$, the unit normal vector is $\vec{n}$, and dS signifies an elemental surface area. The conserved quantity is the density ρ. The time rate of change of the total mass Ω can be determined.

$$\frac{\partial}{\partial t}\int_{\Omega} \rho d\Omega \tag{2.1}$$

The contribution of convective flux across each surface element, *dS*, is considered.

$$\rho = (\vec{v}.\vec{n})dS \tag{2.2}$$

$\vec{n}$ consistently moves in a direction that is opposite to the control volume. If $(\vec{v}.\vec{n})$ is negative, it can be defined as inflow, and if $(\vec{v}.\vec{n})$ is positive, it is defined as outflow. The continuity equation can be expressed in integral form, as shown in Equation 2.3.

$$\frac{\partial}{\partial t}\int_{\Omega} \rho \mathrm{d}\Omega + \int_{\partial\Omega} \rho(\vec{\mathrm{v}}.\vec{n})\mathrm{dS} \tag{2.3}$$

The momentum equation can be obtained by applying Newton's second law, which relates the momentum of a mass element to the net force acting on it. This law can be extended to the momentum of a control volume Ω.

$$\rho\vec{v}d\Omega \tag{2.4}$$

The change in time of momentum within the control volume is equal to

$$\frac{\partial}{\partial t}\int_{\Omega} \rho\vec{v}d\Omega \tag{2.5}$$

The density times velocity is the conserved quantity is given below.

$$\rho\vec{v} = [\rho u, \rho v, \rho w]^T \tag{2.6}$$

The principle of momentum conservation is significantly dependent on the crucial role played by the convective flux tensor given by

$$\oint_{\partial\Omega} \rho\vec{v}(\vec{v}.\vec{n})\mathrm{dS} \tag{2.7}$$

Two types of forces act on the control volume: external body forces (such as gravity and buoyancy) and surface forces (such as pressure distribution and frictional stresses).

The external force from the body contributes to the preservation of momentum, as given below.

$$\int_{\Omega} \rho\vec{f_e}\mathrm{d}\Omega \tag{2.8}$$

Surface sources (Figure 2.8) are composed of isotropic pressure and viscous stress $\overline{\overline{\tau}}$ tensor.

$$\overline{Q}s = -p\overline{I} + \overline{\tau} \tag{2.9}$$

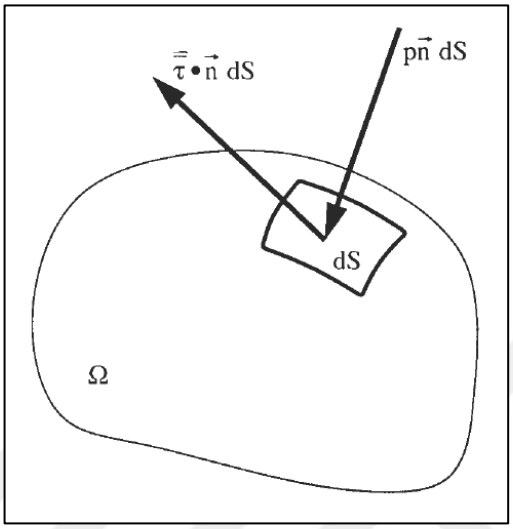


Figure 2.8 The surface forces that act on a surface element within the control volume (Blazek, 2001)

The momentum conservation equation for a control volume is expressed as Equation 2.10, considering all the above equations.

$$\frac{\partial}{\partial t}\int_{\Omega}\rho\vec{v}\mathrm{d}\Omega + \oint_{\partial\Omega}\rho\vec{v}(\vec{v}.\vec{n})\mathrm{dS} = \int_{\Omega}\rho\vec{f_e}\mathrm{d}\Omega - \oint_{\partial\Omega}p\vec{n}\mathrm{dS} + \oint_{\partial\Omega}(\overline{\tau}\vec{n})\mathrm{dS}) \tag{2.10}$$

The first law of thermodynamics can be used to derive the energy equation. It considers the net heat flux and the forces' work rate to determine changes in the total energy inside the volume over time. As shown below, the total energy per unit mass is the sum of the internal energy per unit mass and the kinetic energy per unit mass.

$$E = e + \frac{|\vec{v}|^2}{2} + \frac{u^2+v^2+w^2}{2} \tag{2.11}$$

The total energy per unit volume is

$$\frac{\partial}{\partial t}\int_{\Omega}\rho\mathrm{E}\mathrm{d}\Omega \tag{2.12}$$

the convective flow can be defined as

$$\oint_{\partial\Omega} \rho E(\overrightarrow{v}.\vec{n})dS \tag{2.13}$$

The diffusive flux exists in energy equations but not in continuity and momentum equations. The diffusive flux $\overrightarrow{F_D}$ is expressed for fluid at rest.

$$\overrightarrow{F_D} = -\gamma\rho\kappa\nabla e \tag{2.14}$$

The specific heat coefficient is defined as $\gamma = \frac{c_p}{c_v}$ and κ is the thermal diffusivity coefficient. It is expressed as the Fourier law of heat conduction. In Equation 2.15, the thermal conductivity coefficient is represented as k, and the absolute static temperature is T.

$$\overrightarrow{F_D} = -k\nabla T \tag{2.15}$$

The volumetric heating from chemical reactions or radiation is part of the net heat entering the control volume. The heat sources are referred as the time rate of heat transfer per unit mass ($\dot{q}_h$). Together with the rate of work done by the body forces $\vec{f}$ introduced for the momentum equation, it completes the volume sources.

$$Q_v = \rho\vec{f}\vec{v} + \dot{q}_h \tag{2.16}$$

Surface sources $\vec{Q}_s$ also influence the conservation of energy, which is the final parameter to consider. These values represent the rate of work done by pressure, shear, and normal stresses on a fluid element over time.

$$\vec{Q}_s = -p\vec{v} + \vec{\bar{\tau}}\vec{v} \tag{2.17}$$

The equations above can be used to express the concept of energy conservation.

$$\frac{\partial}{\partial t}\int_{\Omega} \rho E d\,\Omega + \oint_{\partial\Omega} \rho E(\vec{v}\vec{n})d\,S = \oint_{\partial\Omega} k(\nabla T\vec{n})d\,S + \int_{\Omega}(\rho\overrightarrow{f_e}\vec{v} + \dot{q}_h)d\,\Omega - \oint_{\partial\Omega} p(\vec{v}\vec{n})dS + \oint_{\partial\Omega}(\vec{\bar{\tau}}\vec{v})\vec{n}d\,S \tag{2.18}$$

CHAPTER THREE
NUMERICAL INVESTIGATION OF CONDENSING BOILER

Numerical modelling is used for many fields of engineering investigations. It can provide to be evaluated alternative solutions for complex thermal systems when their design phases to researchers. The condensing boilers have complex thermal, fluid dynamics and combustion mechanisms. In this chapter, thermal and fluid dynamics mechanisms are modelled for the essential parts of the condensing boiler and the whole boiler.

In the following section of this chapter, the numerical investigation of the condensing boiler, the numerical investigation of the flue gas's flow characteristics for the different heat exchanger designs, the numerical investigation of the flow characteristics of the flue gas movement inside the combustion unit modelling with the air domain and flue gas domain, the investigation of the impact of design parameters of the condensing boiler's heat exchanger on its performance and the investigation of thermal performance of the internally channels type of the finned tube heat exchanger used for condensing boiler are discussed.

3.1 Numerical Investigation of the Condensing Boiler

Heat exchangers, baffles and other flow obstacles used in the combustion units play an essential role in condensing heating devices' thermal performance and energy efficiency. These heat exchangers and baffles used in domains where the combustion reaction occurs can be produced from copper, aluminium or stainless-steel materials. In addition, the total heat transfer passed to the fluid domain from the burnt gas domain, known as the flue gas, and the pressure drops can be affected according to the geometry of the components used in the combustion unit.

Extended surfaces increase heat transfer via the convection in the heat exchangers inside the combustion units. These extended surfaces are mainly formed with finned tube geometries for heat exchangers made of aluminium material. In the literature, there are many experimental studies to investigate the heat transfer at air-side regions and the thermal performance of finned-tube heat exchangers of various fin types (Kim,

Youn and Webb, 1999; Du and Wang, 2000; Wang, Lee and Sheu, 2001; Perrotin and Clodic, 2003; Keawkampro et al., 2021; Kiatpachai et al. 2022; Maghsoudali, Rastegarkoutenaei, Sahami and Bandpy, 2023). These studies were conducted only under certain experimental conditions and for different application areas. However, there are few experimental studies for combustion units of condensing boilers where the combustion reaction occurs (Lee et al., 2011b).

In addition to experimental studies, numerical methods should be used in examining the heat transfer and flow distributions in the combustion unit of wall-mounted condensing heating devices. When the numerical studies in the literature about the finned tube heat exchanger design used in combustion units are examined, a detailed study was carried out by Wais in 2010 (Wais, 2010). The optimization study of the radial finned tube heat exchanger investigated the effect of different flow rate values and fin profile change on the performance.

In another study conducted by H. Bilirgen et al. in 2013, the effects of the design parameters of the determined finned structure on the average heat transfer and pressure drop occurring in the finned-tube heat exchanger were numerically investigated with the ANSYS program (Bilirgen et al., 2013). Although there are many numerical studies in the literature on the finned tube heat exchangers, almost no numerical study determines the heat and flow distributions by modelling the internal air volume of the combustion unit for the condensing boiler.

In the study conducted by Karaaslan et al. in 2013, the combustion unit of a boiler produced with the aluminium casting production technique was modelled numerically, and the heat transfer and flow characteristics of the fin and non-finned cases were investigated (Karaaslan et al., 2013).

In this study, the numerical model of the air volume of the combustion unit of the condensing boiler was first created. The heat transfer and fluid dynamics in this air volume have been modelled numerically, and the flow characteristics and heat distributions inside the combustion unit have been investigated in detail.

The numerical three-dimensional model of the flue gas's air volume was created (Figure 3.1) to examine the flow and heat distributions of the flue gas in the combustion unit.

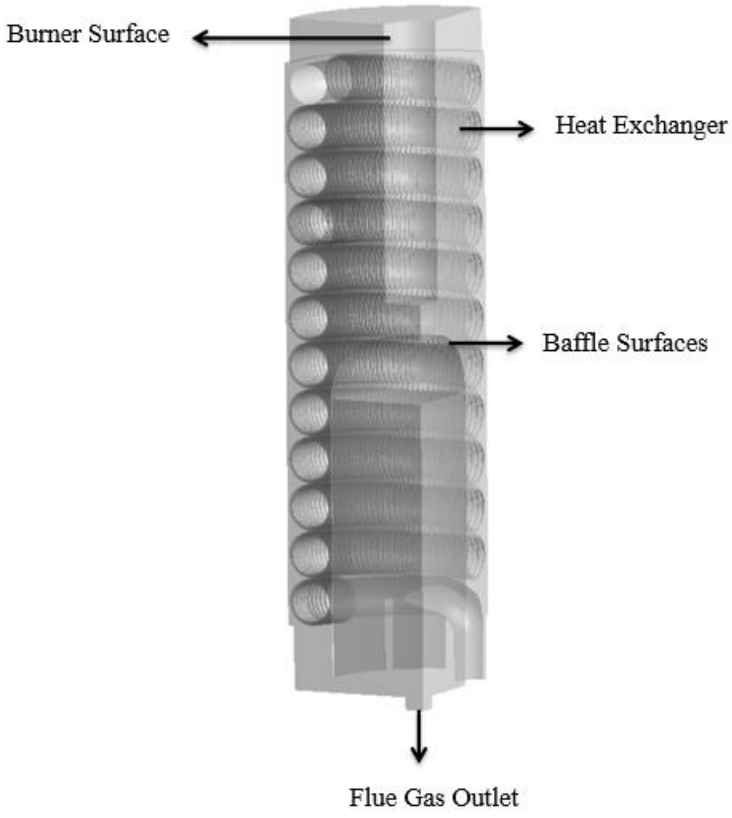


Figure 3.1 The numerical three-dimensional model of the flue gas's air volume

As seen in Figure 3.1, a quarter of the cylindrical combustion unit's internal air volume is modelled to reduce the mesh elements and the solution times. The heat exchanger surfaces, the burner surface, and the baffle surfaces are modelled as flow obstacles by removing them from the air volume.

The cross-section and dimension details of the aluminium-finned heat exchanger are given in Figure 3.2.

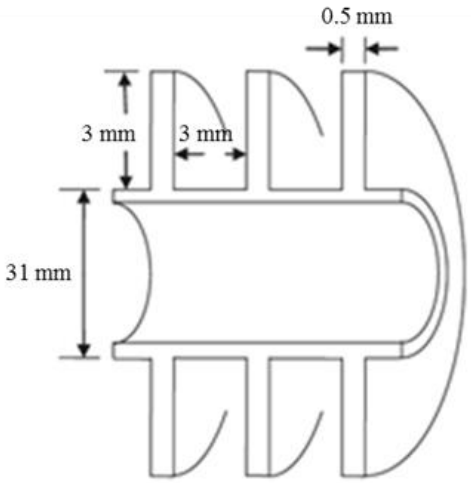


Figure 3.2 The cross-section and dimension details of the finned heat exchanger

After the modelling, the next step for numerical analysis is to separate the model into the mesh. A suitable mesh of the numerical model was created using different networking techniques. The mesh number of the numerical model is 835719, shown in Figure 3.3.

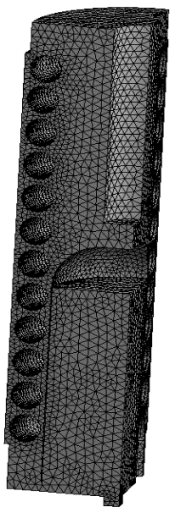


Figure 3.3 The mesh structure for the numerical model

The emissivity values of 0.42 for the 6000 series aluminium material at room temperature were defined for the heat exchanger surfaces. During the numerical solution for the flue gas volume, some thermophysical properties of air are used. The properties of the air were assumed as the values at the film temperature calculated by

averaging the experimentally determined flue gas temperatures at the inlet and outlet of the combustion unit. The thermophysical properties of air are given in Table 3.1. T_f is the film temperature, ρ is the density, C_p is the specific heat, k is the thermal conductivity, α is the thermal diffusivity, and ν is the kinematic viscosity (Incropera and Dewitt, 2000).

Table 3.1 Thermophysical properties of air

T_f [K]	ρ [kg/m^3]	C_p [J/kgK]	k [W/mK]	α [m^2/s]	ν [m^2/s]
850	0.4097	1110	0.0596	13.1 x10^{-5}	9.38 x10^{-5}

The boundary conditions are defined and shown in Figure 3.4. The combustible gas (natural gas, etc.) and air mixed in specific proportions pass through the burner surface with the help of a fan and enter the combustion unit. The inlet velocity of this mixture is defined as the boundary condition to the burner surfaces. Considering the fan flow rate and burner surface areas, the air inlet velocity was determined as 0.85 m/s.

The aluminium heat exchanger is designed from 12 coils with finned tubes. In numerical analyses, a constant temperature boundary condition is defined for the heat exchanger surfaces where the flue gas's air volume contacts. The temperature values in each helical coil were determined by experimental studies and are given in Table 3.2.

Table 3.2 The temperature values in each helical coil

Helical Coil	Temperature (K)	Helical Coil	Temperature (K)
1. Coil	428.15	7. Coil	375.15
2. Coil	423.15	8. Coil	355.65
3. Coil	420.65	9. Coil	345.15
4. Coil	438.15	10. Coil	337.15
5. Coil	405.15	11. Coil	331.15
6. Coil	393.15	12. Coil	328.15

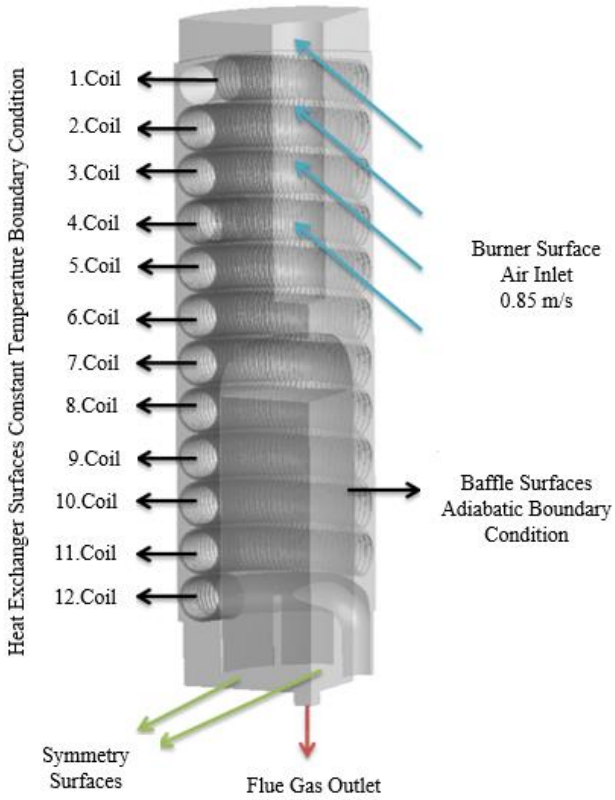


Figure 3.4 The boundary conditions for the numerical model

The baffle and other surfaces are adiabatic boundary conditions for the numerical study, except for the symmetry and flue gas outlet surfaces. The steady state, radiation effects, natural convection caused by gravity, forced convection caused by fan effect and turbulent flow type conditions are considered.

3.1.1 The Results and Discussion of the Numerical Investigation of the Condensing Boiler

When the data obtained from the numerical study are examined, the streamlines realised in the internal air volume of the combustion unit, which is modelled as a quarter, are given in Figure 3.5. The flue gas leaving the burner surface with a speed of 0.85 m/s is separated from the outlet area by reaching a speed of 71.19 m/s.

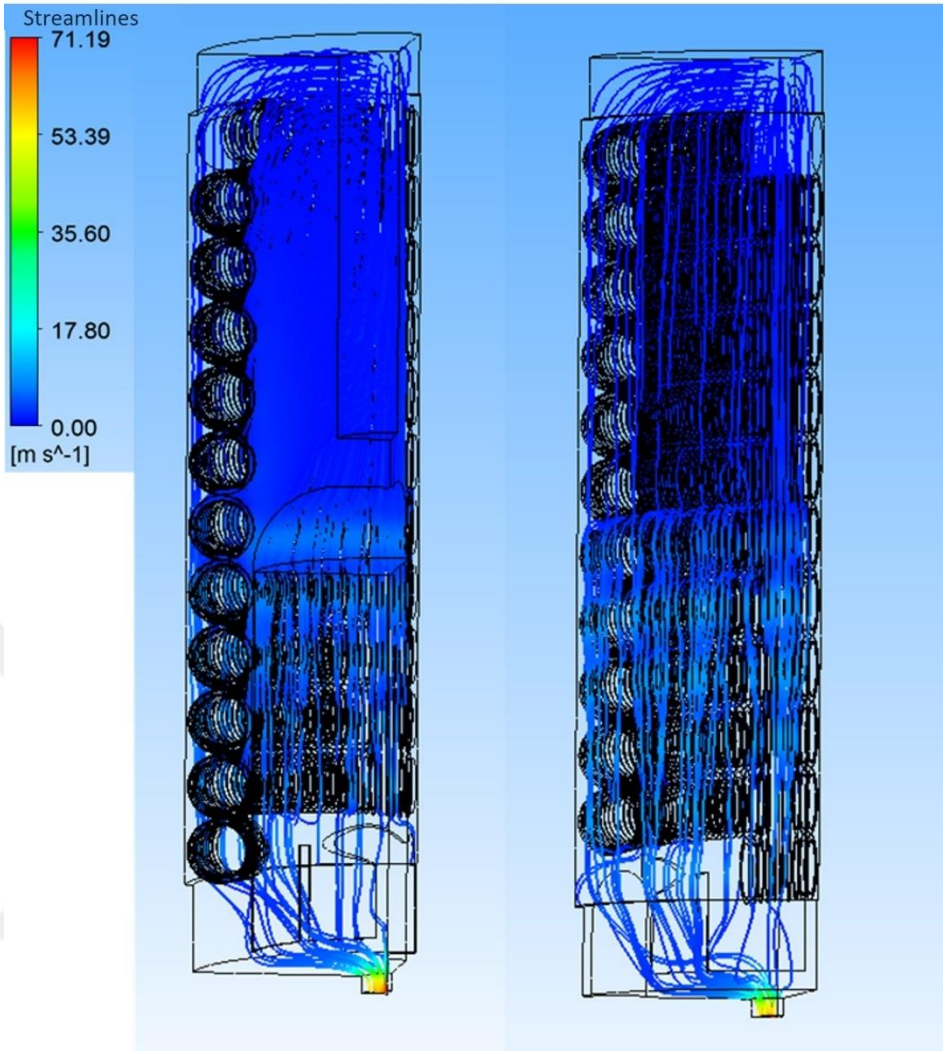


Figure 3.5 The streamlines inside the internal air volume of the combustion unit

As shown in Figure 3.5, a massive part of the flue gas first leaves the burner surface and then passes over the surfaces of the heat exchanger near the inner part of the combustion unit and moves towards the baffle.

In Figure 3.6, detailed findings of the flue gas movement in the upper region of the internal air volume of the combustion unit were obtained. In this region where the combustion reaction occurs, the heat transfer surface areas increased by the fins can not be used effectively. In addition, a considerable part of the total heat transfer in this region is transferred to the water by radiation. Therefore, finned type heat exchanger design and use in this region should be re-evaluated.

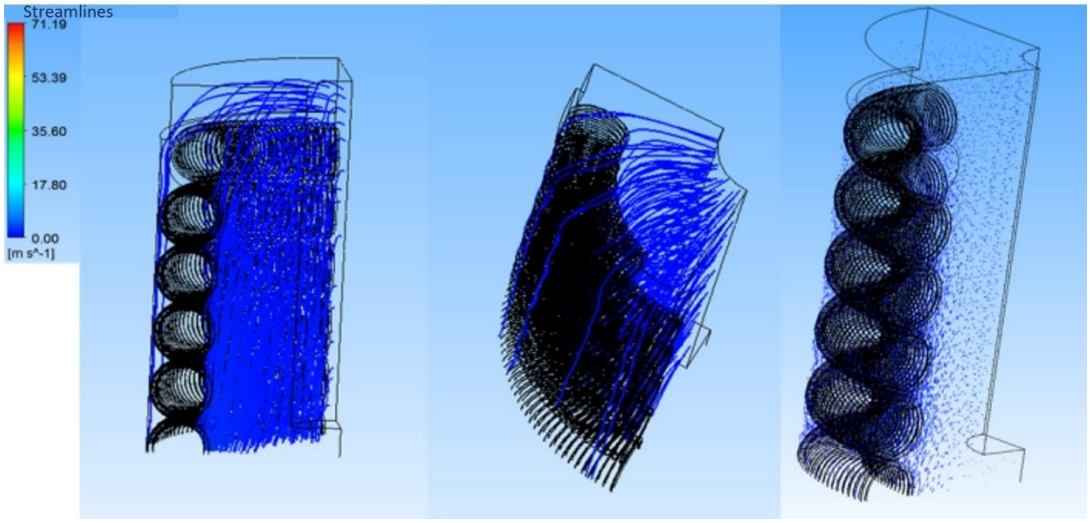


Figure 3.6 The air flow distribution at the upper region of the internal air volume of the combustion unit

Detailed findings of the airflow in the lower region of the internal air volume of the combustion unit are given in Figure 3.7. The flue gas is gone to the heat exchanger via the baffle. It is seen that the finned surfaces in this region are used effectively. In addition, as the velocity of the flue gas increases towards the outlet, the local convection coefficients on the finned surfaces also increase. The average local convection coefficient on the heat exchanger surfaces from the eighth to the twelfth coil is 43.03 W/m^2K. The condensation also occurs in this region. For these reasons, the fin structure and design of the heat exchanger used in this region significantly affect the total heat transfer.

The total pressure drops in the combustion unit, of which a quarter is modelled, is found as 2963 Pa.

The temperature distribution of the internal air volume in the combustion unit is given in Figure 3.8.

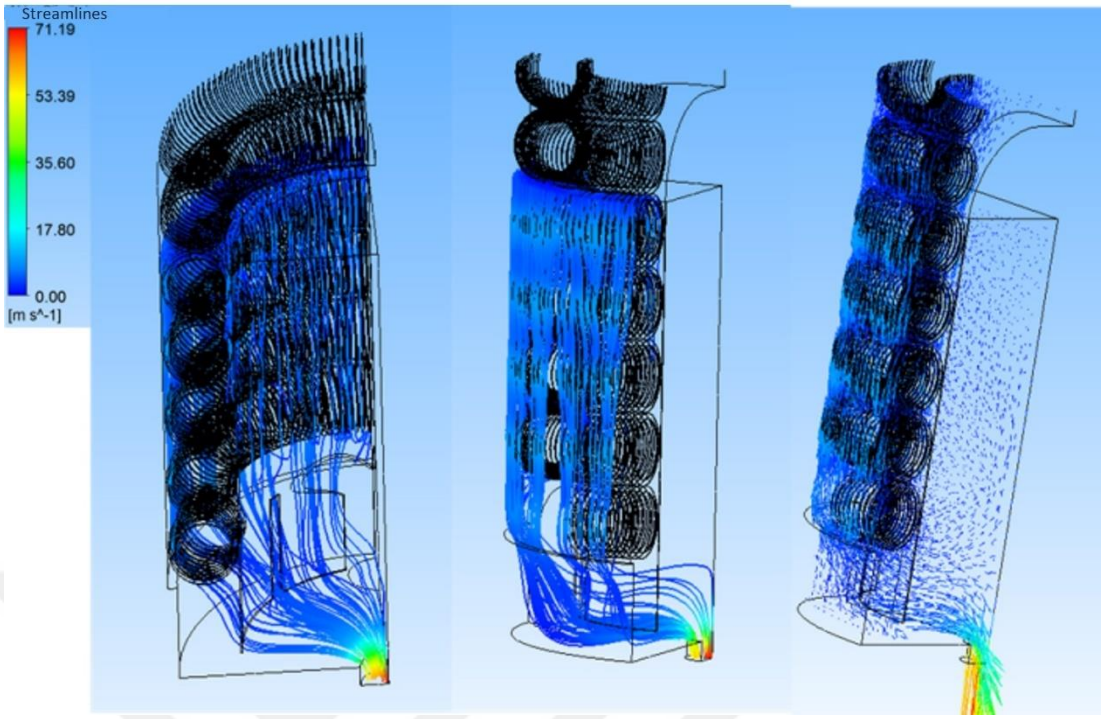


Figure 3.7 The air flow distribution at the lower region of the internal air volume of the combustion unit

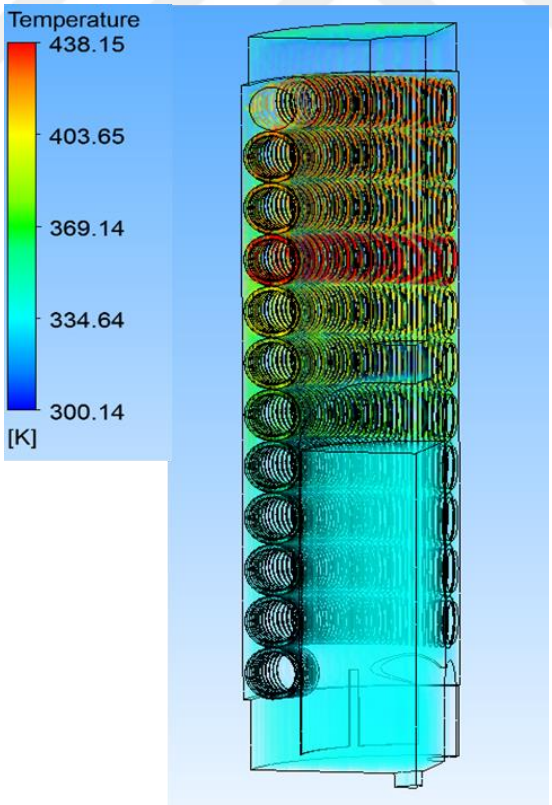


Figure 3.8 The temperature distribution of the internal air volume in the combustion unit

The temperature distributions of the flue gas in the lower region of the combustion unit indicate the actual situation. Most of the total heat transfer in this region occurs by convection.

The flue gas outlet temperature values for the wall-hang condensing boiler vary between 328.15 K and 338.15 K. In the numerical study, the average flue gas temperature value in the flue gas outlet is 335.48 K. As a result, the numerical study was modelled according to the flue gas temperature at the outlet region in terms of the thermal aspect.

The internal air volume of the combustion unit can be modelled numerically for the condensing boiler. Thus, the flow and temperature distributions of the flue gas are investigated in detail. In addition, it is found that such combustion units have two different thermal regions in this study. Although the combustion unit transfers a large part of the flue gas energy generated as a result of the combustion reaction to the water in the upper part of the internal air volume by radiation, a considerable part of the energy is transferred in the lower part of the internal air volume by convection. Therefore, it has been determined that the constant temperature boundary condition defined for the heat exchanger surfaces is not suitable for the upper region of the combustion unit.

With the detailed streamlines obtained as a result of this study, it has been shown that each component positioned in the combustion unit is practical for the flue gas movement.

3.2 The Numerical Investigation of the Flue Gas's Flow Characteristics for the Different Heat Exchanger Designs

The first numerical study shows us to be able to model the internal air volume of the condensing boiler. According to the first study result, the main components (heat exchanger type, baffle design, etc.) of the combustion unit affect the flue gas movement inside the heat engine. Furthermore, two different zones are found in terms of the heat transfer mechanisms. A considerable amount of heat transfer is occurred by the convection at the lower zone of the combustion unit. The design of the heat

exchanger located in this zone is essential to enhance the energy transfer from flue gas to water and decrease the pressure drop of the flue gas.

Extended surfaces are used to increase the convective heat transfer in the heat exchangers at the condensing zone of the combustion units. While these extended surfaces contribute positively to the total heat transfer, they increase the pressure drops in the combustion unit. These pressure drops determine the fan power used in the combustion unit. According to ERP regulations, efficiency calculations are used in electricity and the gas consumed by the boiler. Generally, aluminium finned tube heat exchangers are preferred in the condensing zone in new-generation combustion unit designs.

In this second study, the fin length and fin thickness of the aluminium finned tube heat exchanger that can be used in the condensing zone of the combustion units have been chosen as the design parameters. The cross-section details of 12 different types of finned tube heat exchangers were determined by choosing four different values for fin length and three different values for fin thickness. These heat exchangers are arranged in one or two rows to fit into the defined fixed volume. Thus, a three-dimensional internal air model of 12 different combustion units is created. The effects of the determined design parameters on the pressure drop and flow characteristics in the combustion unit were investigated in detail using the ANSYS program.

The designed combustion unit's flue gas air volume consists of two regions considering the total heat transfer. Figure 3.9 shows a high-temperature zone in the region where the burner is located and a condensation zone where the finned tube heat exchangers are designed. A finless helical aluminium tube heat exchanger is designed in the high-temperature region of the three-dimensional numerical model. In the condensing zone, a design consisting of finned-tube heat exchangers, the cross-section detail given in Figure 3.10, has been created.

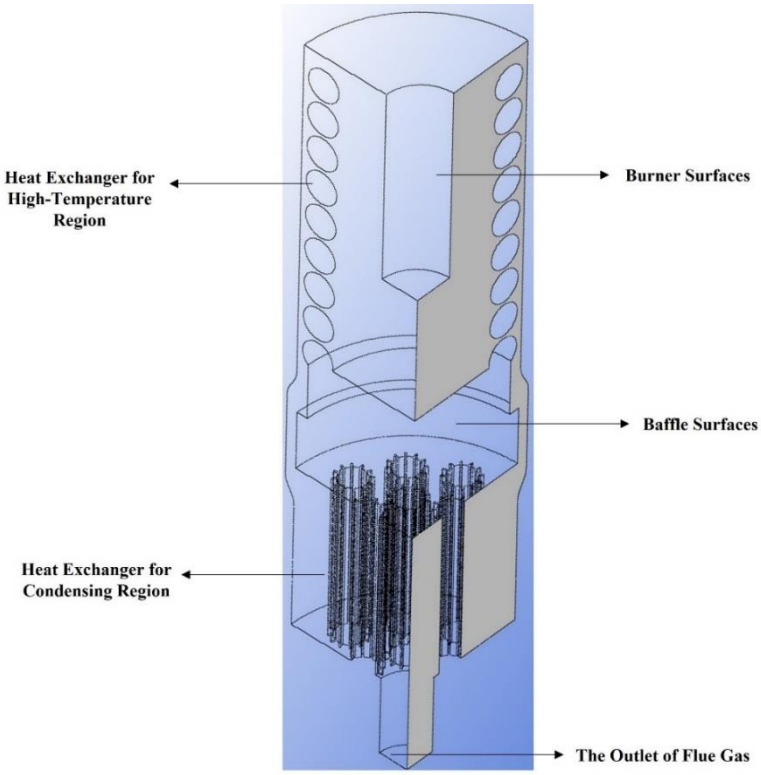


Figure 3.9 The numerical three-dimensional model of the flue gas's air volume

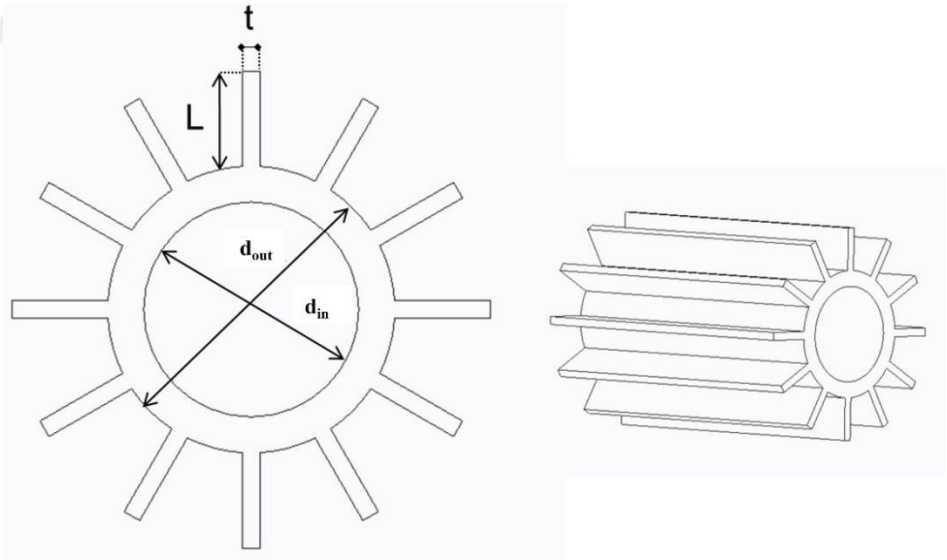


Figure 3.10 The cross-sectional schematic view of the designed heat exchanger for the condensing region

As seen in Figure 3.9, a symmetrical quarter of the cylindrical combustion unit's internal air volume is modelled to reduce the mesh element numbers and decrease the solution times. The heat exchanger surfaces, the burner surface and the baffle surfaces are modelled as flow obstacles by extracting them from the internal air volume.

The fin length (L) and thickness (t) of the finned-tube heat exchanger used in the condensing zone and the cross-section details in Figure 3.10 are chosen as the design parameters. In addition, the number of rows of finned tube heat exchangers that can be used in this region varies according to the fin length (Figure 3.11). All designs keep the finned heat exchanger's inner diameter (d_{in}=18 mm) and the wall thickness (d_{out}=24 mm) constant. Each finned tube heat exchanger has 12 fins. The fin length (L) is chosen in four different values 4 mm, 6 mm, 8 mm and 10 mm. For each fin length, numerical models are created according to three different fin thicknesses (1.5 mm - 2 mm - 2.5 mm). Thus, three-dimensional numerical models are created for 12 different designs given in Table 3.3.

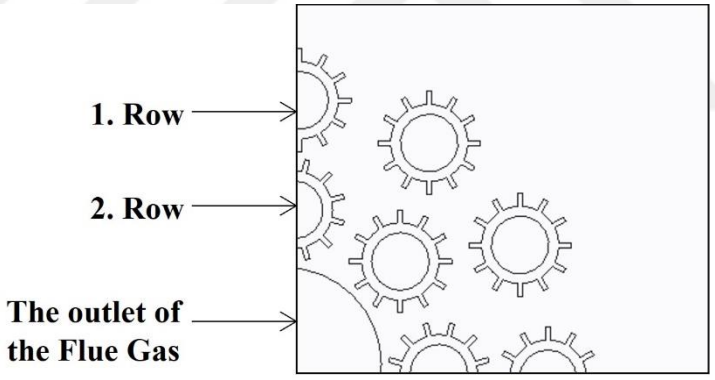


Figure 3.11 The cross-sectional schematic view of the finned tube heat exchangers arrayed in the condensing zone

Table 3.3 Design parameters for twelve different designs

Model No	**Fin Height L [mm]**	**Fin Thickness t [mm]**	**Number of Finned Pipe at 1. Row**	**Number of Finned Pipe at 2.Row**
1	4	1.5	12	8
2	4	2	12	8
3	4	2.5	12	8
4	6	1.5	8	8
5	6	2	8	8
6	6	2.5	8	8
7	8	1.5	8	0
8	8	2	8	0
9	8	2.5	8	0
10	10	1.5	8	0
11	10	2	8	0
12	10	2.5	8	0

After the models are created, the meshing process is the next step for numerical analysis. Appropriate mesh structures of numerical models are created using different mesh technique methods. The mesh element numbers of the numerical models vary between 4.500.000 and 8.500.000 and are shown in Figure 3.12.

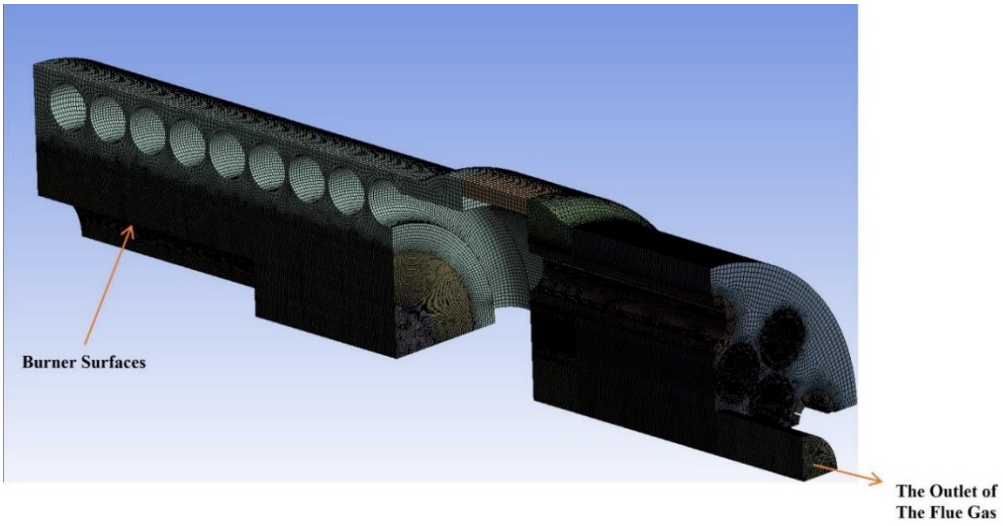


Figure 3.12 The mesh structure for the numerical models

During the numerical solution for the flue gas volumes, 1.1614 kg/m^3 for density (ρ) and 1.59x10^{-5} m^2/s for kinematic viscosity (ν) are used at the thermophysical properties of the air at 300 K temperature (Incropera and Dewitt, 2000).

The boundary conditions of the numerical models are shown schematically in Figure 3.13. The combustible gas (natural gas, etc.) and air mixed in specific proportions pass through the burner surface with the help of a fan and enter the combustion unit. The inlet velocity of this mixture is defined as the boundary condition to the burner surfaces. Considering the desired power and burner surface area in the designed combustion unit, an air intake of 2.85 m/s is determined. The numerical models modelled as one-quarter volume have two symmetry surfaces.

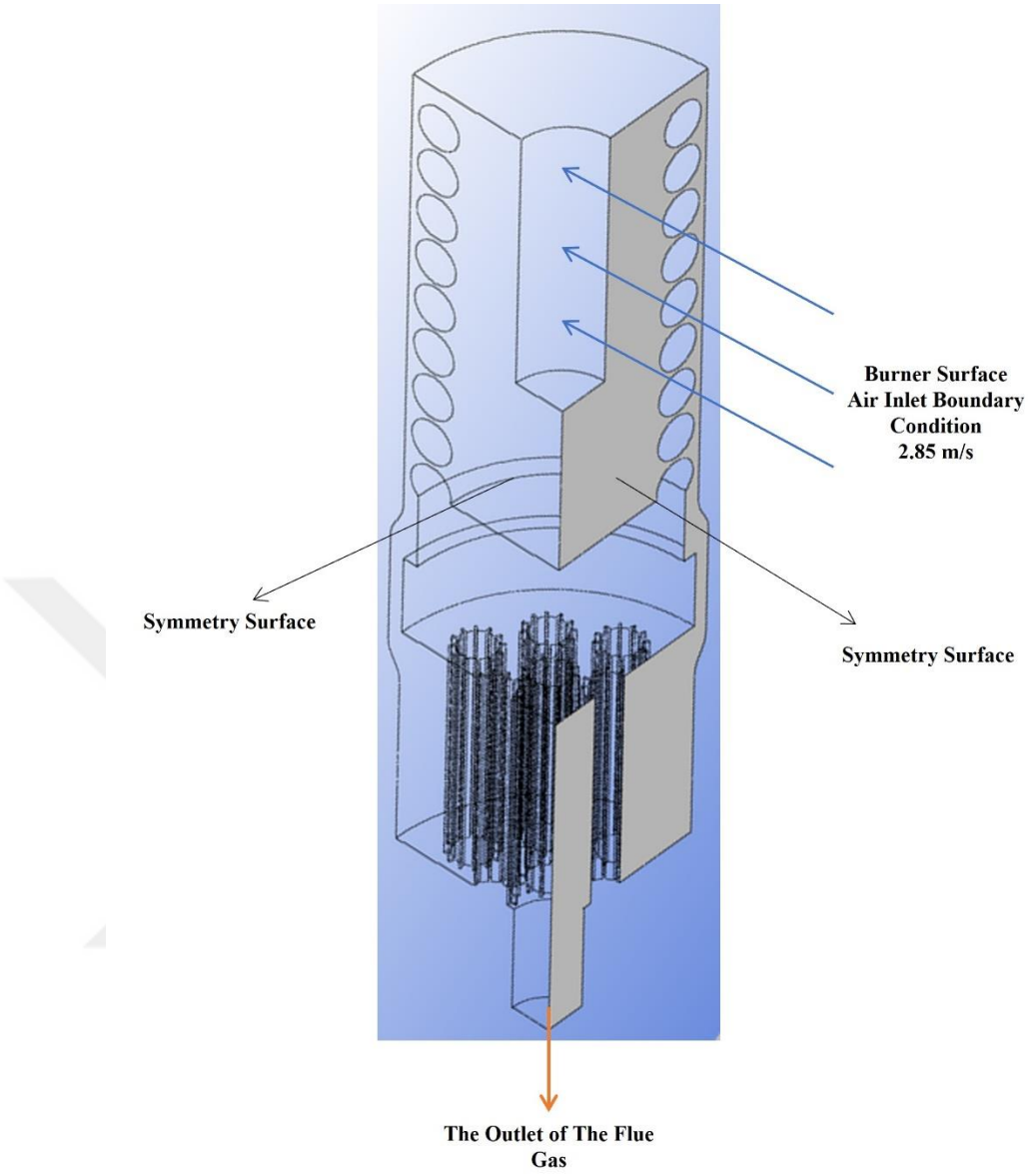


Figure 3.13 The boundary conditions for the numerical models

The flow analyses are only solved to examine the effects of the determined design parameters on the pressure drop and flow characteristics in the combustion unit.

The conditions of the steady-state regime, the natural convection caused by gravity, the forced convection caused by the fan effect and the turbulent flow type conditions are considered.

3.2.1 The Results and Discussion of the Numerical Investigation of the Flue Gas's Flow Characteristics for the Different Heat Exchanger Designs

As a result of the numerical analysis, the effects of each parameter on the pressure drop (Δ_p) in the combustion unit and the total surface area of the finned tube heat exchanger in the condensing zone were investigated separately.

3.2.1.1 The Variation of the Fin Height

The fin thicknesses are kept constant to investigate the effect of change in fin height. Table 3.4 shows the fin height variation's effect on numerical results for a fin thickness of 1.5 mm. In the numerical model with a fin height of 4 mm, 12 finned pipes are fitted in the first row, and eight finned pipes are fitted in the second row. Eight finned pipes at each row are fitted in the same volume for a fin height of 6 mm model. Due to the increased outer diameters, only one row with eight pipes is fitted for 8- and 10-mm model fin heights.

When the fin height is increased from 4 mm to 6 mm, the total surface area of the finned tube decreases by 0.44% and the pressure drop increases by approximately 7% (154 Pa). When the streamlines in Figure 3.14 are examined, the flue gas contacts the finned tube surfaces too much for the 6 mm fin length design. Since most of the total heat transfer in the condensing zone is carried out by convection, it is seen that the best design for a thickness of 1.5 mm is a fin height of 6 mm model.

Since a single-row design can be realised for 8 mm and 10 mm fin heights, a 39% reduction in total surface area is also obtained despite a decrease of up to 39% in pressure drops.

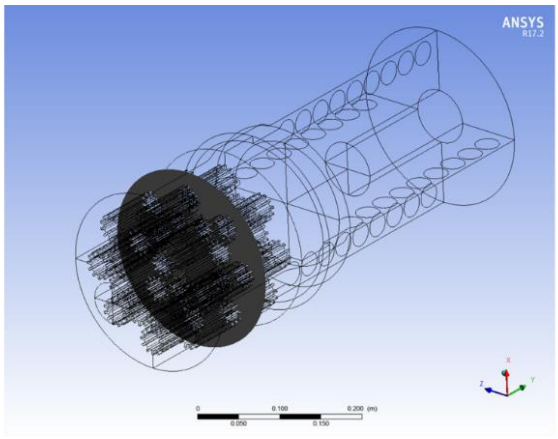
Table 3.4 The effect of fin height variation on numerical results for 1.5 mm fin thickness

Model Number	Fin Height L [mm]	Fin Thickness t [mm]	Number of The Finned Pipe at 1. Row	Number of The Finned Pipe at 2.Row	Total Surface Area of Finned Tube Heat Exchanger [cm^2]	The Rate of Change for Total Surface Area [%]	Pressure Drop Δ_p (Pa)	The Rate of Change for Pressure Drop Δ_p (%)
1	4	1.5	12	8	5349	-	2221	-
4	6	1.5	8	8	5326	-0.44	2375	6.93
7	8	1.5	8	0	3258	-39.09	1350	-39.22
10	10	1.5	8	0	3838	-28.24	1542	-30.57

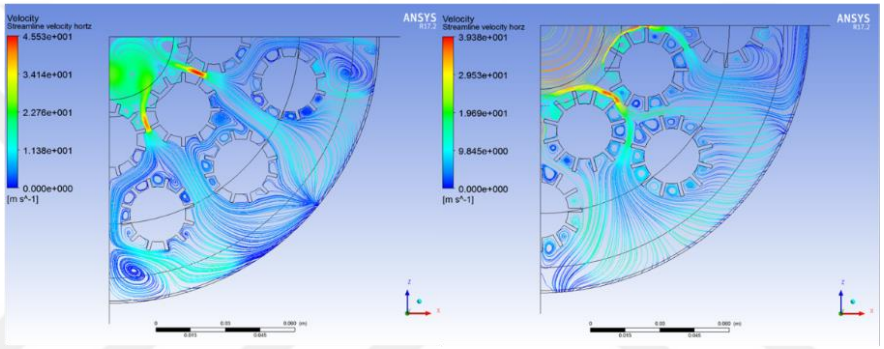
Table 3.5 gives the effect of fin height variation on numerical results for a fin thickness of 2 mm. When it is evaluated with the streamlines in Figure 3.15, results similar to those with the fin height of 1.5 mm are obtained. In the shift from 4 mm to 6 mm fin height, the pressure drops increased by 0.33% and values close to each other were found.

Table 3.5 The effect of fin height variation on numerical results for 2 mm fin thickness

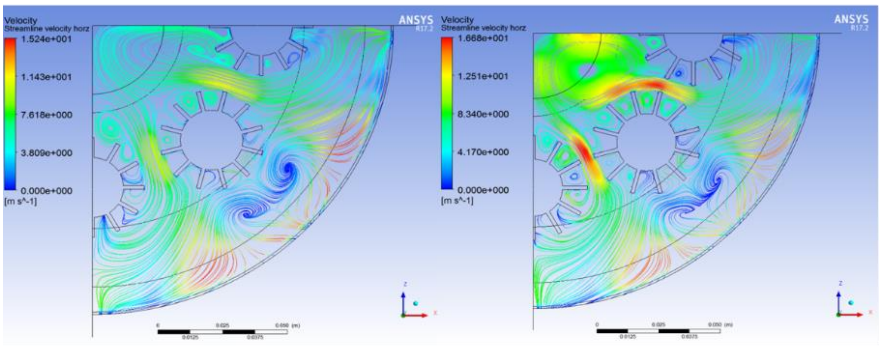
Model Number	Fin Height L [mm]	Fin Thickness t [mm]	Number of The Finned Pipe at 1. Row	Number of The Finned Pipe at 2.Row	Total Surface Area of Finned Tube Heat Exchanger [cm^2]	The Rate of Change for Total Surface Area [%]	Pressure Drop Δ_p (Pa)	The Rate of Change for Pressure Drop Δ_p (%)
2	4	2	12	8	5360	-	2396	-
5	6	2	8	8	5359	-0.01	2404	0.33
8	8	2	8	0	3263	-39.13	1352	-43.57
11	10	2	8	0	3841	-28.35	1500	-37.40



a)



b) c)



d) e)

Figure 3.14 The streamlines for 1.5 mm fin thickness in the middle region of the condensing zone's internal air volume; a) representation of the middle region of the internal air volume of the condensing zone b) streamlines for 4 mm fin length c) streamlines for 6 mm fin length d) streamlines for 8 mm fin length e) streamlines for 10 mm fin length

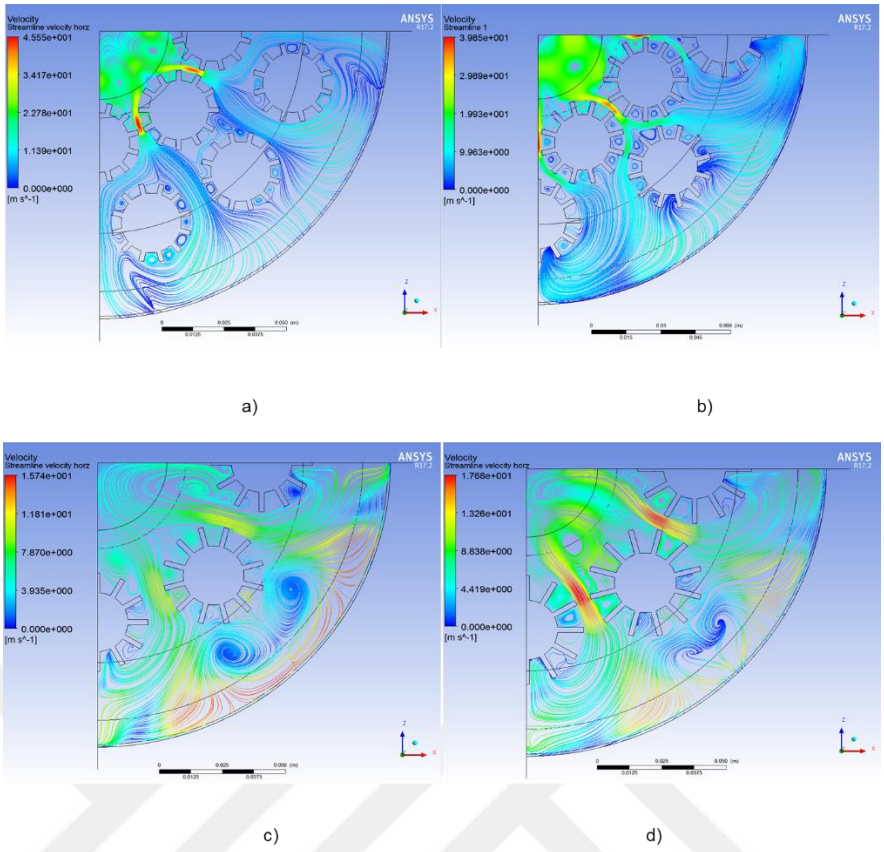


Figure 3.15 The streamlines for 2 mm fin thickness in the middle region of the condensing zone's internal air volume; a) streamlines for 4 mm fin length b) streamlines for 6 mm fin length c) streamlines for 8 mm fin length d) streamlines for 10 mm fin length

Table 3.6 shows the effect of fin height variation on numerical results for a fin thickness of 2.5 mm. When evaluated with the streamlines in Figure 3.16, the results are similar to 1.5 and 2 mm fin height design cases. The pressure drops increased by 13.50% (300 Pa) from 4 mm to 6 mm fin height in the shift. The increment of pressure drop should not be ignored for fin thickness over 2 mm during the design phase.

Table 3.6 The effect of fin height variation on numerical results for 2.5 mm fin thickness

Model Number	Fin Height L [mm]	Fin Thickness t [mm]	Number of The Finned Pipe at 1. Row	Number of The Finned Pipe at 2.Row	Total Surface Area of Finned Tube Heat Exchanger [cm^2]	The Rate of Change for Total Surface Area [%]	Pressure Drop Δ_p (Pa)	The Rate of Change for Pressure Drop Δ_p (%)
3	4	2.5	12	8	5367	-	2185	-
6	6	2.5	8	8	5373	0.12	2480	13.50
9	8	2.5	8	0	3264	-39.19	1319	-39.63
12	10	2.5	8	0	3848	-28.31	1477	-32.40

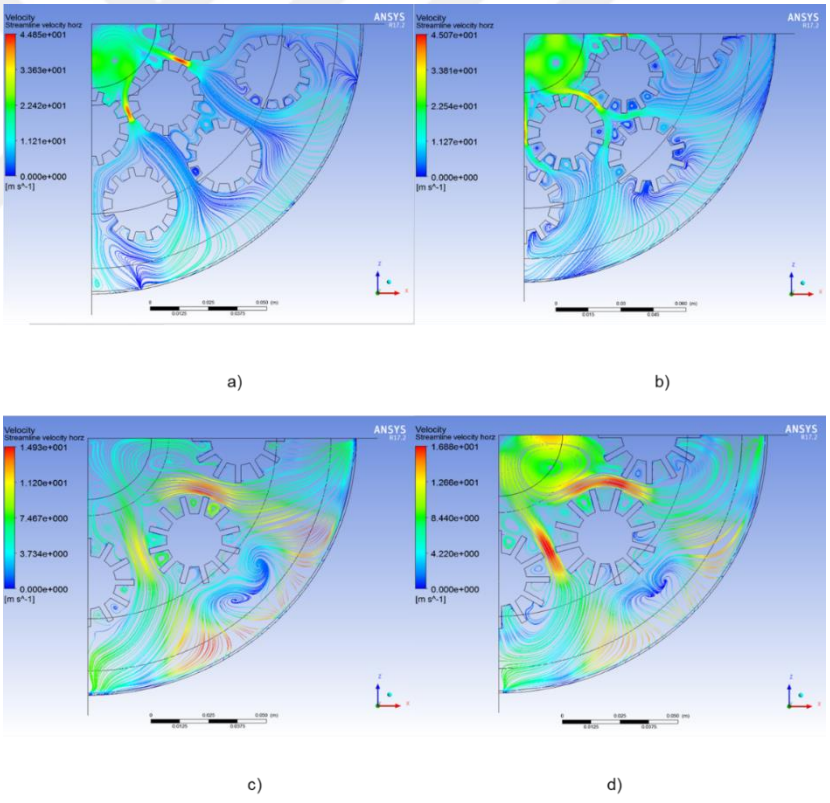


Figure 3.16 The streamlines for 2.5 mm fin thickness in the middle region of the condensing zone's internal air volume; a) Streamlines for 4 mm fin length b) Streamlines for 6 mm fin length c) Streamlines for 8 mm fin length d) Streamlines for 10 mm fin length

3.2.1.2 The Variation of the Fin Thickness

The fin heights are kept constant in order to examine the effect of the fin thickness variation. Table 3.7, 3.8, Table 3.9, and Table 3.10 gives the effect of the fin thickness variation on numerical results for each fin height. At the same fin heights, the variation in fin thickness did not significantly affect the pressure drop. For the design case of fin height of 4 mm, incrementing the fin thickness from 1.5 mm to 2 mm creates a 7.88% rise in pressure drop. However, this change does not reach 3% in other fin heights.

Table 3.7 The effect of fin thickness variation on numerical results for 4 mm fin height

Model Number	**Fin Height L [mm]**	**Fin Thickness t [mm]**	**Number of The Finned Pipe at 1. Row**	**Number of The Finned Pipe at 2.Row**	**Total Surface Area of Finned Tube Heat Exchanger [cm^2]**	**The Rate of Change for Total Surface Area [%]**	**Pressure Drop Δ_p (Pa)**	**The Rate of Change for Pressure Drop Δ_p (%)**
1	4	1.5	12	8	5349	-	2221	-
2	4	2	12	8	5360	0.20	2396	7.88
3	4	2.5	12	8	5367	0.33	2185	-1.62

Table 3.8 The effect of fin thickness variation on numerical results for 6 mm fin height

Model Number	**Fin Height L [mm]**	**Fin Thickness t [mm]**	**Number of The Finned Pipe at 1. Row**	**Number of The Finned Pipe at 2.Row**	**Total Surface Area of Finned Tube Heat Exchanger [cm^2]**	**The Rate of Change for Total Surface Area [%]**	**Pressure Drop Δ_p (Pa)**	**The Rate of Change for Pressure Drop Δ_p (%)**
4	6	1.5	8	8	5326	-	2375	-
5	6	2	8	8	5360	0.64	2404	1.22
6	6	2.5	8	8	5373	0.89	2480	4.42

Table 3.9 The effect of fin thickness variation on numerical results for 8 mm fin height

Model Number	Fin Height L [mm]	Fin Thickness t [mm]	Number of The Finned Pipe at 1. Row	Number of The Finned Pipe at 2.Row	Total Surface Area of Finned Tube Heat Exchanger [cm^2]	The Rate of Change for Total Surface Area [%]	Pressure Drop Δ_p (Pa)	The Rate of Change for Pressure Drop Δ_p (%)
7	8	1.5	8	0	3258	-	1350	-
8	8	2	8	0	3263	0.14	1352	0.15
9	8	2.5	8	0	3264	0.16	1319	-2.30

Table 3.10 The effect of fin thickness variation on numerical results for 10 mm fin height

Model Number	Fin Height L [mm]	Fin Thickness t [mm]	Number of The Finned Pipe at 1. Row	Number of The Finned Pipe at 2.Row	Total Surface Area of Finned Tube Heat Exchanger [cm^2]	The Rate of Change for Total Surface Area [%]	Pressure Drop Δ_p (Pa)	The Rate of Change for Pressure Drop Δ_p (%)
8	10	1.5	8	0	3838	-	1542	-
9	10	2	8	0	3841	0.06	1500	-2.72
10	10	2.5	8	0	3848	0.24	1477	-4.22

As a result, the pressure drops and the flow characteristics of flue gas inside the combustion unit of the condensing boiler can be investigated numerically in terms of the different heat exchanger designs. The numerical results can give a preliminary remark regarding comparing the design cases during the designing phase.

3.3 The Numerical Investigation of the Flow Characteristics of the Flue Gas Movement Inside the Combustion Unit Modelling with the Air Domain and Flue Gas Domain

The air domain was used to model the flue gas for the previous two studies. We do not know whether there is a significant difference in the numerical results when the air or combustible gas mixture domain is used as flue gas. According to the literature survey, no study has evaluated this issue for condensing boilers. This study aims to clarify the open point with the control study. The basic control volumes are modelled for the internal flue gas to decrease the effect of model complexity on the pressure drop and flow characteristic of flue gas movement in the combustion unit. Numerical analyses are executed according to the thermophysical properties of air and combustible gas mixture for two basic control volume structures. The experimental control setups are configured and performed to determine the features of the combustible gas mixture for numerical analyses. The details of the experimental studies are given in Chapter 4.1. Numerical results are validated with experimental results.

The general operating principle of the condensing boiler with heat recovery equipment examined in this study is given in Figure 3.17. The combustible gas (natural gas) and fresh air enter the combustion unit of the boiler at certain rates. The high-temperature flue gas from the combustion reaction is directed to the heat recovery device. At the same time, cold water enters this device. The water vapour in the flue gas in the heat recovery device loses its latent heat and turns into a liquid phase when it falls below the condensation temperature. This water returning to the liquid phase is called condensation water. Condensate is discharged from the heat recovery device drain. The low-temperature flue gas is sent to the atmosphere through the discharge pipe.

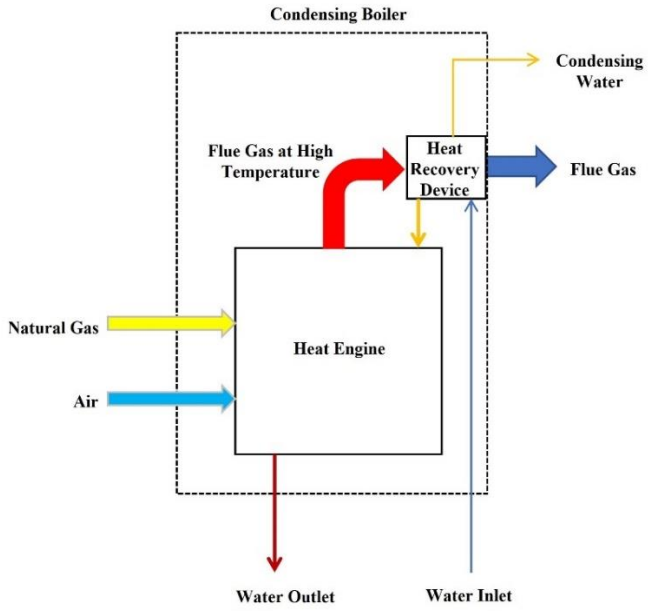


Figure 3.17 The schematic view of the general operation principle for the condensing boiler with a heat recovery device

As mentioned before, these heat exchangers' surface qualities and designs are often complex. To minimise the effect of uncertainties coming from the design and to determine the suitability of the experimental measurement method, the internal volume of the first basic heat recovery device is modelled and shown in Figure 3.18.

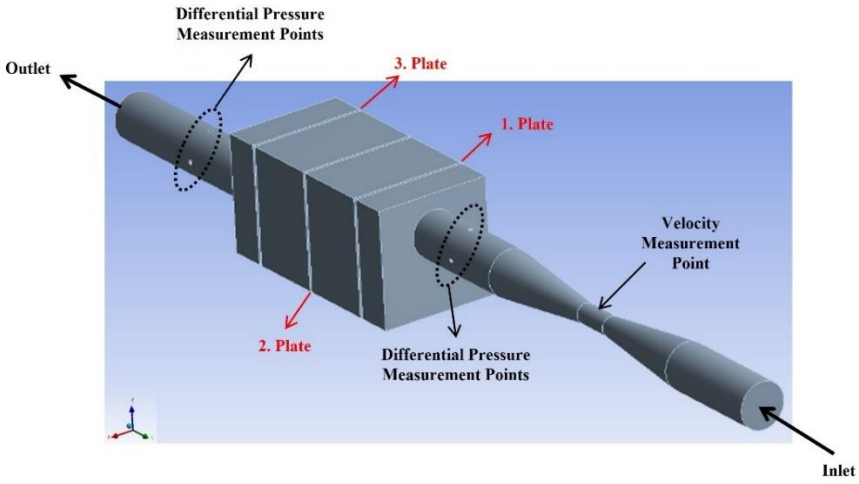


Figure 3.18 The three-dimensional numerical model for the internal volume of the first basic heat recovery device

This basic recovery device has a special control volume. It has got three stainless steel plates with several holes. These plates are hermetically assembled at certain distances. The holes on the plates are drilled, staggered and placed in the positions in Figure 3.19.

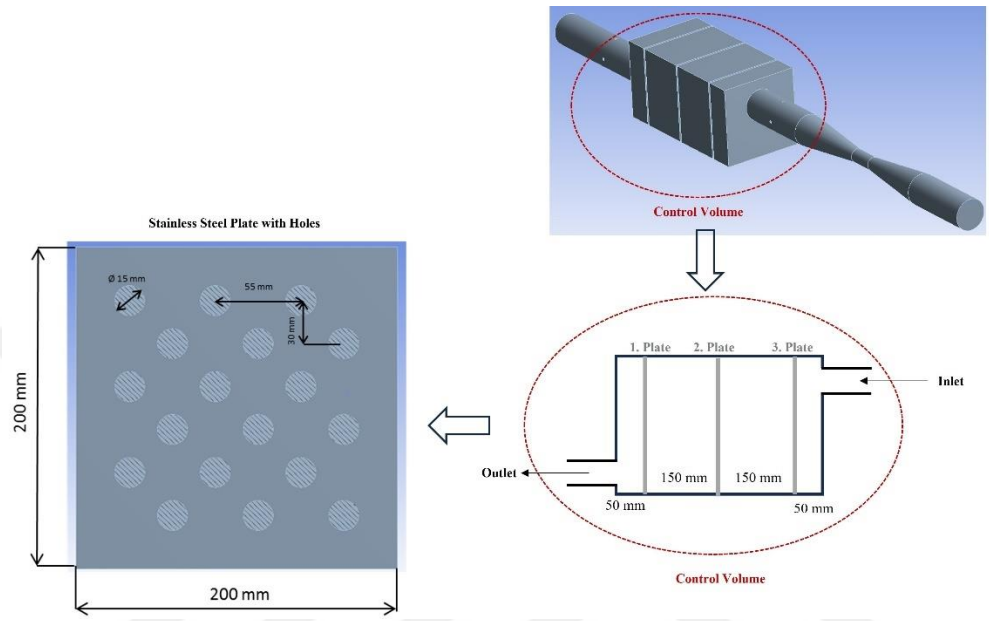


Figure 3.19 The schematic view of the control volume

After the models are created, the meshing process is the next step for numerical analysis. Appropriate mesh structures of numerical models are created using different mesh technique methods. The mesh element number of the numerical model is 9.732.840, shown in Figure 3.20.

For the air domain, 1.1780 kg/m^3 for density (ρ) and 1.57x10^{-5} m^2/s for kinematic viscosity (ν) are used at the thermophysical properties of the air at 297 K temperature (Incropera and Dewitt, 2000). The detail of the experimental study is given in Chapter 4.1, and the measured nine inlet velocities of air (Table 3.11) are defined in numerical studies as a boundary condition.

Table 3.11 The inlet velocities for the boundary condition of the air domain

Inlet velocities of air (m/s)	4.30 – 6.85 – 8.31 – 9.36 – 14.34 – 17.71 – 21.39 – 21.88 – 21.93

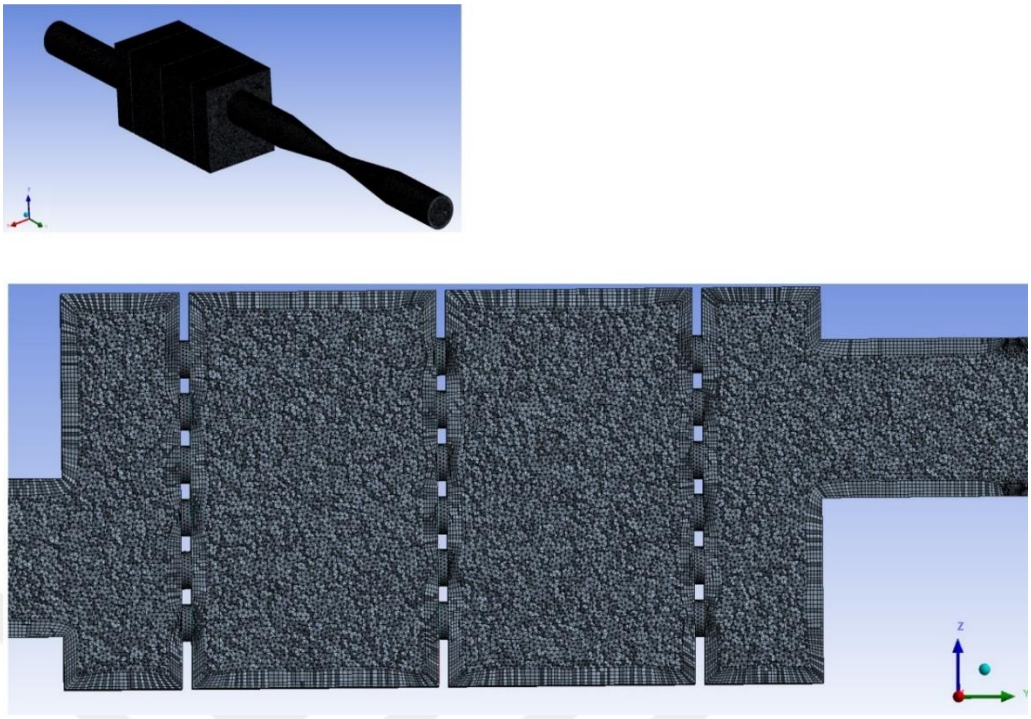


Figure 3.20 The mesh structure for the numerical model

Flow analyses are solved to numerically find the pressure drop in the control volume.

The conditions of the steady-state regime, the natural convection caused by gravity, the forced convection caused by the fan effect and the turbulent flow type conditions are considered.

The experimental and numerical results of the pressure drops in the control volume are compared in the graph given in Figure 3.21. When the graph is examined, the experimental and numerical results are in the same trend, with a 5.6% average difference between the results. Thus, the numerical method is validated for air volume.

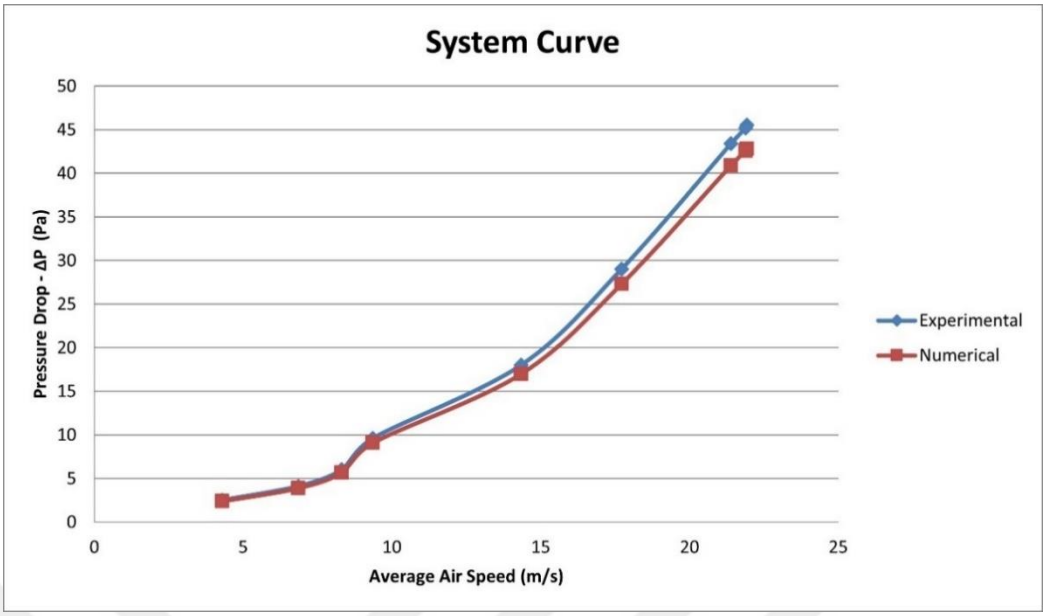


Figure 3.21 The comparison graph for experimental and numerical results of the pressure drops

After the numerical method is validated, the experimental and numerical studies are repeated for the flue gas using the same experimental setup. The experimental setup is connected to the flue outlet of a wall-hang heating appliance. The experimental setup and its detailed information are given in Chapter 4.1.

The experimental study is performed to determine flue gas composition and temperature for the flue gas domain. According to the experimental results, 1.6609 kg/m^3 for density (ρ) and $1.06x10^{-5}$ m^2/s for kinematic viscosity (ν) are used at the thermophysical properties of the CO_2 at 321 K temperature. Furthermore, 1.0555 kg/m^3 for density (ρ) and $1.79x10^{-5}$ m^2/s for kinematic viscosity (ν) are used at the thermophysical properties of the N_2 at 321 K temperature (Incropera and Dewitt, 2000). The inlet velocity is measured at 9.06 m/s and defined as a boundary condition.

The same numerical model and mesh structure were also used in the numerical study of the flue gas volume.

In the solution of the numerical model of the second experiment in which flue gas is used as a fluid, the conditions of the steady regime, natural convection caused by gravity, forced convection caused by fan effect and turbulent flow type conditions are considered.

As a result of the numerical study, a pressure drop of 27.62 Pa is found in the first basic control volume. This value is measured as 28.48 Pa in the experimental study. The numerical model is also experimentally verified using the flue gas as the fluid.

3.3.1 The Results and Discussion of the Numerical Investigation of the Flow Characteristics of the Flue Gas Movement Inside the First Basic Control Volume Modelling with the Air Domain and Flue Gas Domain

Figure 3.22 shows the streamlines inside the internal volume of the first basic heat recovery device at the 9.5 m/s fluid velocity modelling with the air and flue gas domain. Plane 1 is created at the middle location of the control volume. Different flow movements are obtained at the Plane 1 region for both domains at the same fluid velocity when comparing the flow characteristics. It shows us that modelling the flue gas domain instead of the air is important for numerical analyses of the condensing boiler's combustion unit.

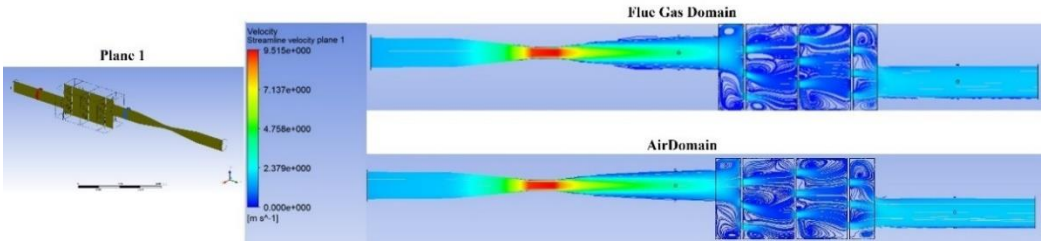


Figure 3.22 The streamlines inside the internal volume of the first basic heat recovery device at the 9.5 m/s fluid velocity modelling with the air and flue gas domain

Another result obtained from experimental and numerical studies is that when the fluid is modelled as air and flue gas for the same volumetric flow rates, there are huge differences in pressure drops. In the studies carried out with air and the flue gas in the control volume made of perforated stainless plates, different pressure drops close to 3 times were obtained for the same volumetric flow conditions. Experimental and numerical results are given in Table 3.12. As a result, modelling the fluid volume as air instead of flue gas in numerical studies of wall-hang heating appliances could reveal different results as flow characteristics.

Table 3.12 The comparison of the results for modelling the air and flue gas inside the first basic control volume

Domain	Average velocity (m/s)	Experimental ΔP (Pa)	Numerical ΔP (Pa)
Air	9.36	9.60	9.08
Flue Gas	9.06	28.48	27.62
Percentage Difference		196.67%	204.19%

3.3.2 The Results and Discussion of the Numerical Investigation of the Flow Characteristics of the Flue Gas Movement Inside the Second Basic Control Volume Modelling with the Air Domain and Flue Gas Domain

After the numerical model is validated with experimental results for the first basic heat recovery's control volume, the second basic heat recovery's control volume is prototyped, which has a more complex heat exchanger and is used for the real condensing heating appliances with heat recovery technology. Its working principle is explained in Figure 3.17.

A new control volume has been created with the heat exchangers used in the heat recovery equipment (recuperator) of wall-hang condensing heating appliances. These heat exchangers are manufactured with an aluminium casting technique. The cross-sectional view of the control volume and the locations of the heat exchangers are given in Figure 3.23.

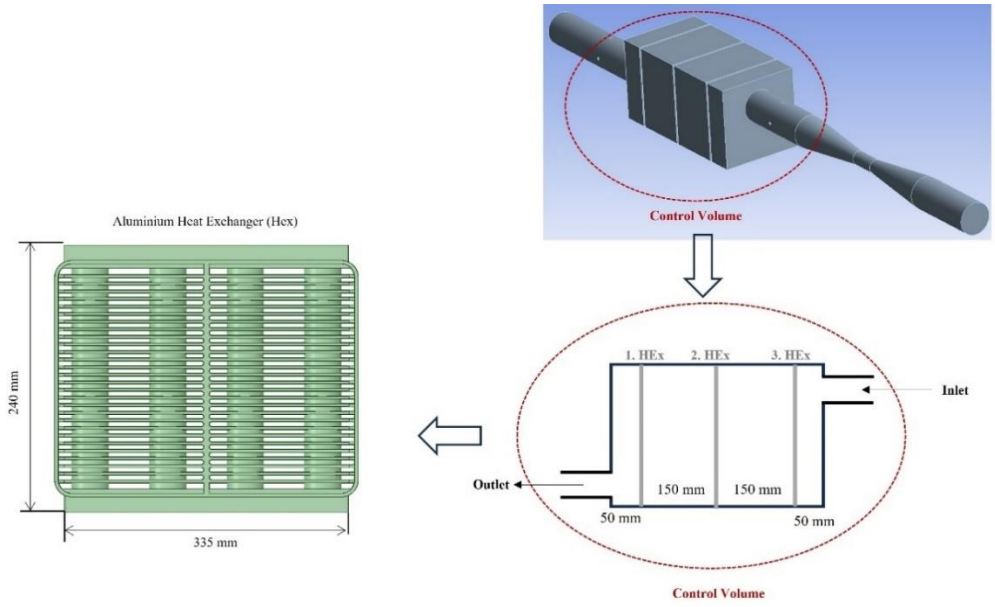


Figure 3.23 The schematic view of the control volume of the second basic heat recovery model

The flue gas volume of the experimental setup is numerically modelled and shown in Figure 3.24. Its experimental setup and test details are given in Chapter 4.1.

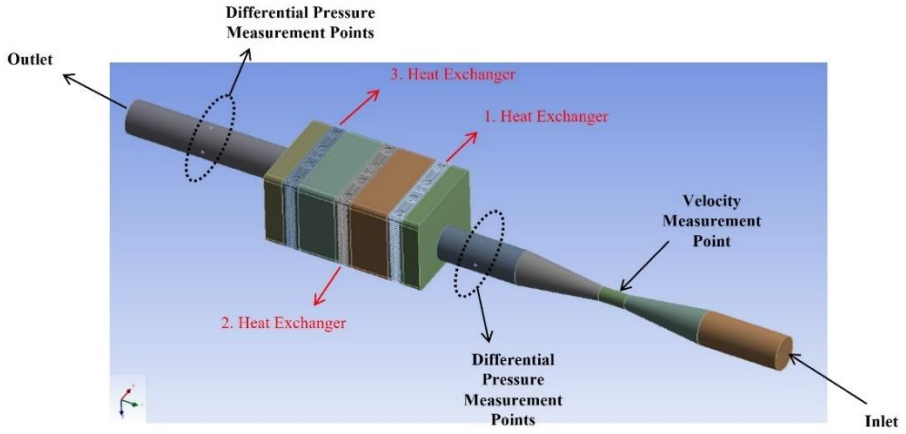


Figure 3.24 The three-dimensional numerical model for the internal volume of the second basic heat recovery device

The appropriate mesh structure of the numerical model is created by using different mesh technique methods together. The mesh element number of the numerical model is 20.025.824 and is shown in Figure 3.25.

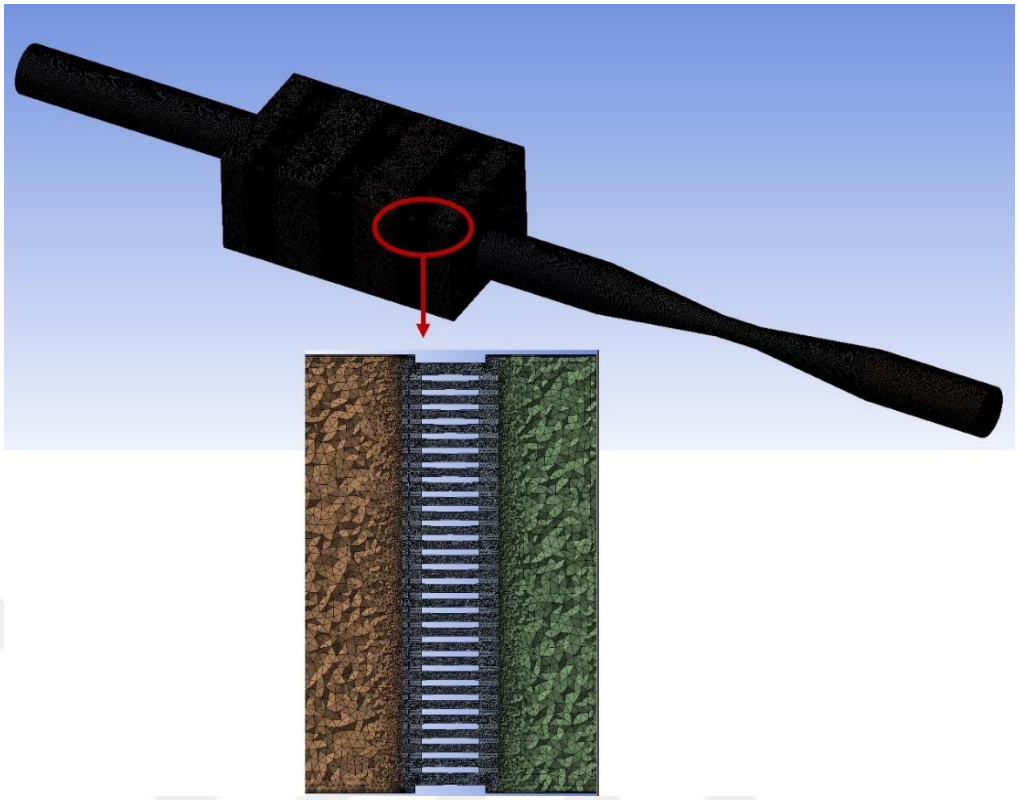


Figure 3.25 The mesh structure for the numerical model of the second basic heat recovery device

The boundary conditions of the numerical model are determined with an experimental setup, which is explained in Chapter 4.1. The temperature and emission measurements of the flue gas from the flue outlet and the velocity and the control volume's pressure drop values of the flue gas are measured simultaneously. The average velocity of the flue gas is 9.40 m/s, the average temperature of the flue gas is 48.4 C°, and the pressure drop (ΔP) of the control volume is 11.10 Pa are obtained.

According to the experimental results, 1.6609 kg/m^3 for density (ρ) and 1.06x10^{-5} m^2/s for kinematic viscosity (ν) are used at the thermophysical properties of the CO_2 at 321 K temperature. Furthermore, 1.0555 kg/m^3 for density (ρ) and 1.79x10^{-5} m^2/s for kinematic viscosity (ν) are used at the thermophysical properties of the N_2 at 321 K temperature (Incropera and Dewitt, 2000). The inlet velocity is measured at 9.40 m/s and defined as a boundary condition.

The conditions of the steady-state regime, the natural convection caused by gravity, the forced convection caused by the fan effect and the turbulent flow type conditions are considered like the numerical model of the first basic heat recovery device.

When the results of the numerical study are examined, the pressure drop in the control volume is found as 10.42 Pa. This value is also measured as 11.10 Pa experimentally. As can be seen, the numerical results align with the experimental results. In Figure 3.26, the flow characteristic of the experimental setup is obtained with the streamlines. In addition, the flow and eddy regions on the heat exchangers in the control volume are shown in detail in Figure 3.27.

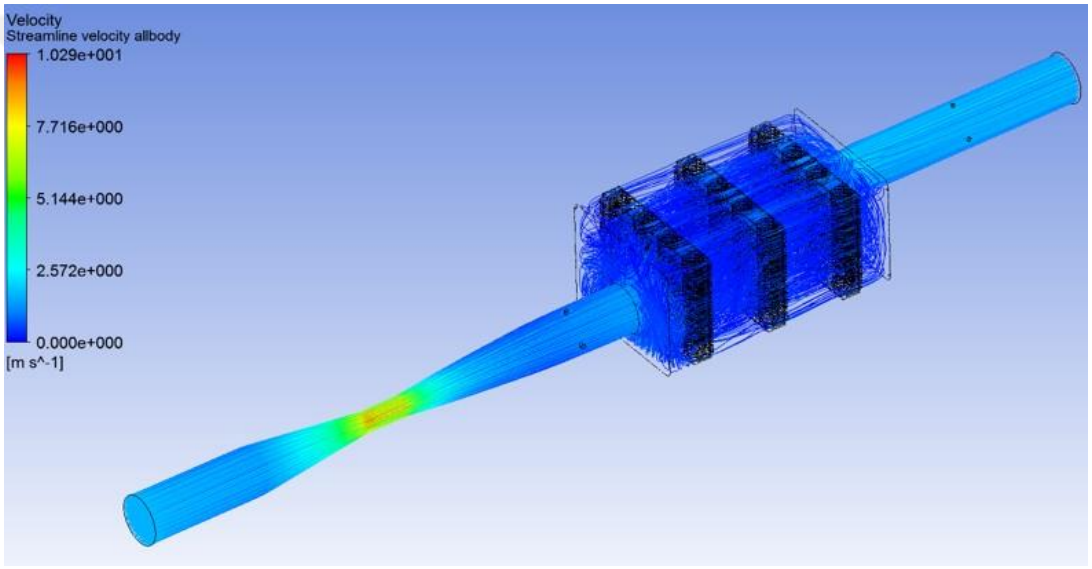


Figure 3.26 The streamlines inside the internal volume of the second basic heat recovery device

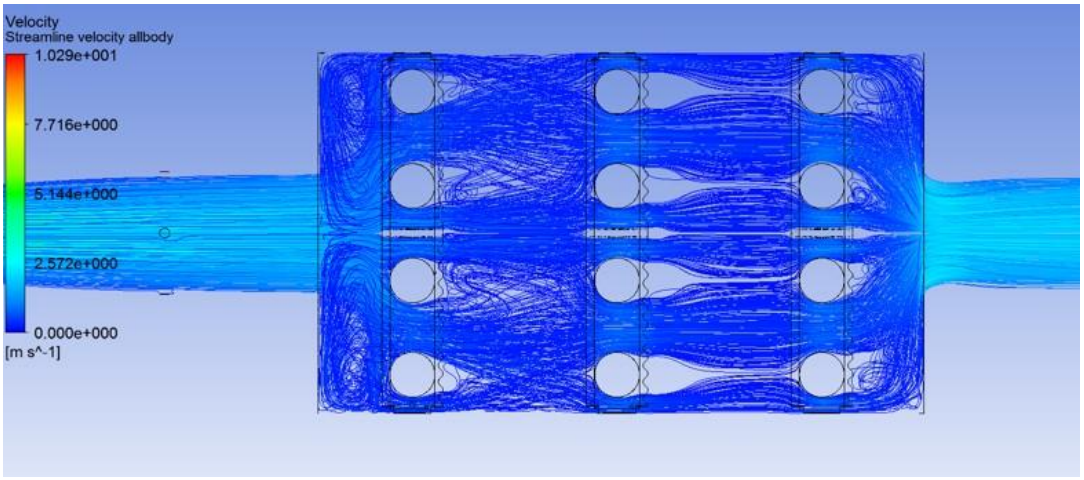


Figure 3.27 The detail streamlines inside the control volume of the basic heat recovery device

Even if the control volume consists of an aluminium-casting heat exchanger or a stainless plate, the numerical results for the flue gas domain align with the experimental studies (Table 3.13). In both studies, the combustion reaction (10.9% CO_2 emission) in the wall-hang heating appliance is the same. Although the volumetric flow rates of the flue gas are close to each other, there are close to 2.5 times differences between the pressure drops. When the numerical model of the flue gas is defined correctly, the flow characteristics resulting from the design difference can be obtained numerically.

Table 3.13 The comparison of the results for the different control volumes modelled with the flue gas domain

Control Volume	**Average velocity [m/s]**	**Experimental ΔP [Pa]**	**Numerical ΔP [Pa]**
Aluminium Heat Exchanger	9.40	11.10	10.42
Stainless Steel Plate	9.06	28.48	27.62
Percentage Difference		156.58%	165.07%

Experimental studies verify the numerical flue gas and air domain models using controlled experimental setups and control volumes. In this way, it has been obtained that the flue gas domain should be modelled as the fluid type for the numerical studies of the combustion units used in the condensing boiler and heating appliances.

As a result of this study, the pressure drops and flow characteristics due to design differences can be modelled in detail. In this way, it is possible to determine the appropriate fan selection required during the design of condensing boilers or detailed information about the flue gas's movement without performing an experimental study. This investigation method can provide a great advantage regarding prototype costs and times during the design phase.

3.4 The Investigation of the Impact of Design Parameters of the Condensing Boiler's Heat Exchanger on Boiler Performance

After validating the flue gas domain used in numerical analyses of a condensing boiler's combustion unit or heat engine, the impact of heat exchanger design parameters on heat engine performance is investigated.

Heat exchangers are crucial for the thermal performance of condensing wall-hang heaters. The heat transferred from flue gas to water depends on the design of the heat exchanger. Recently, aluminium-finned tube-type heat exchangers have been preferred over stainless-steel heat exchangers in condensing heat engines.

This study examines how computational fluid dynamics and heat transfer (CFDHT) can optimize the design of finned tube heat exchangers for use in condensing wall-hung boilers (WHBcs). The input design parameters are fin height, thickness, and space, while the CFDHT method models the internal volume of the heat engine. The study determines the total heat transfer on the inner surface of the tube, the maximum temperature on the fins, the total heat transfer per unit volume of the heat exchanger, and the pressure drop between the inlet and outlet of the internal volume. The study creates 350 design cases to complete the parametric study with numerical results. The numerical results of these design cases form the data set for the artificial neural network modelling presented in Chapter 5.1.

A diagram in Figure 3.28 shows the heat engine unit of a condensing wall hang boiler (WHBc). Flammable gas and fresh air are mixed in specific proportions in the mixer to limit CO and CO_2 emissions according to standards. The heat exchanger transfers heat energy to the water through conduction, convection, and radiation. The water vapour in the flue gas becomes condensing water when it loses its latent heat and returns to the heat engine unit's drainage. The flue gas is sent to the atmosphere by the flue gas pipe.

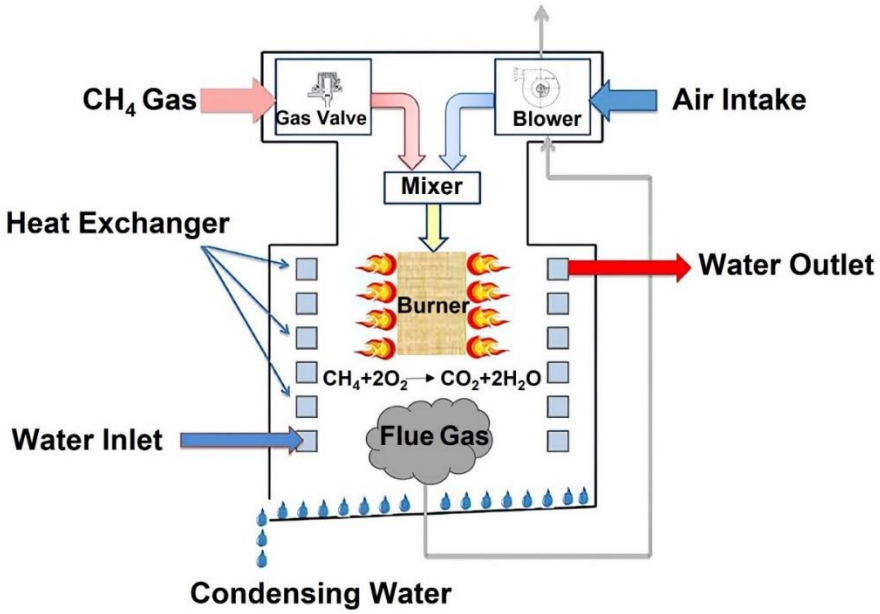


Figure 3.28 Schematic representation of the working principle of the heat engine unit of a condensing wall-hang heating appliance

The main component of the condensing heat engine is the helical finned tube heat exchanger. It provides heat transfer between the water domains and flue gas. The heat engine's internal volume in Figure 3.29 is numerically modelled in 3D to determine the heat exchanger's capacity or total heat transfer to the water. This volume includes the part where the flue gas, formed in the burner, flows over the heat exchanger and outlet. The symmetrical area investigated numerically in 3D is shown in Figure 3.30. The tube pipe has repeated fins illustrated as dotted lines.

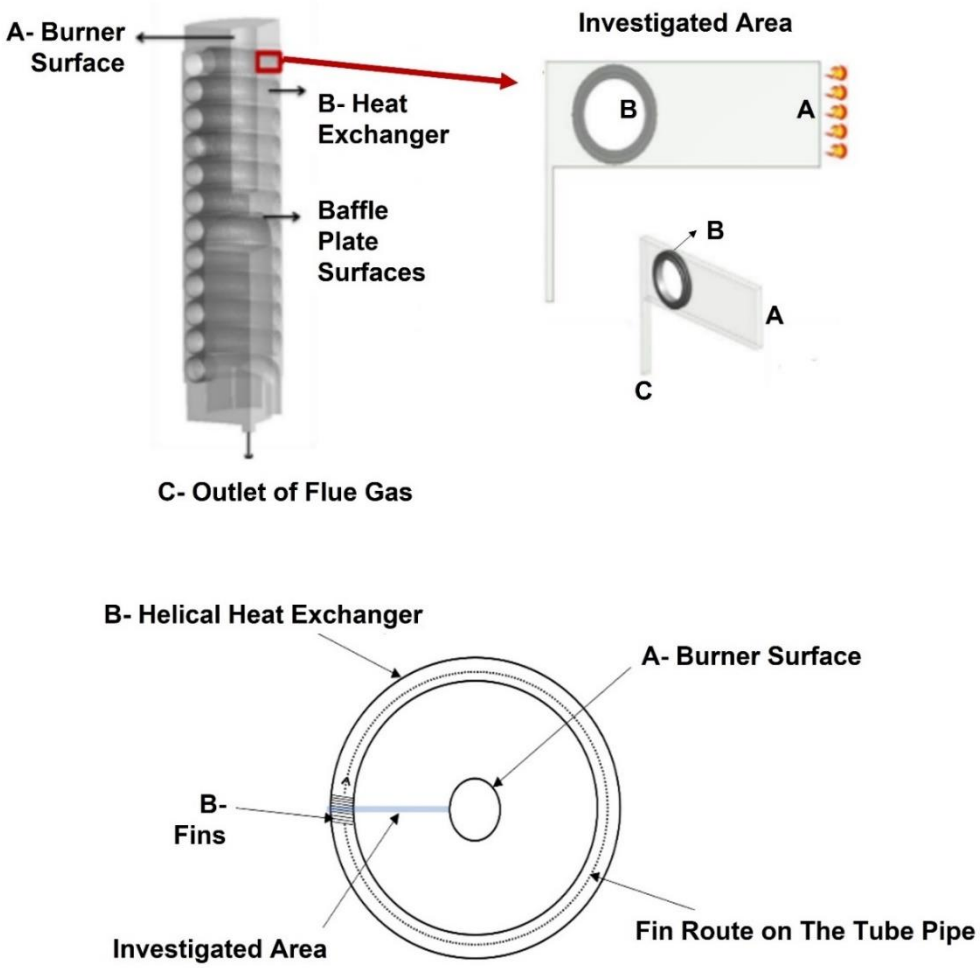


Figure 3.29 The modelled internal volume of the heat engine

In Figure 3.30, the numerical model defines the "flue gas" as the fluid domain and the "finned tube heat exchanger" as the solid domain. The water domain inside the heat exchanger is considered the boundary condition.

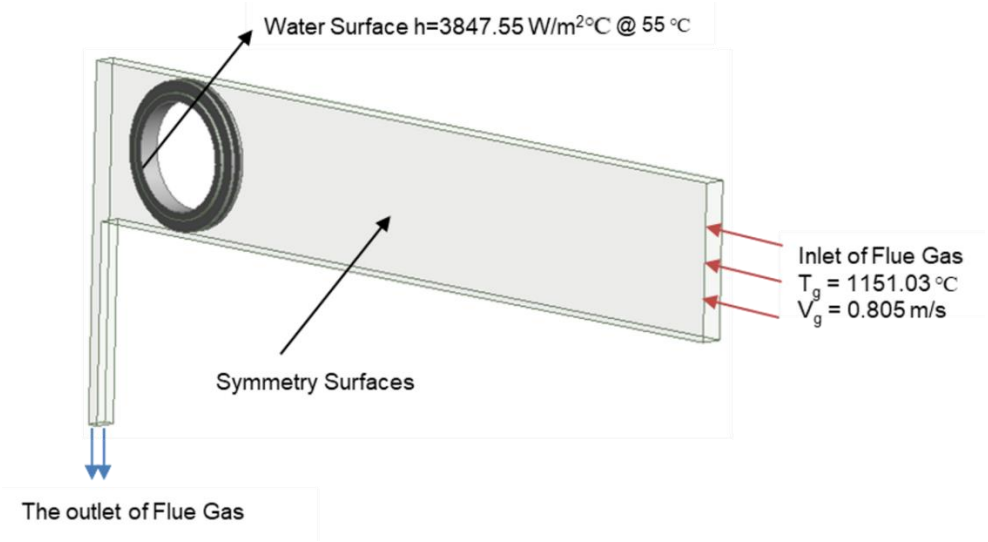


Figure 3.30 The numerical model and boundary conditions

The aluminium heat exchanger has a helical coil tube in real condition. Therefore, the literature investigated to determine the calculation of the heat transfer coefficient for the helical coil pipe inner flow. Seban and McLaughlin performed an experimental study to determine the heat transfer coefficient in helical coil tubes (Seban and McLaughlin, 1963). According to this study, Equation 1 provides to calculate the heat transfer coefficient for turbulent flow.

$$\frac{hd}{k}\left(\frac{\upsilon}{\alpha}\right)^{-0.4} = \frac{f}{8}\frac{U_m\, d}{\upsilon} \tag{3.1}$$

"d" is the tube inside diameter, and "D_h" is the coil diameter to the tube centre. All numerical models have the same d value (30 mm). D_h for the helical coil tube is modelled to provide small coil acceptance (Seban and McLaughlin, 1963), and all numerical models have the same D_h value. According to the EN15502 standard, the performance of the condensing wall hang boilers is tested for 80 ℃ - 60 ℃ and 50 ℃ - 30 ℃ operating conditions (EN 15502 -1:2012+A1:2015, 2015). The film temperature of the water inside the tube coil is calculated as 55 ℃ (average temperature of operating conditions). This film temperature of the water is used to determine the thermal conductivity (k), thermal diffusivity (α) and kinematic viscosity (ν). The mean velocity (U_m) is calculated according to the inner diameter of the heat exchanger and the water flow rate passed inside the tube. The water flow rate is selected as 17 lt/min. The Weisbach friction factor (f) is determined from the graph of

Reynolds number – friction factor according to the turbulent flow and small coil criteria (Seban and McLaughlin, 1963).

Finally, the new heat transfer coefficient (h) of the waterside is calculated as 3847.55 W/m^{2}K for the below conditions:

- Water temperature 55 ℃
- Water flow rate 17 lt/min
- D_h/d= 17; small coil acceptance (Seban and McLaughlin, 1963)

As mentioned, the flue gas is modelled as a fluid domain according to the combustion gas mixture. The mass fraction of the combustion gases is used from the previous study (Yılmaz, Kumlutaş, Yücekaya and Cumbul, 2021). This prediction of mass fractions is made for 100 % methane gas (G20) and an air-gas equivalent ratio (φ) of 0.75. Table 3.14 gives the composition of the combustion gases.

Table 3.14 The composition of the combustion gases @ G20 (100% CH_4) & φ =0.75

Combustion Gas	O_2	N_2	CO_2	H_2O	CO	NO	H	H_2	O	OH
Mass Fraction [%]	4.705	73.139	7.426	14.274	0.023	0.300	0.001	0.011	0.008	0.114

Flue gas temperature is calculated as 1151.03 ℃ with a program (Cumbul, 2018) created in the master thesis based on the equations and formulations inside the NASA report SP-3001 (NASA report SP-3001, 2018). The flue gas temperature is calculated according to the CO_2 mass fraction inside the combustion gases. The assumption of the ideal combustion is considered, and the base equation is given below.

$$\frac{C_p^\circ(T)}{R} = a_1T^{-2} + a_2T^{-1} + a_3 + a_4T + a_5T^2 + a_6T^3 + a_7T^4 \qquad (3.2)$$

The investigated condensing heat engine has a premix combustion unit. This unit provides the gas/air mixture, which can be adjusted to the desired value. It comprises a radial fan, pneumatic gas valve, venture, and stainless-steel multi-hole burner. This gas/air mixture passes through multi-holes of the burner. The average velocity of the

flue gas created after the combustion process is equal to the gas/air mixture. The average velocity of the flue gas is calculated according to the gas/air volumetric flow and the lateral area of the stainless-steel multi-hole burner. When the 24 kW input load is attained from the heat engine used with methane gas (G20), a 55.65 m3/h volumetric flow of gas-air mixture is needed for a 0.75 air-gas equivalent ratio (φ). The lateral area of the burner of the heat engine is 0.0192 m^2 for that input load. Consequently, the flue gas velocity is obtained as 0.805 m/s for the boundary condition of the numerical model.

The selected design parameters of the aluminium heat exchanger are fin height (h_f), fin thickness (t_f), and fin spacing (s). The values of these parameters are given in Table 3.15. All values for design parameters are selected according to manufacturing conditions. The inner pipe diameter and thickness are kept the same for all models.

Table 3.15 The variation of design parameters

Design Parameter (Input Parameter)	**Values [mm]**
Fin Height (h_f)	1, 2, 3, 4, 5, 6, 7, 8, 9, 10
Fin Thickness (t_f)	0.5, 1, 1.5, 2, 2.5
Fin Spacing (s)	1, 1.5, 2, 2.5, 3, 3.5, 4

According to the combination of design parameters' values, 350 different numerical models are created.

The next step for the numerical analysis is the meshing process. Optimized meshing structures for numerical models have been created using different meshing techniques. The number of mesh elements of numerical models varies according to the model between 550.733 and 1.128.369.

During the numerical solution, 167 W/m°C thermal conductivity coefficient and 0.42 emissivity coefficient values of 6000 series aluminium material at room temperature conditions are entered for the heat exchanger solid model (Incropera and Dewitt, 2000).

Continuous regime, radiation effects, natural convection caused by gravity, forced convection caused by fan effect and turbulent flow type conditions are considered.

Each numerical analysis took an hour for model preparation, meshing and defining boundary conditions and solving 350 design cases within 15 days to obtain data set for parametric study and ANN modelling. The detail of ANN modelling is given in Chapter 5.1.

Total heat transfer (Q_T) on the inner surface of the tube, the maximum temperature on the fins (T_{max}), the pressure drop (ΔP) between the inlet and outlet of internal volume and the total heat transfer ($\bar{Q}_T$) per unit volume of the heat exchanger are selected and calculated as numerical results. These are also used as output parameters for parametric study and ANN modelling.

3.4.1 The Results and Discussion of the Investigation of the Impact of Design Parameters of the Condensing Boiler's Heat Exchanger on Boiler Performance

Three hundred fifty design points obtained by numerical analyses are used for parametric study. This parametric study aims to investigate the effects of design parameters on the output parameters and find the relationships between them. In the end, the optimal design parameters are found in this study.

The maximum temperature is the most important output parameter regarding the robustness of the aluminium heat exchanger inside the combustion regions. When the heating and cooling cycle of the heat engine is, thermal stress affects the lifetime of the fins on the heat exchanger. If the maximum temperature of the melting point exceeds the aluminium fin tips, the permanent deformation of the heat exchanger becomes unavoidable. Therefore, the maximum temperature on the fin tips is desired below 200 °C. These are the key criteria to start evaluating the results of the calculated 350 design cases. All design cases have the maximum temperature on fins below the key temperature criteria.

After selecting the robustness criteria of the heat exchanger, designers and researchers can evaluate other criteria on heat exchangers' performance like heat

transfer, less material usage and pressure drop. If they need the maximum heat transfer from the heat exchanger to the water domain, they should use the fin thickness of 2.5 mm (according to Table 3.16). Besides the heat transfer criteria, pressure drop or material weight could be considered additional criteria. Table 3.15 can guide them to the starting point to evaluate which fin thickness could be used.

Table 3.16 Sort of design cases in terms of the fin thickness and their maximum and minimum values of output parameters

T_f (mm)	T_{max} [°C]		Q_T [W]		$\bar{Q}_T$ [W/mm^3]		ΔP [Pa]	
	Min.	Max.	Min.	Max.	Min.	Max.	Min.	Max.
0.5	73.2	161.2	19.9	95.6	24.9	40.9	0.50	5.24
1.0	72.5	137.0	24.4	100.7	22.1	26.3	0.55	6.05
1.5	72.3	123.4	29.5	108.4	17.5	24.3	0.62	6.76
2.0	72.2	117.7	34.1	115.8	15.0	22.8	0.68	7.12
2.5	72.0	114.0	38.8	124.0	13.4	21.8	0.75	7.45

The next evaluation is determining the optimum design cases for each output parameter's target value. Table 3.17 summarises the optimum design cases and their output values regarding selected target criteria.

Table 3.17 Optimized design cases in terms of their target criteria

Optimized Parameter	Target	Inputs			Outputs			
		h_f [mm]	t_f [mm]	s [mm]	Q_T [W]	T_{max} [°C]	$\bar{Q}_T$ [W/mm^3]	ΔP [Pa]
Q_T	Maximise	10	2.5	4.0	124.0	96.6	14.1	0.75
$\bar{Q}_T$	Maximise	10	0.5	1	75.1	161.2	40.9	1.04
ΔP	Minimise	10	0.5	4.0	95.6	121.5	32.66	0.50

The heat transfer from the heat exchanger to the water domain maximises with a 10 mm – 2.5 mm – 4.0 mm (h_f - t_f - s) design case. Although the heat transfer maximises

for this case, the total heat transfer ($\bar{Q}T$) per unit volume of the heat exchanger is 14.1 W/mm^3. This value is approximately 34.5 % of the maximised value of $\bar{Q}_T$. The consumption of material is another essential criterion when the design phase of the heat exchanger is ongoing. It is related directly to the cost of the heat exchanger. Therefore, $\bar{Q}_T$ shows a good performance indicator for selecting the optimum total heat transfer (Q_T). Maximised $\bar{Q}_T$ is available with a 10 mm – 0.5 mm – 1.0 mm (h_f - t_f - s) design case. However, the total heat transfer decreased to 75.1 W in that case. Using this criterion to optimize the heat exchanger's design is not enough. When the two parameters maximise simultaneously, the convenient heat transfer rate could enable the fit material consumption. The maximum temperature on the fin tips is obtained at the maximised $\bar{Q}_T$ design case. When the $\bar{Q}_T$ increases, the temperature on the fin tip also increases for every design case due to the usage of less material.

The pressure drop is one of the other criteria to determine or select the correct fan type or power for combustion heat engines. This value is demanded to keep a minimum level to use smaller fan types and operating costs. Therefore, the pressure drop (ΔP) between the inlet and outlet of internal volume could be minimised with a 10 mm – 0.5 mm – 4 mm (h_f - t_f - s) design case.

Finally, the optimal design case reaches each output parameter's target status simultaneously. Table 3.18 shows the optimum design case and its output values.

Table 3.18 Optimum design case (Q_T, $\bar{Q}_T$ max.; ΔP min.)

h_f [mm]	**t_f [mm]**	**s [mm]**	**Q_T [W]**	**T_{max} [°C]**	**$\bar{Q}_T$ [W/mm^3]**	**ΔP [Pa]**
10	0.5	3.5	90.0	122.7	32.8	0.52

3.5 The Investigation of Thermal Performance of the Internally Channels Type of the Finned Tube Heat Exchanger Used for Condensing Boiler

The effects of the design parameters of the finned tube-type heat exchanger on thermal performance have been investigated numerically in the previous study. The water domain was not modelled, and the effects of the design changes on the heat transfer of the finned tube-type heat exchanger in the flue gas region were determined. Besides evaluating the heat transfer in the flue gas region according to ERP regulations, it is necessary to examine the heat transfer of the water region inside the heat exchanger to design a new type of heat exchanger that can replace conventional ones used for condensing wall-hung heating appliances. Therefore, the water region design of heat exchangers is also important. In the literature, there are many numerical and experimental studies on the thermal performance of the finned tube with internally channels type heat exchangers (Kim, 2016; Duan, Ling and Peng, 2018; Joo and Kim, 2016; Wang, Lin and Zeng, 2009; Iqbal, Syed and Ishaq, 2015). However, none examine the heat transfer inside the combustion heat engine.

This study creates numerical models of the finned tube with an internally channels type heat exchanger, which can be used for a wall hang condensing heating appliance. The effect of the heat exchanger designs on thermal performance with different numbers of internal channels has been investigated by using the computational fluid dynamics and heat transfer (CFDHT) method. The total amount of heat transferred to the water (W), the total amount of heat per the heat exchanger's volume (W/dm^3), the total internal surface area (mm^2) from where heat is transferred to water and the ratio of the surface area of the heat transfer are selected as performance parameters. After the numerical simulations, the eight channels model was manufactured and compared to the real results with the base single-channel model. These real results are experimentally obtained. The detail of the experimental setup is represented in Chapter 4.2.

The heat engine (combustion system) is the main module of WHBc, which produces heat from natural gas or liquid gas and transfers it to the water domain. The heat engine has two different regions, shown in Figure 3.31. The combustion chamber is indicated with a red dot rectangular area. It includes a burner, ignition electrodes, heat exchanger

and outlet of water parts. Gas and air are mixed at venture with a determined ratio. This ratio is adjusted by the fan and gas valve. The mixture is directly led to the burner. The burner's task is to enable combustion via ignition electrodes. Spark is produced by an ignition electrode from electricity. After the sparking, the combustion reaction starts, and the flue gas formation occurs in that region. Radiation, convection, and conduction transfer heat to water and ambient. In the combustion chamber, a large amount of thermal energy diffuses with the heat transfer by radiation.

The condensing region is indicated with a blue dot rectangular area. It includes baffles, a heat exchanger, condensate drains and an inlet of water parts. The flue gas is directed to the exhaust pipe by baffles and heat exchanger. The flue gas has latent heat coming from the hot water vapour. The water vapour must condense to gain more energy. The condensing region cools the steam down efficiently through a specially designed heat exchanger. The energy produced from this process is utilised to preheat the cold heating water, which is a great way to conserve energy. Once the water is heated to the required temperature, it is directed to the combustion chamber, which undergoes further heating to reach the desired temperature.

Generally, the same heat exchanger type is used for both heat transfer regions due to the cost and manufacturing process. Conventional finned tube heat exchangers have one internal channel through the water domain. Inside the condensing region, the heat exchanger's external heat transfer surface area is important since a huge amount of total heat is transferred by convection. On the other hand, the heat exchanger's internal heat transfer surface area is also essential to transfer the heat to the water domain. It is ignored for conventional finned tube heat exchangers of condensing wall hang boilers. With this study, different numbers of internal channels for finned tube heat exchangers are simulated via the numerical method in order to determine the effects on the total heat transfer at the water domain.

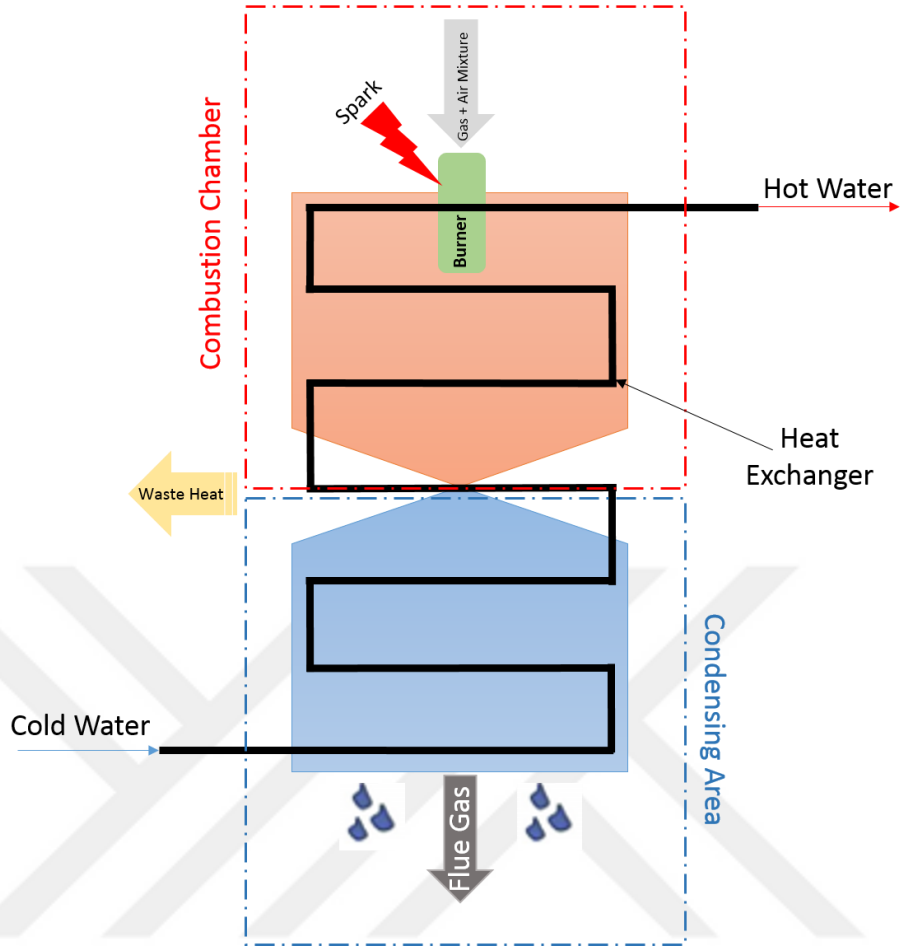


Figure 3.31 Schematic representation of the heat transfer regions of the heat engine unit of a condensing wall hang boiler

As mentioned, the finned tube heat exchanger was used as the base model for numerical simulations with a single internal channel. Four and eight channels were selected for the new development type. Three-dimensional numerical models with two fins base bodies with one, four and eight internal channels respectively are shown in Figure 3.32. The fins are circular, and the fin height is 4 mm for all models. The fin thickness is 0.5 mm, and the gap between the fins is modelled as 1 mm. The inner diameter of the finned pipes is 30 mm, and the wall thickness is 2 mm.

The solid volume of the finned tube with internally channels type heat exchangers and the volume of water inside them are modelled as three-dimensional.



Figure 3.32 Three-dimensional numerical models with different internal channel numbers

After the models are created, the meshing process is the next step for the numerical analysis. Optimized meshing structures for numerical models have been created using different meshing techniques. The number of mesh elements of numerical models varies between 195.52 and 864.061, shown in Figure 3.33.



Figure 3.33 Mesh structure of numerical models

During the numerical solutions, 167 W/mK heat transfer coefficient (the 6000 series aluminium material at room temperature) and 0.42 emissivity coefficient values are entered for the solid volume model of the finned tube with internally channels type heat exchangers. In addition, the thermophysical properties of water at 30 ℃ are used for analysis (Incropera and Dewitt, 2000).

The convection heat transfer mechanism plays a crucial role in the condensing region of the heat engine, highlighted with blue dots area in Figure 3.34. Therefore,

internal channel design can affect the heat transfer to the water domain at that region. The boundary conditions of the condensing region are selected for numerical simulations.

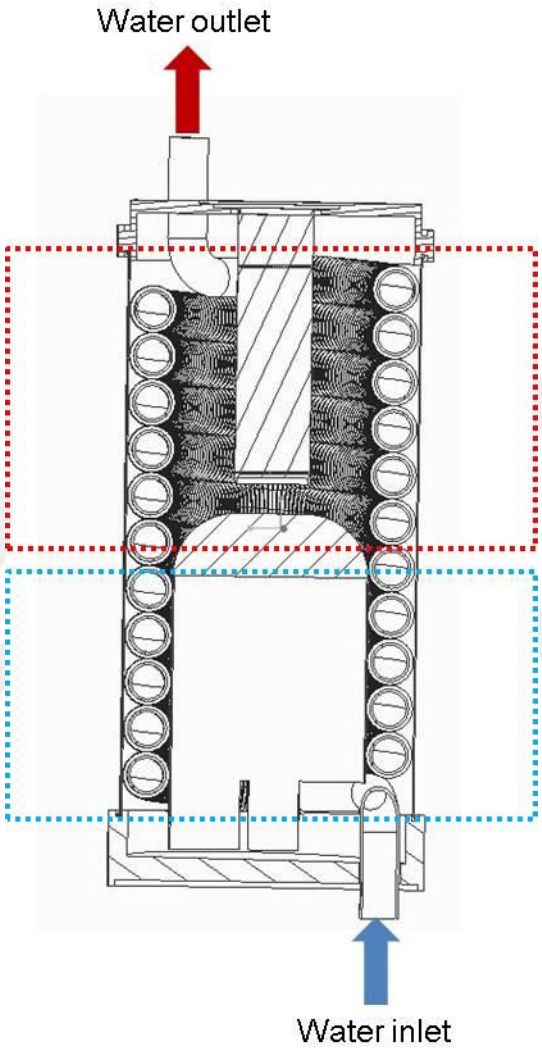


Figure 3.34 General cross-sectional view of heat exchanger structure with the single internal channel

The boundary conditions given in Figure 3.35 are defined for all numerical models. 80 W/m^{2}K convection coefficient at 150 °C is used on the finned tube surfaces, and a 10 lt/min flow rate at 30 °C is defined for the water inlet. The steady state, radiation effects, natural convection by gravity, forced convection by pump and turbulent flow type conditions are considered when solving numerical models.

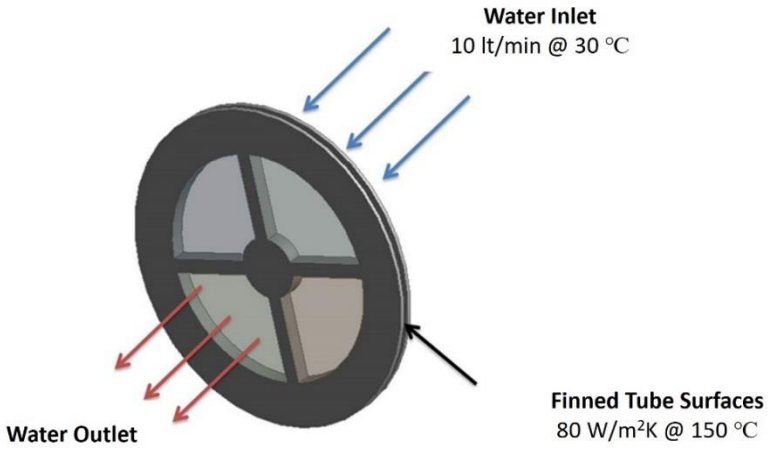


Figure 3.35 Schematic representation of boundary conditions for numerical models

3.5.1 The Results and Discussion of the Investigation of Thermal Performance of the Internally Channels Type of the Finned Tube Heat Exchanger Used for Condensing Boiler

As a result of the evaluation of the numerical analysis, the effects of the heat exchanger design on thermal performance with different numbers of internal channels are investigated. The total amount of heat transferred to the water (W), the total amount of heat per the heat exchanger's volume (W/dm^3), the total internal surface area (mm^2) from where heat is transferred to water and the ratio of the surface area of the heat transfer are selected as a thermal performance indicator.

Table 3.19 is given the results of the analysis for the numerical models. Although the total amount of heat transferred to the water has been determined as 8.11 W for the numerical model with eight channels, 7.48 W is found for the numerical model with four channels and 1.68 W for a single channel.

Table 3.19 The results of the analysis for the numerical models

	Single Channel	**Four Channels**	**Eight Channels**
The total amount of heat transferred to the water (W)	1.68	7.48	8.1
The total amount of heat per the heat exchanger's volume (W/dm^3)	1872.30	6475.16	6096.2
The total external surface area (mm^2) from where heat is transferred to the water	1193.81	1193.81	1193.81
The total internal surface area (mm^2) from where heat is transferred to the water	188.50	384.08	526.64
The ratio of the surface area of the heat transfer	6.33	3.11	2.27

Although the total amount of heat transferred to water is the highest in the eight channels model, the largest total amount of heat per the heat exchanger's volume (6475.16 W / dm3) is found in the four channels model. Even though the total heat in the four-channel model decreased by 7.7%, it was obtained using 6.21% less aluminium material. By optimising the number of channels according to the required heat amount, it can be seen that less material usage can be determined via numerical analysis.

After numerical analyses, a new finned tube heat exchanger prototype was manufactured with eight channels. A general view of the new heat exchanger is shown in Figure 3.36. The base heat engine model has a finned tube heat exchanger with a single internal channel. External dimensions of the base heat engine were kept the same for the new heat exchanger prototype with eight channels. The base heat engine reached the maximum 51.8 kW output power with 91.3% seasonal efficiency. With a newly developed heat exchanger, 84.6 kW output power was achieved. All performance tests were performed according to EN 15502 standard. As a result, 63% more output power and 92.4% seasonal efficiency were gained with the same heat engine volume used with numerical simulation.

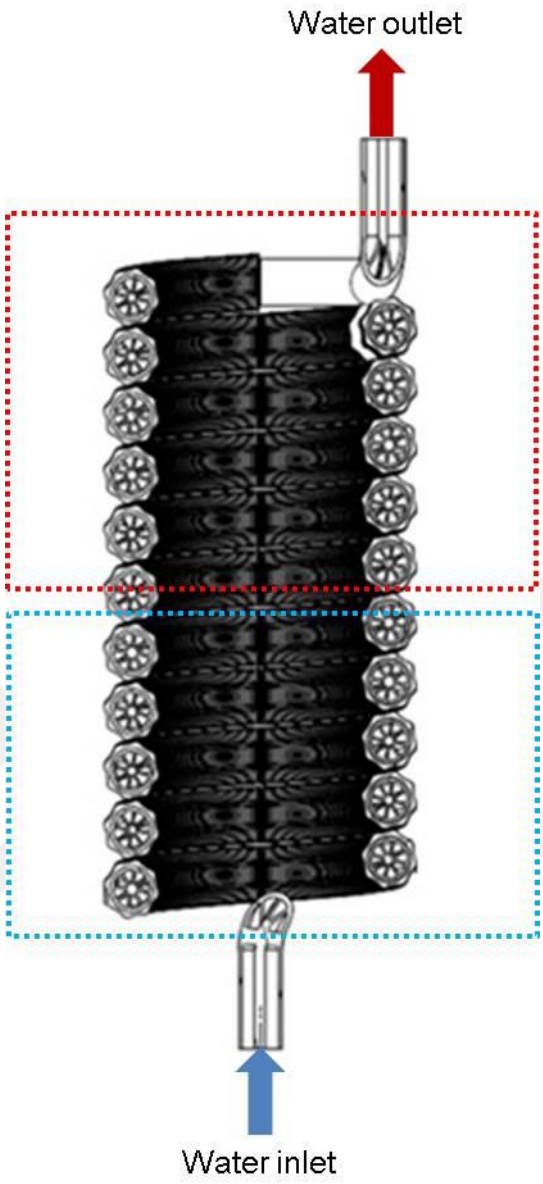


Figure 3.36 General view of new finned tube heat exchanger with eight channels

For all cases modelled in the analyses, the total external surface area from where heat is transferred to water is the same and 1193.81 mm^2. The effect of the internal transfer surface area changes, i.e. the number of channels, is determined by keeping the external surface area constant. The ratio of the surface area of the heat transfer for the single-channel model is 6.33, whereas it decreases to 2.27 in the eight channels model. As seen in numerical analysis, the closer the ratio is to 1, the greater the total heat transfer is achieved. In order to increase the thermal performance in heat exchanger designs that can be used in heat engine units, it is determined with this

numerical study that we should not only focus on the flow of the flue gas side. The closer the heat transfer surface area is to 1, the higher the amount of material to be used in the heat exchanger. With this numerical study, it has been shown that the total amount of heat per the heat exchanger's volume (W / dm^3) can be determined and used as the output of the design parameter.

Finally, it is necessary to perform optimization studies not only in the external surface transfer area but also in the internal transfer surface area. Numerical simulations can help us optimize the heat exchanger's transfer surface areas and decrease the making of prototype numbers and their manufacturing time. According to the comparison of the numerical results, there is a huge deviation between the single and eight internal channels in terms of total heat transfer. However, experimental results are shown us that 63% more output power can be gained with the same heat engine volume in real life. This variation comes from the boundary conditions of numerical models. Boundary conditions (temperature of water, temperature of flue gas, convection coefficient, and so on) change through the heat exchanger length in reality. Therefore, characteristic heat transfer regions should be modelled separately and defined as their boundary conditions precisely.

CHAPTER FOUR
EXPERIMENTAL INVESTIGATION OF CONDENSING BOILER

Computational fluid dynamics and heat transfer (CFDHT) has given useable methods to engineers and researchers to study fluid flow and heat transfer phenomena for condensing boilers. It offers a virtual platform to simulate complex fluid behaviours and heat transfer in various applications. However, while CFD simulations provide powerful insights, the relation between experimental studies and CFD simulations remains indispensable for accurate and reliable results. Real-world measurements are essential in experimental studies to validate CFD models. This crucial process gives confidence in simulation results and indicates model deficiencies, boundary condition errors, and assumptions that may cause discrepancies. It is important to emphasise that experimental data serves for the accuracy of CFD simulations. CFD simulations often include making simplifications and assumptions due to computational limitations and numerical model complexity. Experimental studies can help us to identify cases where these simplifications and assumptions could not be real. They guide the enhancement of simulation modelling, ensuring that the simulations represent real-world conditions as closely as possible.

The relation between experimental studies and CFD simulations extends to new product development or optimising actual design parameters to reach performance targets. Experimental validation of CFD predictions is crucial in industries like heating and ventilation, where the emission and efficiency of appliances are important according to the regulations and standards.

One of the key advantages of experimental studies is to determine cases that might be challenging to model accurately in simulations. Moreover, experimental studies provide data on boundary conditions critical inputs for CFD simulations. Incorrect boundary conditions can lead to significant variances between simulation and reality. By using experimental data to define these conditions, simulations' results become more realistic and reliable. It ensures that the simulated performance of a new design aligns with physical reality, reducing the cost of design and time. While CFD simulations provide a powerful and efficient tool for studying fluid dynamics, experimental studies remain a cornerstone of accurate and reliable results.

In the following section of this chapter, the experimental investigation of the flow characteristics of the flue gas movement inside the combustion unit modelling with the air domain and flue gas domain, the experimental investigation of thermal performance of the internally channels type of the finned tube heat exchanger used for condensing boiler, 23 kW condensing boiler experiments and 153 kW condensing boiler experiments are discussed.

4.1 The Experimental Investigation of the Flow Characteristics of the Flue Gas Movement Inside the Combustion Unit Modelling with the Air Domain and Flue Gas Domain

The numerical simulations were performed to clarify the modelling of the fluid domain as air or flue gas for the combustion unit of a condensing boiler with a heat recovery device given in Chapter 3.3. Two basic control volumes were modelled and prototyped for the internal flue gas to decrease the effect of model complexity on the pressure drop and flow characteristic of flue gas movement in the combustion unit. The detail of control volumes was represented in Figure 3.19 and Figure 3.23. The experimental setups are created with these control volumes to determine the boundary conditions of simulations and validate the numerical results and models.

Figure 4.1 shows the schematic view of the experimental setup for the first basic heat recovery model's control volume. The first basic heat recovery model's control volume has three stainless steel plates with several holes. These plates were hermetically assembled at certain distances. The holes on the plates are drilled, staggered and placed in the positions in Figure 3.19. The first experimental setup is prototyped to determine the boundary conditions of the air domain for the numerical model shown in Figure 4.1.

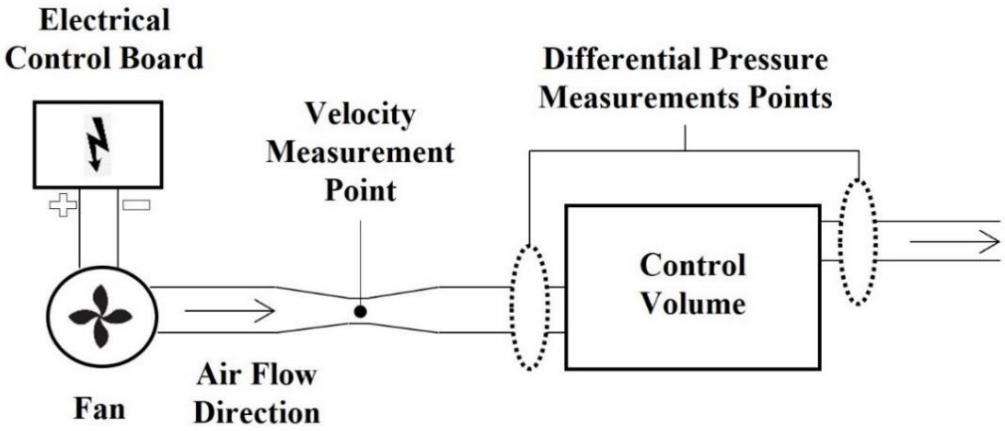


Figure 4.1 The schematic view of the experimental setup for the first basic heat recovery model's control volume

Two apparatus are made to measure the velocity and pressure drop of air. The fan is assembled into the inlet apparatus, which is used for condensing the boiler and moving the air. The electrical control board has adjusted the voltage of the fan. When the fan's voltage increases, the fan speed increases, and the air velocity increases. The diameter of the inlet apparatus narrows at the middle region to measure the velocity of air sensitively with a digital vane flow velocity probe and its datalogger. This probe has a 0.6 to 50 m/s measurement range, and its accuracy is 0.2 m/s. The inlet and outlet apparatus have holes to measure the differential pressure of air. The micromanometer measurement device measures the control volume's pressure drop. This micromanometer has a 0 to 999 Pa measurement range, and accuracy is ± 0.05 Pa. The first experimental setup is shown in Figure 4.2.

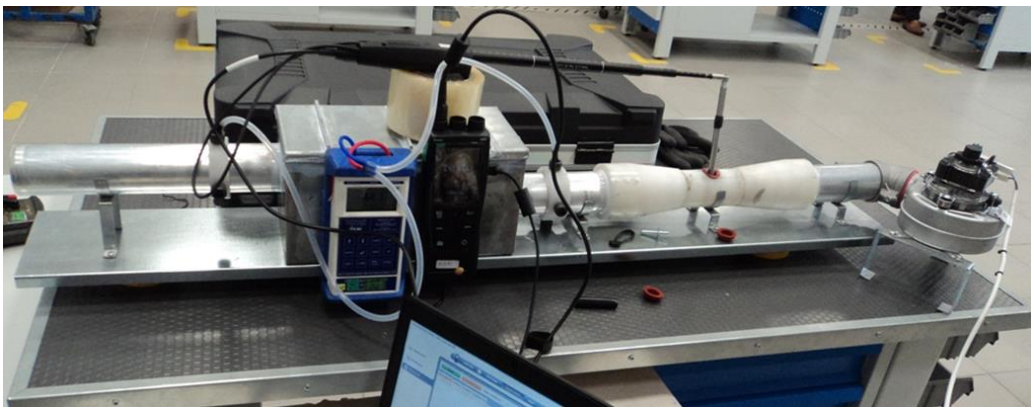


Figure 4.2 The experimental setup for the first basic heat recovery model's control volume

Two different experiments are performed with this experimental setup. The first one is to measure the velocity of the air and the pressure drops of the first basic control volume at various fan voltages. The average air velocity and pressure drop are measured for twenty fan voltage values listed in Table 4.1.

Table 4.1 The experimental results of the first basic control volume at various fan voltages

Measurement Point	**Fan Voltage [Volt]**	**Average Air Temperature [°C]**	**Average Air Velocity [m/s]**	**Average Pressure Drop [ΔP]**
1	230	23.4	21.93	45.5
2	220	23.5	21.88	45.2
3	210	23.5	21.79	44.8
4	200	23.4	21.75	44.2
5	190	23.5	21.59	43.8
6	180	23.4	21.39	43.4
7	170	23.4	21.09	42.5
8	160	23.4	20.56	41.7
9	150	23.4	20.23	39.5
10	140	23.5	19.31	37.8
11	130	23.5	17.71	29.0
12	120	23.5	14.34	18.0
13	110	23.3	9.36	9.6
14	100	23.3	8.31	6.0
15	90	23.3	7.78	5.2
16	80	23.3	6.85	4.1
17	70	23.3	5.76	3.5
18	60	23.3	4.30	2.5
19	50	23.3	2.45	0.8
20	40	23.3	1.30	0.2

Three measurements are recorded every ten seconds for each measurement point. So, the average air temperature, air velocity, and pressure drop of the control volume are determined. The average air temperature and velocity were used for the boundary conditions of numerical modelling with the air domain. The average pressure drop results were compared with numerical results, and the numerical model of the first basic heat recovery device was validated. Numerical results are given in Chapter 3.3

The second experiment with this experimental setup is to determine the boundary conditions of the flue gas domain for the numerical model. This experimental setup is integrated into the outlet of the wall-hang condensing boiler to measure the flue gas temperature, the flue gas velocity and the pressure drops of the control volume. Figure

4.3 shows the schematic view of the second experimental setup for the first basic heat recovery model's control volume with the flue gas domain.

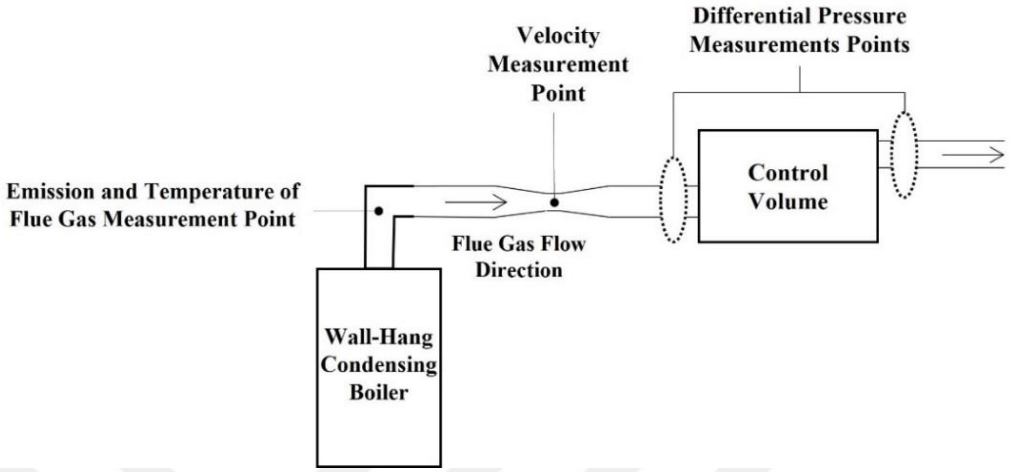


Figure 4.3 The schematic view of the second experimental setup for the first basic heat recovery model's control volume with flue gas

The second experimental setup is shown in Figure 4.4. The same measurement devices are used to measure flue gas's velocity and pressure drops. The wall-hang condensing boiler is installed on a fully equipped test rig. Pure methane (G20) is used for operating the heating appliance. All measurements are recorded simultaneously when the appliance operates in a steady state condition. The emission and temperature of the flue gas are measured with an exhaust gas analyser. This gas analyser has 0 to 40% CO_2 and 0 – 400 ℃ measurement ranges. Its accuracy is ±0.1% for CO_2 and ±0.1℃ for flue gas temperature.

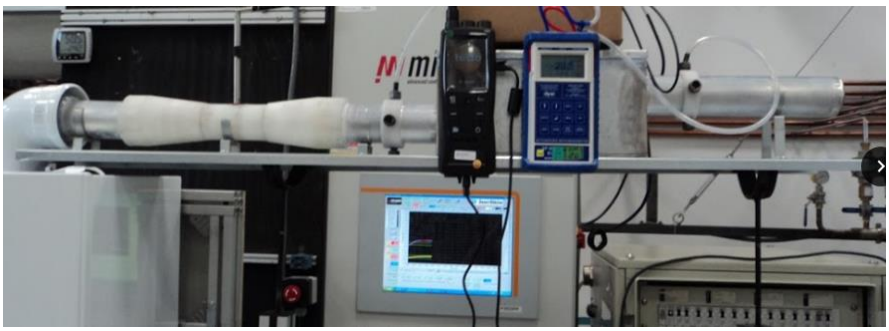


Figure 4.4 The second experimental setup for the first basic heat recovery model's control volume with flue gas

When the wall-hang boiler is operating in a steady state condition, CO_2 emission and the flue gas temperature are measured. The CO_2 emission value of flue gas is obtained as 10.9%, which is kept the same for each measurement point listed in Table 4.2. The average flue gas velocity, temperature, and the average pressure drop of the control volume are recorded for ten measurement points and shown in Table 4.2. All measurement data are taken every ten seconds.

Table 4.2 The second experimental results of the first basic control volume with flue gas

Measurement Point	**Average Flue Gas Temperature [°C]**	**Average Flue Gas Velocity [m/s]**	**Average Pressure Drop [ΔP]**
1	47.8	8.98	28.5
2	47.9	8.96	28.4
3	47.0	8.98	28.5
4	48.9	8.97	28.4
5	47.0	8.97	28.2
6	47.9	9.06	28.1
7	47.8	9.03	28.7
8	49.2	9.12	28.8
9	47.3	9.25	28.6
10	47.4	9.28	28.6
Average	**47.82**	**9.06**	**28.48**

According to Table 4.2, the average flue gas velocity is 9.06 m/s, the average flue gas temperature is 47.82 C°, and the pressure control pressure drop (ΔP) is 28.48 Pa. The average flue temperature and velocity were used for the boundary conditions of numerical modelling with the flue gas domain. The average pressure drop results were compared with the numerical results given in Chapter 3.3.1.

Experimental studies show that when the fluid is modelled as air and flue gas for the close volumetric flow rates, there are huge differences in pressure drops. In the studies carried out with air and the flue gas in the control volume made of perforated stainless plates, different pressure drops close to 3 times were obtained for the same volumetric flow conditions given in Table 4.3.

Table 4.3 The comparison of the experimental results for the air and flue gas inside the first basic control volume

Domain	Average velocity (m/s)	Average Pressure Drop [ΔP]
Air	9.36	9.60
Flue Gas	9.06	28.48
Percentage Difference		196.67%

The third experimental setup is made like in Figure 4.4. The control volume is only different from the first and second experimental setups. The second basic heat recovery model's control volume has three heat exchangers manufactured with an aluminium casting technique. These heat exchangers were hermetically assembled at certain distances in Figure 3.23.

The third experiment with this experimental setup is to determine the boundary conditions of the flue gas domain for the numerical model of the second basic heat recovery. This experimental setup is integrated into the outlet of the wall-hang condensing boiler to measure the flue gas temperature, the flue gas velocity and the pressure drops of the control volume. Figure 4.3 shows the schematic view of the second experimental setup for the second basic heat recovery model's control volume with the flue gas domain.

The third experimental setup is shown in Figure 4.5. The same measurement devices are used to measure flue gas's velocity and pressure drops. The wall-hang condensing boiler is installed on a fully equipped test rig. Pure methane (G20) is used for operating the heating appliance. All measurements are recorded simultaneously when the appliance operates in a steady state condition. The emission and temperature of the flue gas are measured with an exhaust gas analyser. This gas analyser has 0 to 40% CO_2 and 0 – 400 °C measurement ranges. Its accuracy is ±0.1% for CO_2 and ±0.1°C for flue gas temperature.

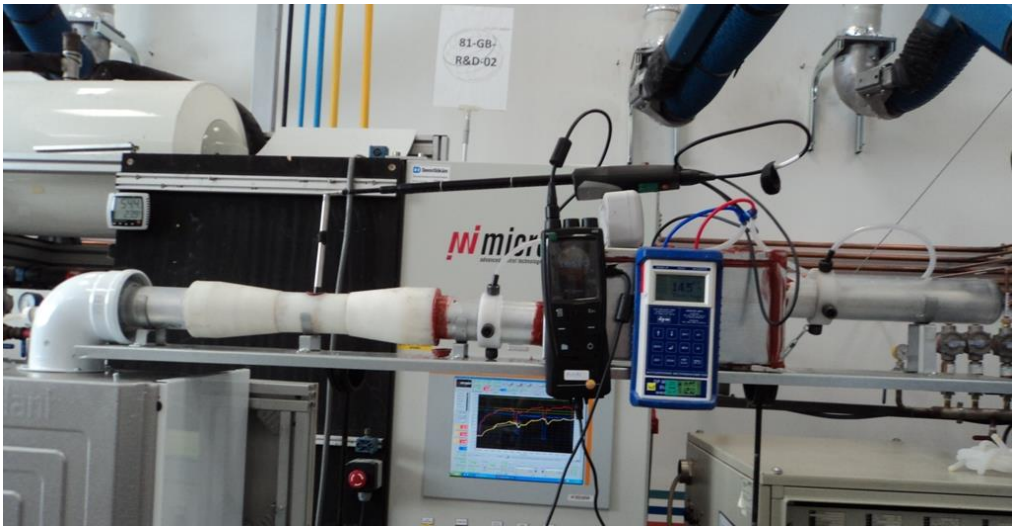


Figure 4.5 The third experimental setup for the second heat recovery model's control volume with flue gas

When the wall-hang boiler is operating in a steady state condition, CO_2 emission and the flue gas temperature are measured. The CO_2 emission value of flue gas is adjusted as 10.9% to be compared with the experiment results of the first heat recovery model with flue gas, and this value is kept the same value for each measurement point listed in Table 4.4. The average flue gas velocity, temperature, and the average pressure drop of the control volume are recorded for ten measurement points and shown in Table 4.4. All measurement data are taken every ten seconds.

Table 4.4 The third experimental results of the second basic control volume with flue gas

Measurement Point	**Average Flue Gas Temperature [°C]**	**Average Flue Gas Velocity [m/s]**	**Average Pressure Drop [ΔP]**
1	47.7	9.33	11.2
2	47.7	9.27	11.1
3	47.6	9.21	11.3
4	48.2	9.58	11.2
5	48.5	9.57	10.9
6	48.7	9.56	11.0
7	48.4	9.43	11.0
8	48.8	9.46	11.3
9	49.1	9.48	11.3
10	49.4	9.49	11.0
Average	**48.41**	**9.44**	**11.13**

According to Table 4.4, the average flue gas velocity is 9.44 m/s, the average flue gas temperature is 48.41 C°, and the pressure control pressure drop (ΔP) is 11.13 Pa.

The average flue temperature and velocity were used for the boundary conditions of numerical modelling with the flue gas domain. The average pressure drop results were compared with the numerical results given in Chapter 3.3.2.

In both studies, the combustion reaction (10.9% CO_2 emission) in the wall-hang heating appliance is the same. Although the volumetric flow rates of the flue gas are close to each other, there are close to 2.5 times differences between the pressure drops given in Table 4.5.

Table 4.5 The comparison of the experimental results for the air and flue gas inside the first basic control volume

Control Volume	**Average velocity (m/s)**	**Average Pressure Drop [ΔP]**
Aluminium Heat Exchanger	9.40	11.10
Stainless Steel Plate	9.06	28.48
Percentage Difference		156.58%

As a result of this study, the average velocity, temperature, and pressure drops for both domains due to design differences can be experimentally tested in detail. In this way, it is possible to determine the boundary conditions for numerical models and validate them with experimental results.

4.2 The Experimental Investigation of Thermal Performance of the Internally Channels Type of the Finned Tube Heat Exchanger Used for Condensing Boiler

The effect of the heat exchanger designs on thermal performance with different numbers of internal channels was investigated by using the computational fluid dynamics and heat transfer (CFDHT) method in Chapter 3.5. The eight internal channels model was the best design case instead of the single channel design. In this study, two heat engines are designed and prototyped with heat exchangers manufactured with single and eight internal channels. These heat engines have the same outer dimensions. Only heat exchangers are different for both heat engines. After that, two different wall-hang condensing boiler prototypes are made, and their performance test is performed.

Figure 4.6 shows the detail of the heat engine designed with a single internal channel heat exchanger. This heat exchanger is made of 6060 series aluminium and a helical finned tube heat exchanger. The fin height is 4 mm, the fin thickness is 0.5 mm, and the gap between the fins is 1 mm. The inner diameter of the finned tube is 30 mm, and the wall thickness is 2 mm. The burner door and condensing collector are made of 6060 series aluminium. The mineral wool is assembled inside the burner door to isolate the fan and gas valve from the high temperature of the burner side. The outer shield is made of stainless steel, and the sheet of mineral wool, which is 2 mm thick, is assembled between the inner side of the outer shield and heat exchanger. This mineral wool prevents heat loss to the ambient from the heat engine. The baffle is designed and manufactured to divert the flue gas to heat exchangers for maximising heat transfer at the condensing region.

After that, the prototype of the wall-hang condensing boiler is produced to perform the development test with the single internal channel heat exchanger. Figure 4.7 shows the prototype of the wall-hang condensing boiler with the single internal channel heat exchanger.

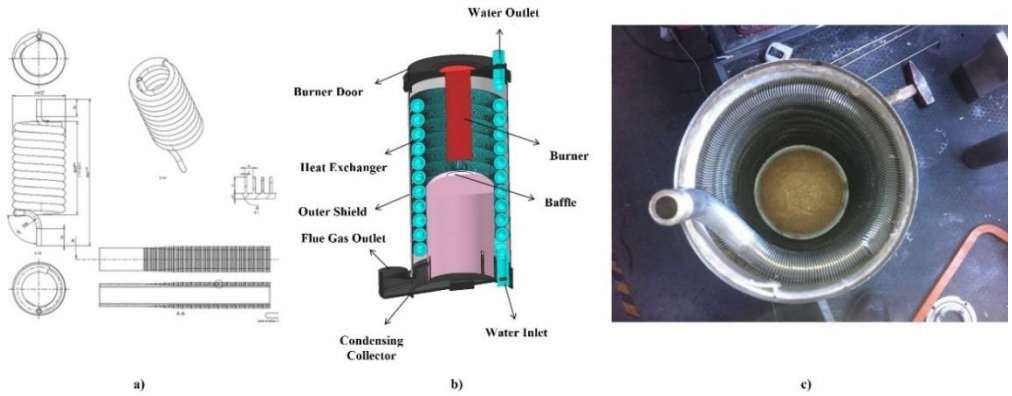


Figure 4.6 The detailed view of the heat engine with single internal channel heat exchanger a) technical view of the single channel heat exchanger b) the cross-section of heat engine design c) the top view of the heat engine prototype with single internal channel heat exchanger



Figure 4.7 The prototype of the wall-hang condensing boiler with the single-channel heat exchanger

The boiler prototype is installed on a fully equipped test rig. The first experimental study is to determine the maximum capacity of the boiler with convenient emission. Pure methane (G20) is used for all tests. The trial-error method adjusts the boiler to reach the maximum inlet load. The 51.8 kW maximum inlet load is achieved at 8.9 % CO_2 value. At that operating condition, CO emission of 104 ppm and NO_x emission of 39 ppm are found. The seasonal efficiency tests are performed and obtained at 91.3%.

Figure 4.8 shows the detail of the heat engine designed with eight internal channel heat exchangers. This heat exchanger is made of 6060 series aluminium and a helical finned tube heat exchanger. The fin height is 4 mm, the fin thickness is 0.5 mm, and the gap between the fins is 1 mm. The inner diameter of the finned tube is 30 mm, and the wall thickness is 2 mm. The burner door and condensing collector are made of 6060 series aluminium. The mineral wool is assembled inside the burner door to isolate the fan and gas valve from the high temperature of the burner side. The outer shield is made of stainless steel, and the sheet of mineral wool, which is 2 mm thick, is assembled between the inner side of the outer shield and heat exchanger. The same baffle is designed and manufactured to divert the flue gas to heat exchangers for

maximising heat transfer at the condensing region. Only the heat exchanger is changed according to the first heat engine prototype.

After that, the prototype of the wall-hang condensing boiler is produced for the development test with the eight internal channels heat exchanger. Figure 4.9 shows the prototype of the wall-hang condensing boiler with the eight internal channels heat exchanger.

The second boiler prototype is installed on a fully equipped test rig. The first experimental study is to determine the maximum capacity of the boiler with convenient emission. Pure methane (G20) is used for all tests. The trial-error method adjusts the boiler to reach the maximum inlet load. The 84.6 kW maximum inlet load is achieved at a 9.06 % CO_2 value. At that operating condition, CO emission of 117 ppm and NO_x emission of 26 ppm are found. The seasonal efficiency tests are performed and obtained at 92.4%.

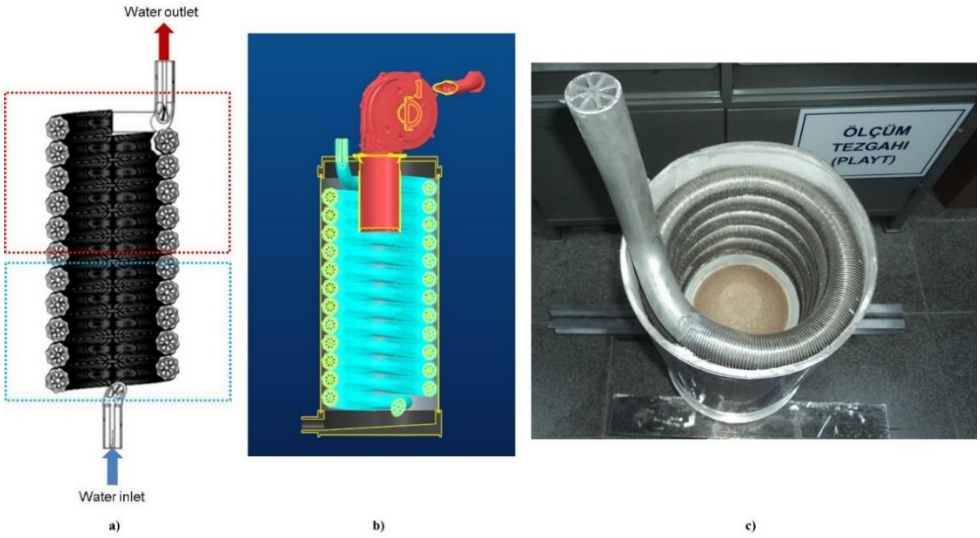


Figure 4.8 The detailed view of the heat engine with eight internal channels heat exchanger a) the cross-section of eight channels heat exchanger b) the cross-section of heat engine design c) the top view of the heat engine prototype with eight internal channels heat exchanger



Figure 4.9 The prototype of the wall-hang condensing boiler with the eight channels heat exchanger

As a result, 63% more output power and 92.4% seasonal efficiency are gained with the same heat engine volume used with eight internal channels heat exchanger.

4.3 The 23 kW Condensing Boiler Experiments

In this study, the whole wall-hang boiler experimentally investigated the output parameters of performance and emissions. This condensing boiler has a premix combustion unit and a stainless-steel heat exchanger. This unit provides the gas/air mixture that adjusts the desired value with the gas/air mixing system (Figure 4.10). It comprises the radial fan, pneumatic gas valve, venture, and stainless-steel multi-hole burner. The fan speed (rpm value) is the main control mechanism to allow gas flow rate into the burner. Additionally, the gas valve has a mechanical adjustment point to regulate the air-gas equivalence ratio (φ).

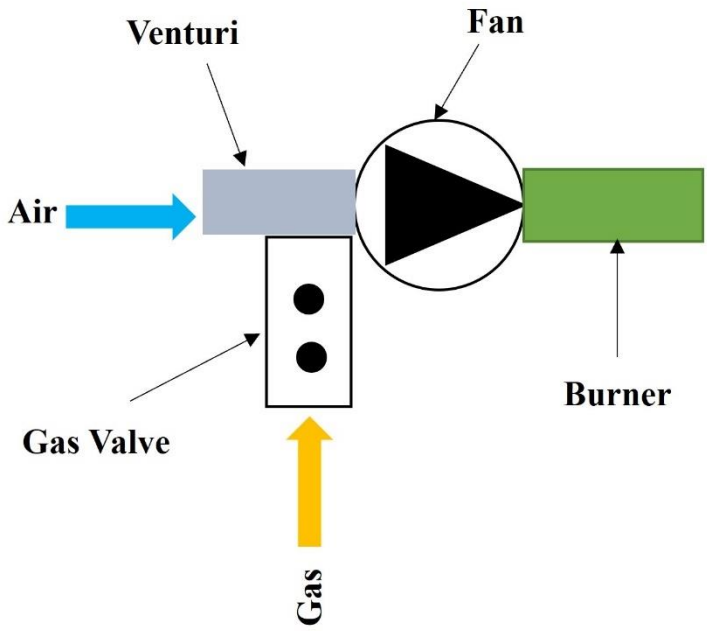


Figure 4.10 The gas/air mixing system of the wall-hang condensing boiler

The fan speed (rpm value) and the air-gas equivalence ratio (φ) are the main parameters to determine the performance of a condensing wall hang boiler. The air-gas equivalence ratio plays a significant role in emissions (CO, NO and NO_2), and the fan speed can adjust most of the input heat load of the boiler. The gas type is also used as another design parameter for this study. The effects of these three parameters on the input heat load and emissions are evaluated and presented. Finally, the optimum working condition is determined to provide lower NO_x emission calculated according to the EN15502 standard.

The schematic view of the experimental setup is shown in Figure 4.11. Experimental tests are performed at a fully equipped and calibrated test rig.

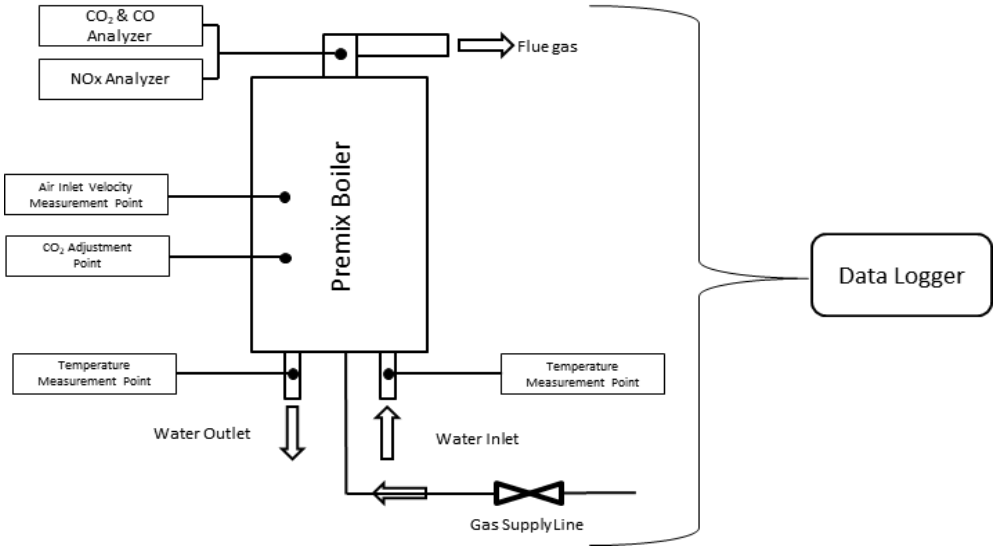


Figure 4.11 Schematic view of experimental setup

The values of input parameters are given in Table 4.6. According to the variation of design parameters, sixty different design points are performed experimentally, and their results are recorded. Twenty design points are measured per one working day at the test laboratory (Figure 4.12).

Table 4.6 The variation of design parameters

Design Parameter	Values
Gas Type	G20 (Pure Methane) - NG Line Gas
Fan Speed (rpm)	1700 – 2400 – 3500 – 4000 - 5500
Air-gas equivalence Ratio (φ)	0.65 - 0.70 - 0.75 - 0.80 - 0.85 - 0.90



Figure 4.12 The experimental setup for the 23 kW condensing boiler

Current condensing boiler technology with pneumatic gas valve are adjusted under two operating conditions. The first is to be adjusted at a nominal input heat load (maximum). This condition is also called a 100% modulation ratio. After the maximum adjustment, the minimum modulation ratio is done at a minimum input load. The minimum modulation ratio changes according to the boiler design and its components. The modulation ratio is calculated as Equation 1. Q_c is the working input load of the boiler when the boiler is operating at any point between minimum and maximum conditions. After these adjustments, boilers operate between the maximum and minimum modulation range.

$$\text{Modulation Ratio} = Q_c/Q_n \times 100\ [\%] \quad (4.1)$$

This investigated condensing boiler was designed and certificated according to the 23 kW nominal input heat load (Q_n) and the 6 kW minimum input heat load (Q_{min}). It can operate between 26% and 100% modulation range. The first design point refers to the initial condition of a boiler operated with natural gas. With a 5500 rpm fan speed and 0.75 air-gas equivalence ratio (φ), a 23.39 kW input load is measured. With 1700 rpm fan speed and 0.75 air-gas equivalence ratio (φ), a 6.36 kW input load is measured. After that, the condensing boiler is operated with G20 gas, the same fan speed, and air-gas equivalence ratio (φ). 24.03 kW maximum input heat load and 6.41 kW minimum input heat load are measured to determine the initial condition of the boiler operated with G20 gas.

Table 4.6 shows sixty design cases for five different fan speeds, six different air-gas equivalence ratios (φ) and two different gas types. The experimental results are given in Table 4.7. The table gives the input heat load (Q_c), modulation ratio (%), CO, NO and NO_2 emissions (ppm) for each design point. The bold highlighted results show the initial condition of the condensing boiler. This experimental data set is used for the artificial neural network study in Chapter 5.2.

Table 4.7. Experimental results of all design points

Exp. No.	Gas Type	φ	Fan Speed [rpm]	CO [ppm]	NO [ppm]	NO_2 [ppm]	Modulation [%]	Q_c [kW]
1	NG	0.65	5500	7.25	0.63	3.47	93	21.49
2	NG	0.70	5500	22.49	2.93	4.72	100	22.98
3	**NG**	**0.75**	**5500**	**5642**	**8.73**	**7.54**	**102**	**23.39**
4	NG	0.80	5500	12696	18.01	9.97	113	25.95
5	NG	0.85	5500	25293	33.75	16.71	118	27.25
6	NG	0.90	5500	650.62	66.49	26.08	126	28.96
7	G20	0.65	5500	5.79	1.08	4.48	94	21.54
8	G20	0.70	5500	20.81	3.46	5.77	100	23.06
9	**G20**	**0.75**	**5500**	**74.29**	**10.84**	**8.91**	**104**	**24.03**
10	G20	0.80	5500	127.17	18.62	9.53	113	26.05
11	G20	0.85	5500	280.73	38.24	17.64	119	27.45
12	G20	0.90	5500	678.65	70.31	25.81	126	29.05
. . .	. . .	. . .	. . .	. . .	. . .	. . .	. . .	. . .
49	NG	0.65	1700	0.00	2.60	2.59	26	5.89
50	NG	0.70	1700	0.00	5.46	3.91	27	6.25
51	**NG**	**0.75**	**1700**	**0.00**	**6.87**	**4.74**	**28**	**6.36**
52	NG	0.80	1700	0.00	18.92	7.76	30	6.93
53	NG	0.85	1700	0.75	30.01	10.97	31	7.20
54	NG	0.90	1700	17.14	47.45	15.27	33	7.55
55	G20	0.65	1700	0.00	2.52	2.93	26	5.87
56	G20	0.70	1700	0.00	5.27	3.74	27	6.24
57	**G20**	**0.75**	**1700**	**0.00**	**7.54**	**5.14**	**28**	**6.41**
58	G20	0.80	1700	0.00	17.32	7.53	30	6.89
59	G20	0.85	1700	0.27	29.11	11.12	31	7.23
60	G20	0.90	1700	16.39	47.55	14.52	33	7.68

4.3.1 The Effects of the Air-Gas Equivalence Ratio on the Boiler Performance

The air-gas equivalence ratio (φ) is adjusted from 0.65 to 0.90 for each fan speed and gas type. Figure 4.13 and Figure 4.14 show the variation graphs of input heat load (Q_c) when the air-gas equivalence ratio (φ) is changed. According to Figures 4.13 and 4.14, the same variation trends are seen for input heat loads operated by the natural gas and G20. Input loads at G20 are more than the natural gas state. When the air-gas equivalence ratio (φ) increases, input heat loads increase for all fan speeds. However, the increased rate of the input heat load has a high slope when the fan speed drives up above 3000 rpm. If the input heat load needs to be increased, the air-gas equivalence ratio (φ) can be adjusted higher.

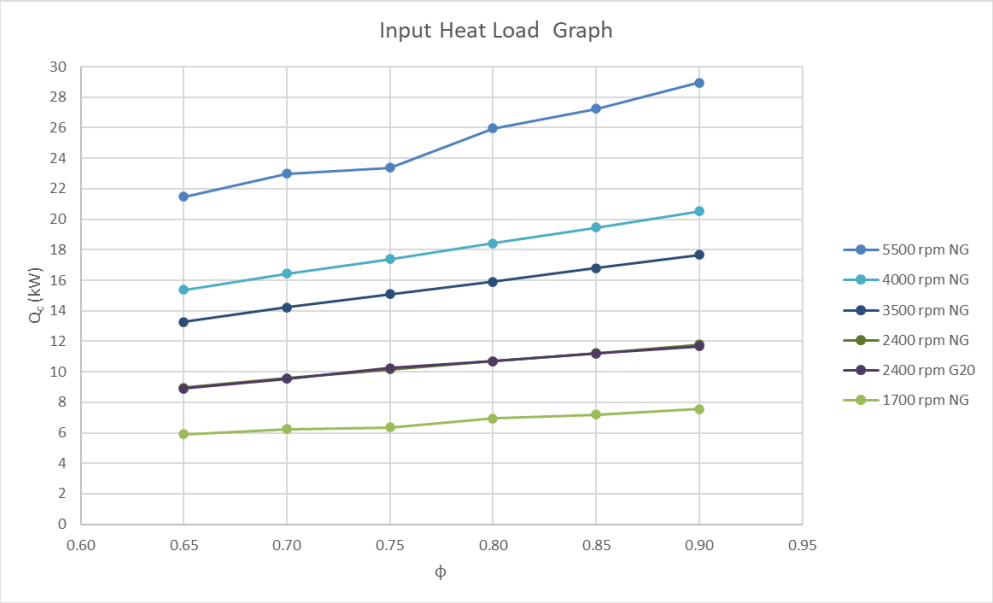


Figure 4.13 The variation graph of input heat load when changing the air-gas equivalence ratio for natural gas

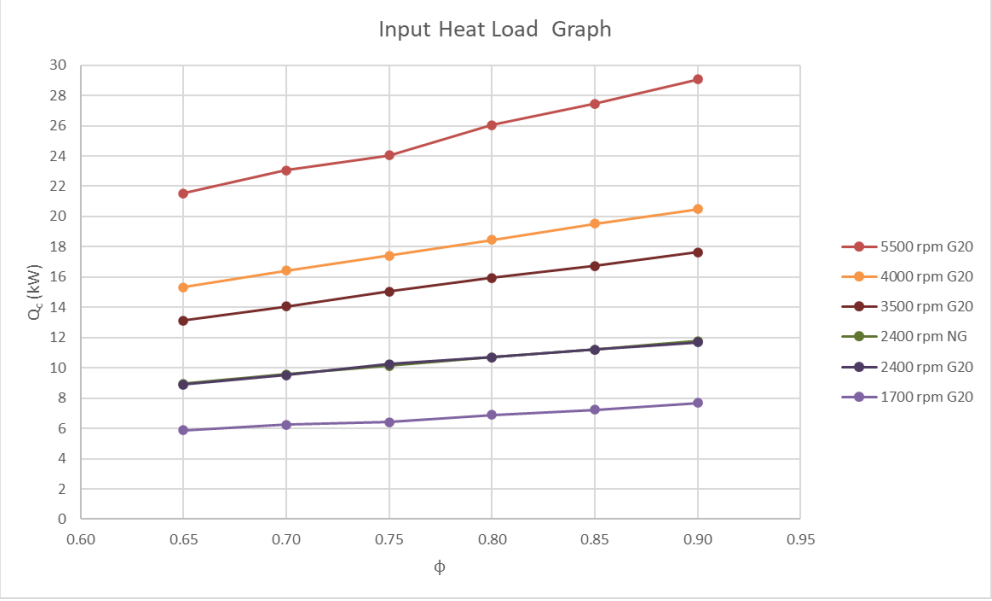


Figure 4.14 The variation graph of input heat load when changing the air-gas equivalence ratio for G20 gas

The air-gas equivalence ratio (φ) is adjusted from 0.65 to 0.90 for each fan speed and gas type. Figure 4.15 and Figure 4.16 show the variation graphs of CO emission when the air-gas equivalence ratio (φ) is changed. Figures 4.15 and 4.16 show the same variation trends for CO emissions operated by the natural gas and G20. CO emissions

increase for all fan speeds when the air-gas equivalence ratio increases. However, the increase rate of the CO emission has a high slope when the air-gas equivalence ratio is adjusted as 0.80 and above. For high fan speeds, especially 5500 rpm, CO emissions increase dramatically. If the CO emissions need to be controlled at low levels, the air-gas equivalence ratio should be selected below 0.8 φ.

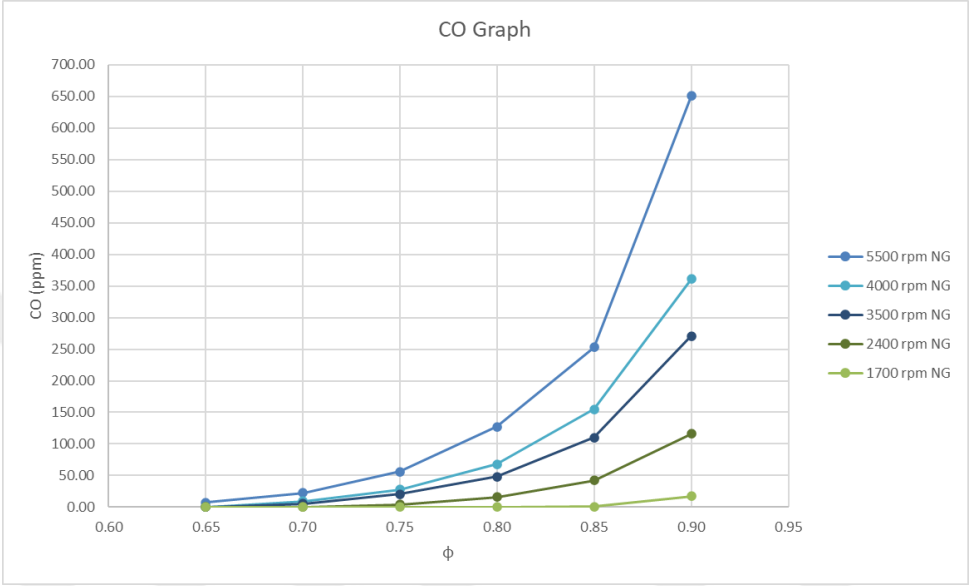


Figure 4.15 The variation graph of CO emission when changing the air-gas equivalence ratio for natural gas

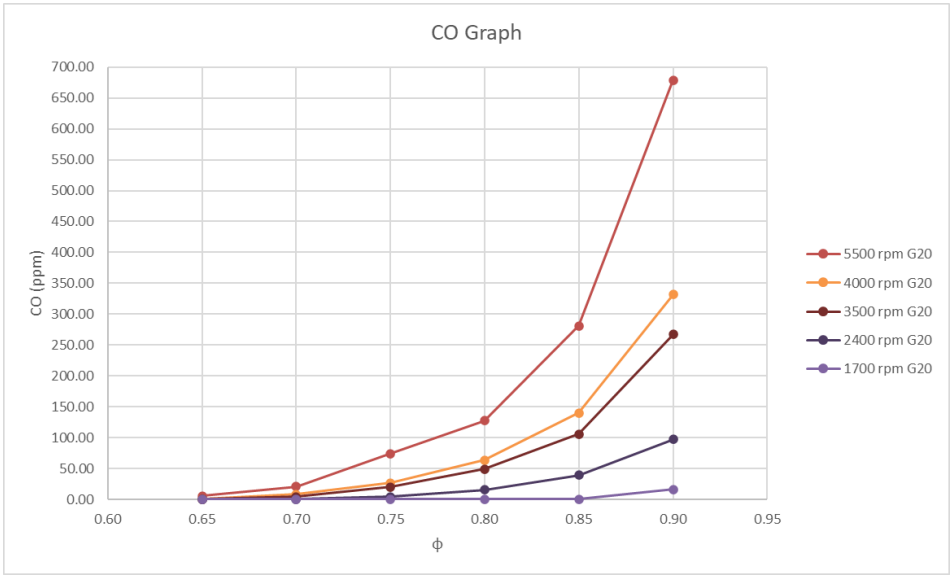


Figure 4.16 The variation graph of CO emission when changing the air-gas equivalence ratio for G20 gas

The air-gas equivalence ratio (φ) is adjusted from 0.65 to 0.90 for each fan speed and gas type. Figure 4.17 and Figure 4.18 show the variation graphs of NO emissions when the air-gas equivalence ratio (φ) is changed. Figures 4.17 and 4.18 show the same variation trends for NO emissions operated by the natural gas and G20. NO emissions for 0.9 φ at natural gas are slightly more than the G20 state. This result is related to the composition of natural gas. Natural gas from domestic pipelines includes 0.22 – 0.47% N gas inside. However, the increased rate of NO emission has a high slope when the air-gas equivalence ratio is adjusted as 0.80 and above, like the CO emission trend. For 3500 and 2400 rpm fan speeds operated with natural gas, NO emissions are measured higher than the 5500 rpm fan speed. It means that the formation of NO emissions is important for the 60%-40% modulation range. If the NO emissions need to be controlled at low levels, the air-gas equivalence ratio should be selected below 0.8 φ.

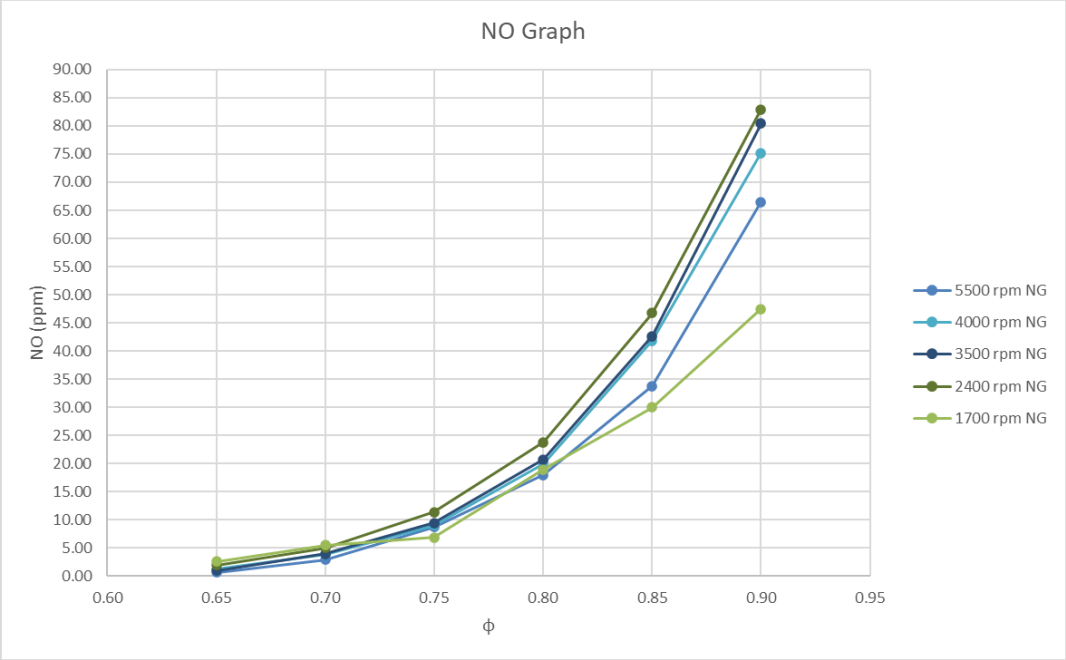


Figure 4.17 The variation graph of NO emissions when changing the air-gas equivalence ratio for natural gas

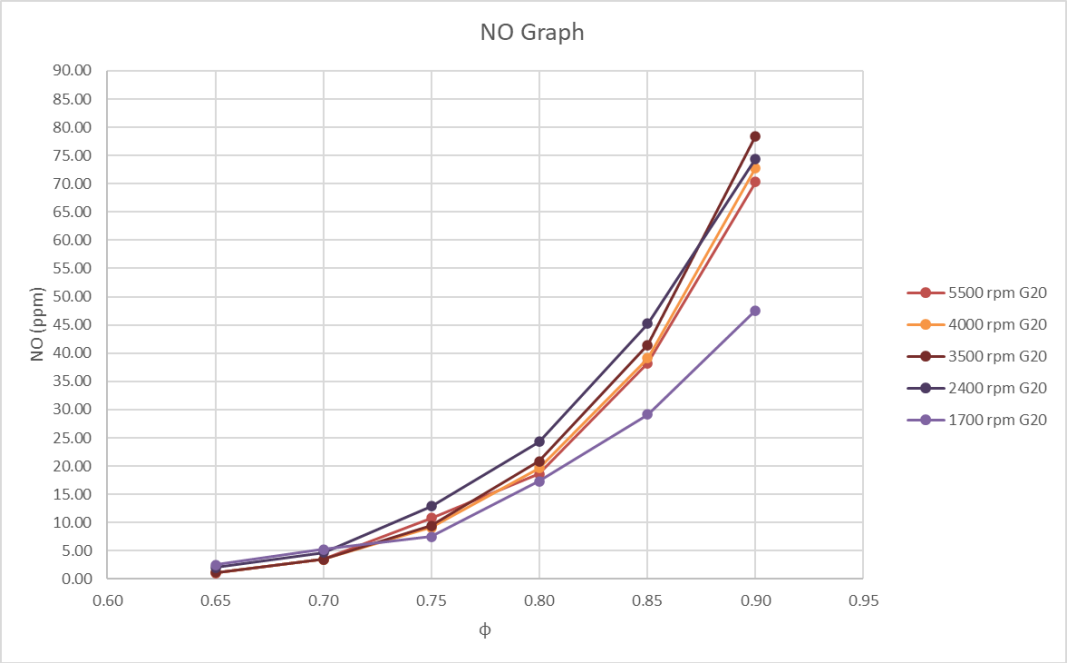


Figure 4.18 The variation graph of NO emissions when changing the air-gas equivalence ratio for G20 gas

Figure 4.19 and Figure 4.20 show the variation graphs of NO_2 emissions when the air-gas equivalence ratio (φ) is changed. Figures 4.19 and 4.20 show the same variation trends for NO_2 emissions operated by the natural gas and G20. However, the increased rate of NO_2 emission has a high slope when the air-gas equivalence ratio is adjusted as 0.85 and above. NO_2 emission is not measured as zero for any design point. If the NO emissions need to be controlled at low levels, the air-gas equivalence ratio should be selected below 0.75 φ.

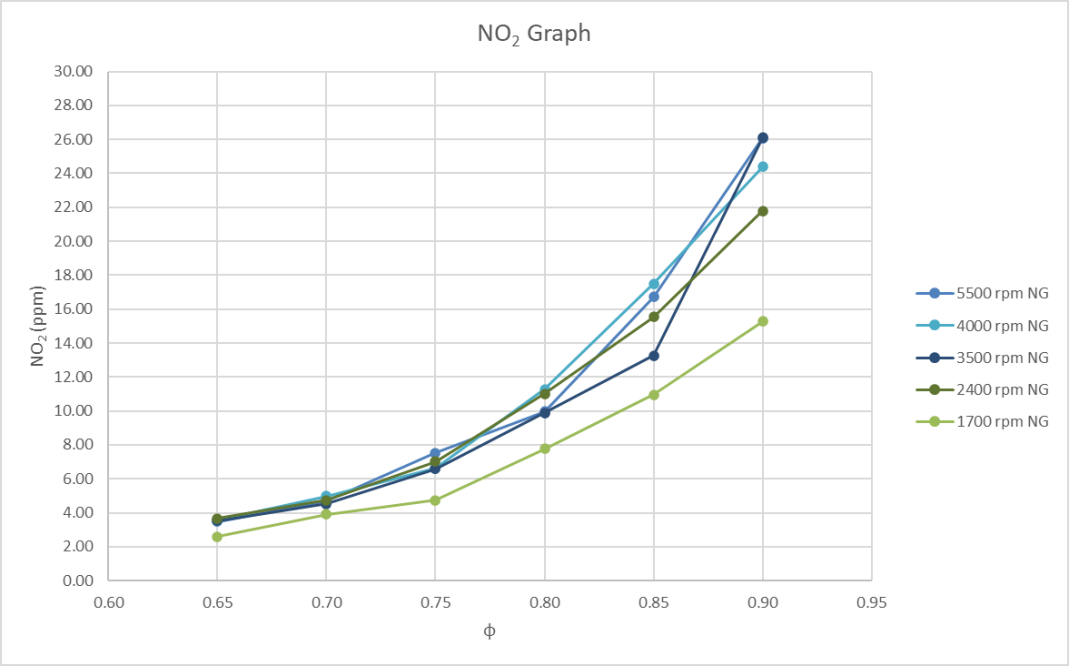


Figure 4.19 The variation graph of NO_2 emissions when changing the air-gas equivalence ratio for natural gas

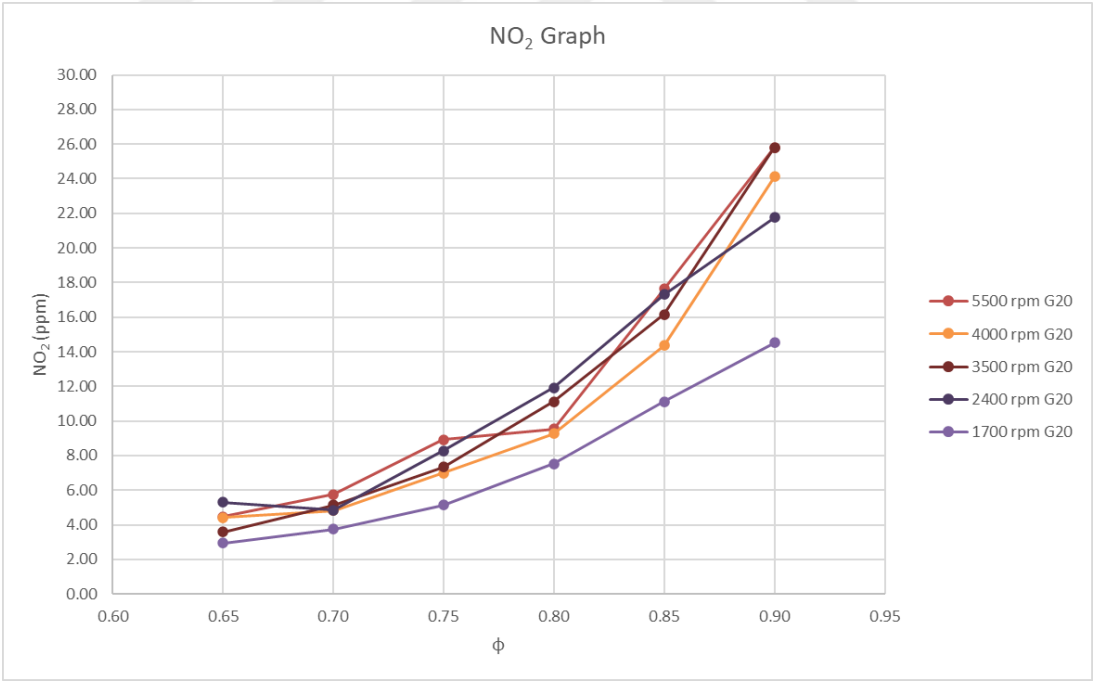


Figure 4.20 The variation graph of NO_2 emissions when changing the air-gas equivalence ratio for G20 gas

4.3.2 The Effects of the Fan Speed on the Boiler Performance

The fan speed is changed from 1700 to 5500 rpm for each air-gas equivalence ratio (φ) and gas type. Figure 4.21 and Figure 4.22 show the variation graphs of input heat load (Q_c) when the fan speed is changed. According to Figures 4.21 and 4.22, the same variation trends are seen for input heat loads operated by the natural gas and G20. Input loads at G20 are more than the natural gas state. This result is related to the composition of G20 gas. G20 provided from special tubes includes 100% CH_4 gas inside. When the fan speed increases, input heat loads increase for all air-gas equivalence ratios (φ). If the input heat load needs to be increased, the fan speed can be selected higher.

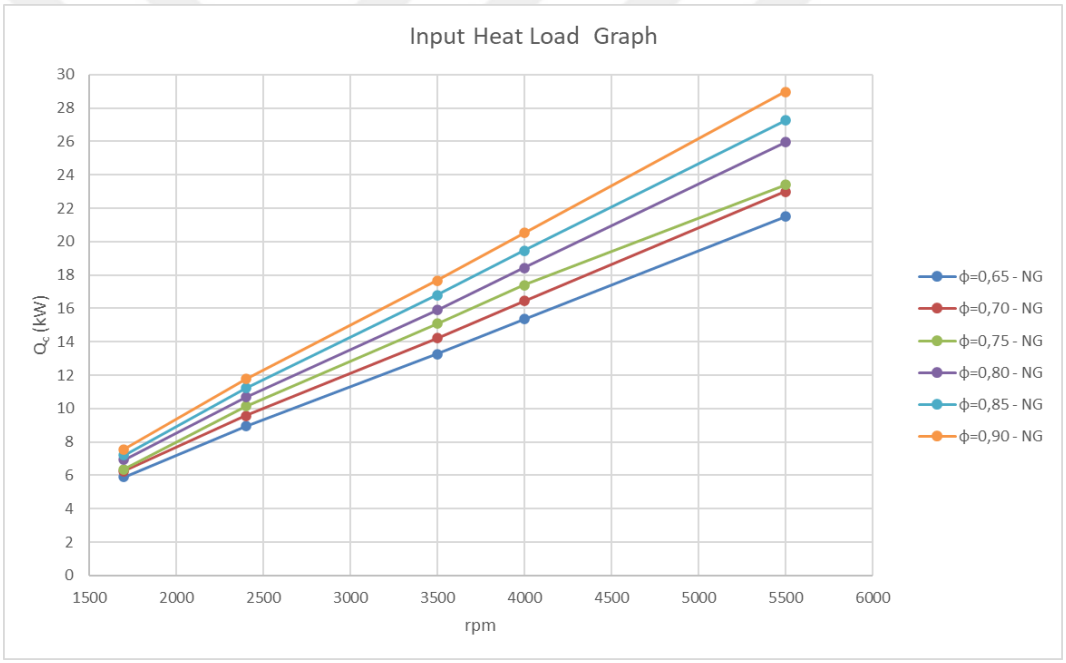


Figure 4.21 The variation graph of input heat load when changing the fan speed for natural gas

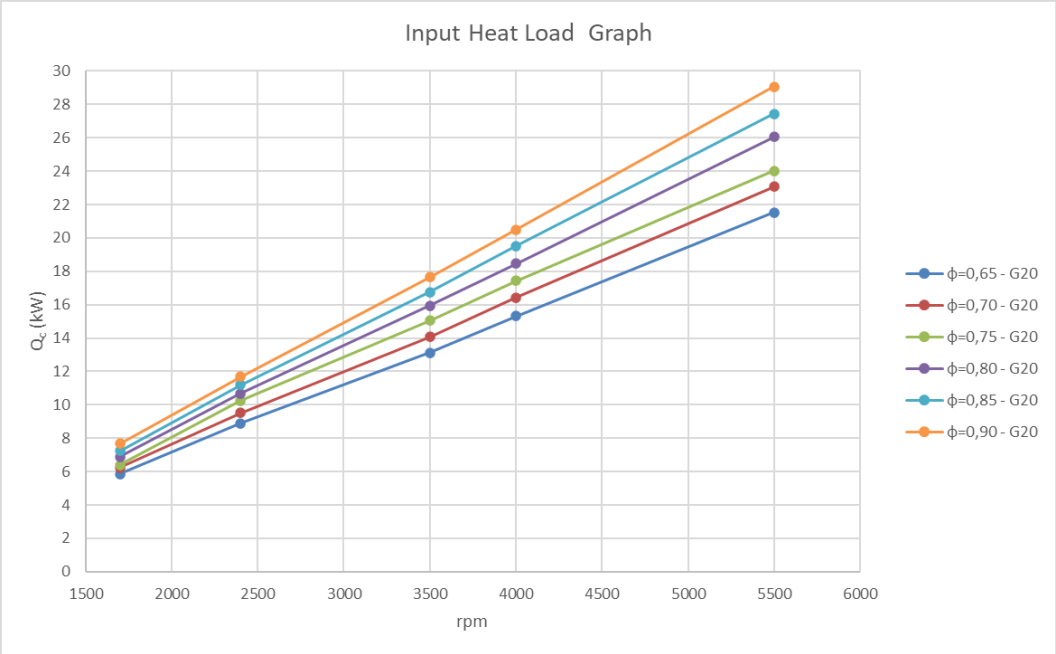


Figure 4.22 The variation graph of input heat load when changing the fan speed for G20 gas

The fan speed is changed from 1700 to 5500 rpm for each air-gas equivalence ratio (φ) and gas type. Figure 4.23 and Figure 4.24 show the variation graphs of CO emission when the fan speed is changed. Figures 4.23 and 4.24 show the same variation trends for CO emissions operated by natural gas and G20. When the fan speed increases, CO emission increases for all air-gas equivalence ratios (φ). For high air-gas equivalence rates, especially 0.9 φ, CO emissions increase dramatically. If the CO emissions need to be controlled at low levels at all fan speeds, the air-gas equivalence ratio should be selected below 0.75 φ.

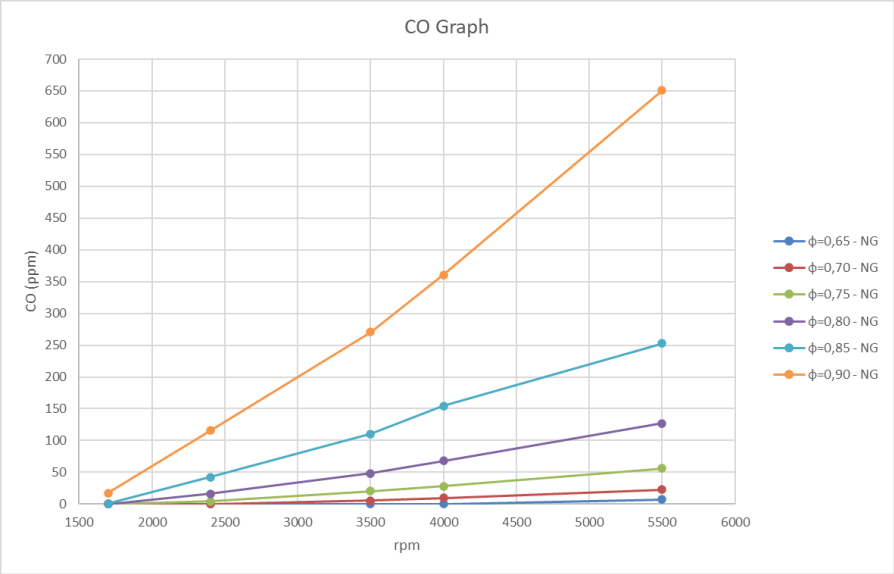


Figure 4.23 The variation graph of CO emission when changing the fan speed for natural gas

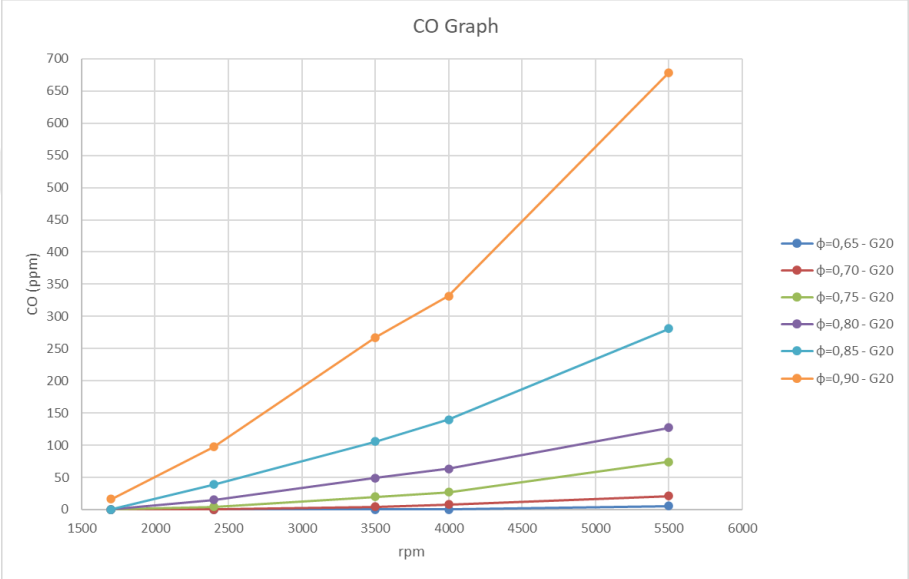


Figure 4.24 The variation graph of CO emission when changing the fan speed for G20 gas

The fan speed is changed from 1700 to 5500 rpm for each air-gas equivalence ratio and gas type. Figure 4.25 and Figure 4.26 show the variation graphs of NO emissions when the fan speed is changed. Figures 4.25 and 4.26 show the same variation trends for NO emissions operated by the natural gas and G20. All fan speeds have low NO emissions and stable trends for 0.65, 0.70, and 0.75 air-gas equivalence ratio

(φ). When the fan speed is increased from 1700 rpm to 2400 rpm, the increased rate of the NO emission has a high slope for 0.90 and 0.85 air-gas equivalence ratio.

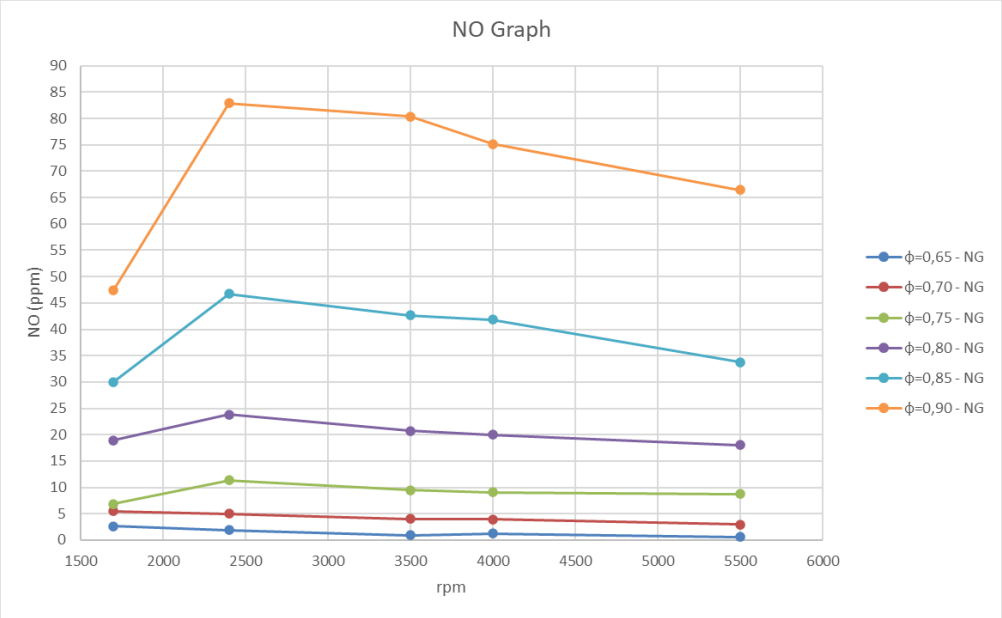


Figure 4.25 The variation graph of NO emission when changing the fan speed for natural gas

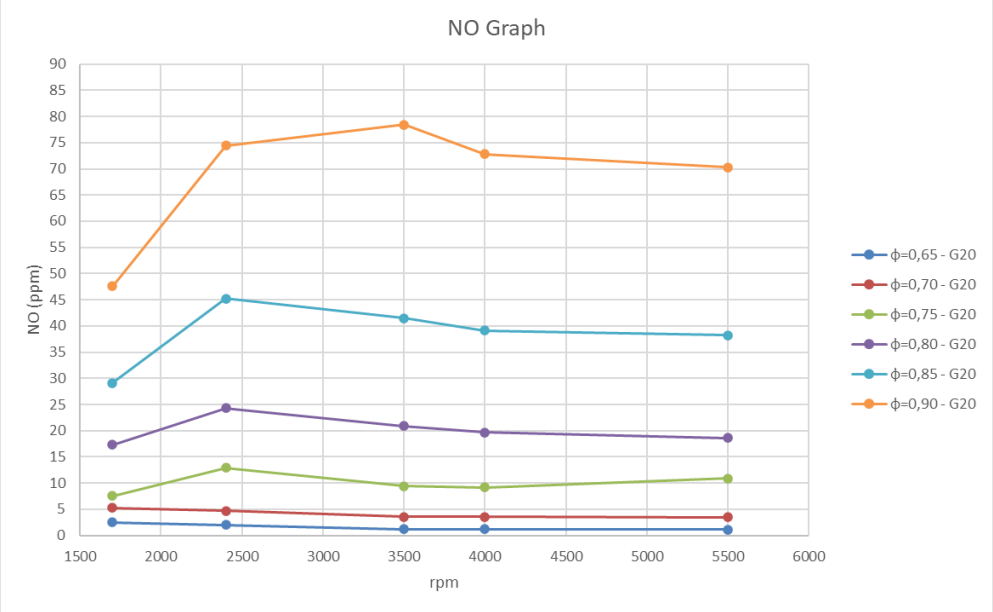


Figure 4.26 The variation graph of NO emission when changing the fan speed for G20 gas

Figure 4.27 and Figure 4.28 show the variation graphs of NO_2 emissions when the fan speed is changed. Figures 4.27 and 4.28 show the same variation trends for NO_2

emissions operated by the natural gas and G20. If the NO and NO_2 emissions need to be controlled at low levels, the air-gas equivalence ratio should be selected below 0.75 φ.

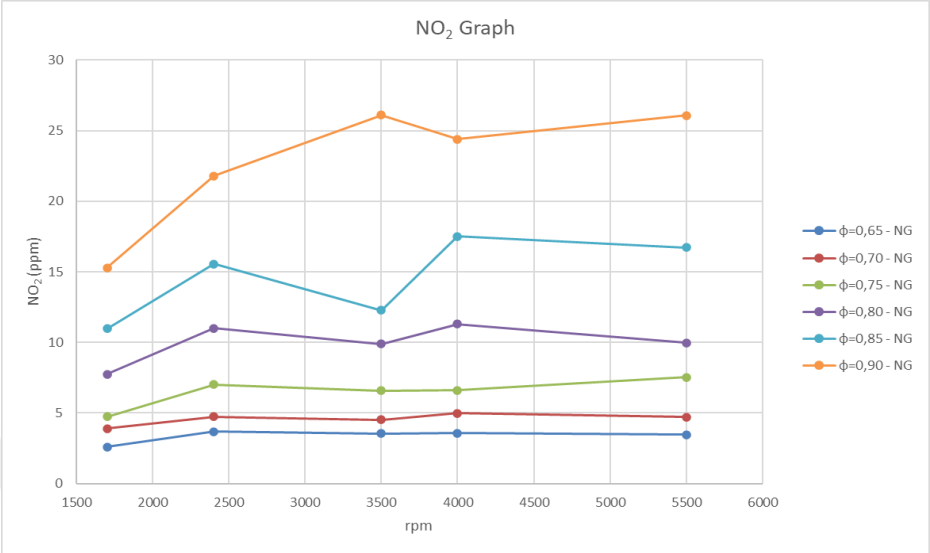


Figure 4.27 The variation graph of NO_2 emission when changing the fan speed for natural gas

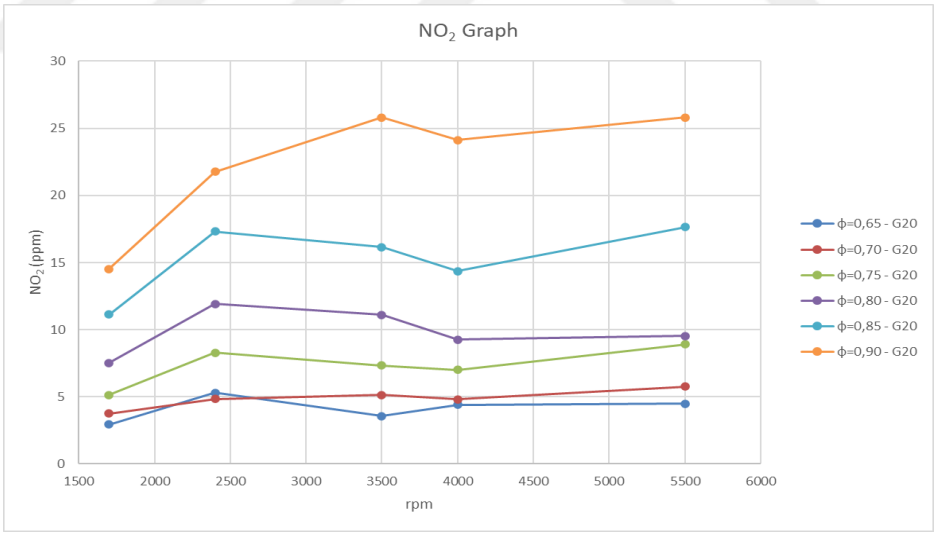


Figure 4.28 The variation graph of NO_2 emission when changing the fan speed for G20 gas

4.3.3 The Determination of Optimum Design Point

When the condensing boiler is designed or developed, input heat loads and emissions are crucial to catch target values. Target values are determined at the beginning of the study. As mentioned before, this investigated condensing boiler was developed according to the 23 kW nominal and 6 kW minimum input heat loads. EN15502 standards, as well as limit emissions. The most important emission value is NO_x emission. The NO_x measurement tests are carried out according to the EN15502 standard. The emission values are measured while the condensing boiler operates at modulation ratios of 100% (maximum input heat load), 70%, 40%, and 26% (maximum input heat load). After that, the NO_x value of the boiler is calculated as mg/kWh.

Figure 4.29 and Figure 4.30 show the NO and NO_2 emission distributions of the initial state measured at different air-gas equivalence ratios (φ) and modulation ratios (input heat loads). The most important emission values for the NO_x calculation are NO and NO_2 emissions. Red dot lines on graphs indicate the 100%, 70%, 40%, and 26% modulation values, which are working condition points to measure NO_x according to the standard. Initial NO_x could be improved if these emissions are reduced below five ppm. According to Figures 4.29 and 4.30, the air-gas equivalence ratios (φ) should be selected 0.70 or 0.65 to catch 23 kW nominal and 6 kW minimum input heat loads.

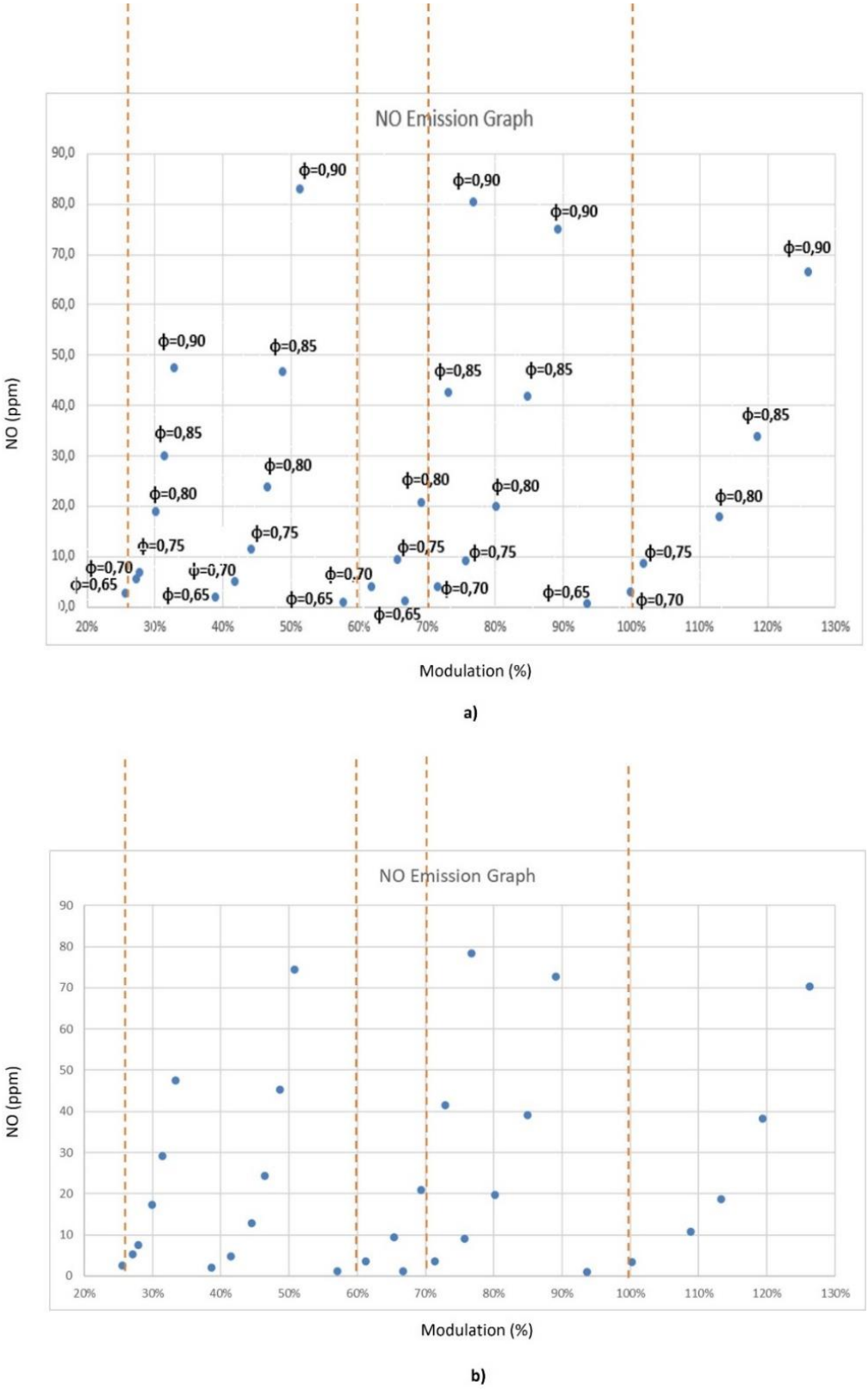


Figure 4.29 The variation graph of NO when changing the modulation ratio of condensing boiler a) φ values are shown, and b) φ values are not shown

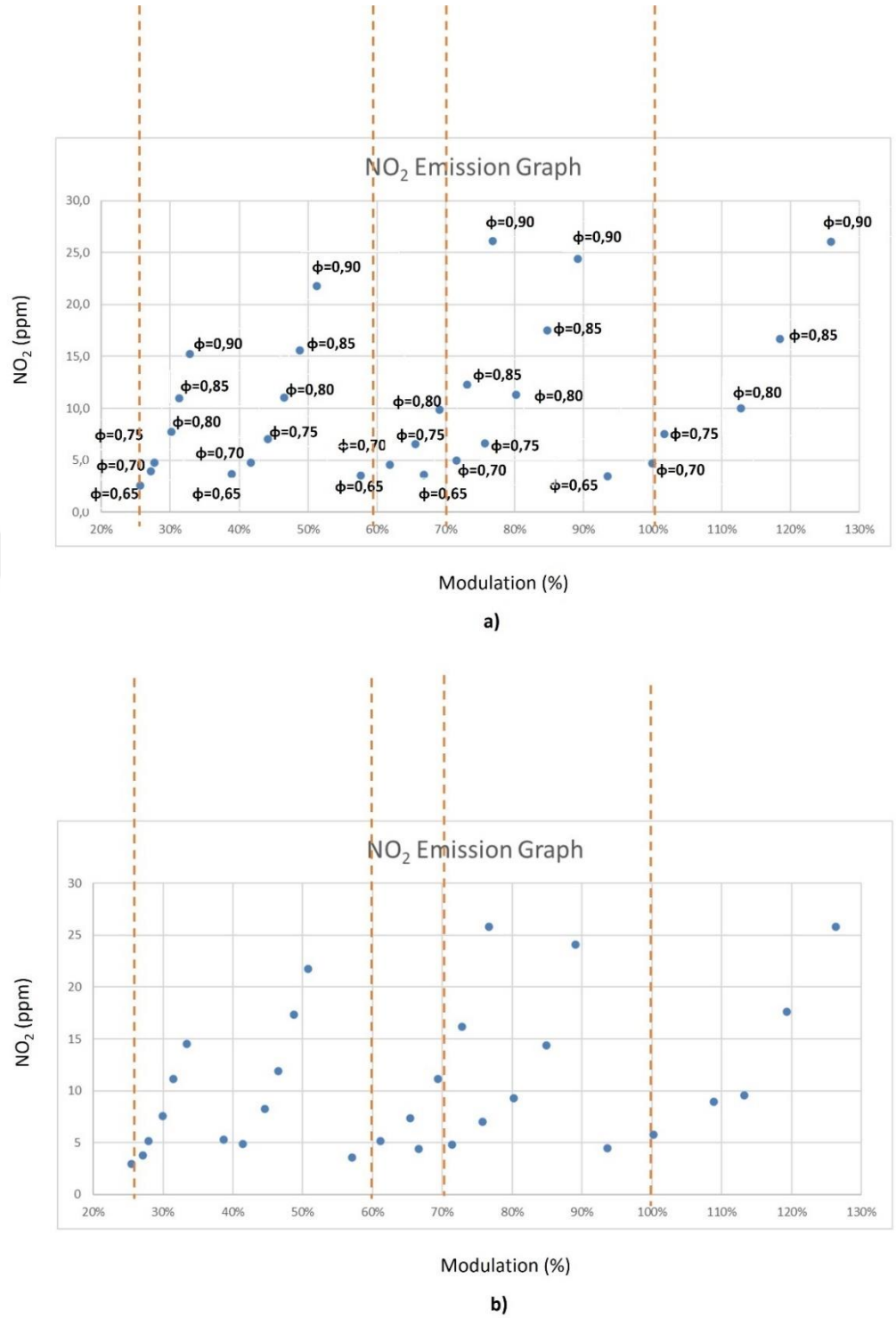


Figure 4.30 The variation graph of NO_2 when changing the modulation ratio of condensing boiler a) φ values are shown, and b) φ values are not shown

The investigated boiler was certificated as a 23 kW nominal input heat load. According to the standard, manufacturers must produce boilers with ± 5% tolerance of

input heat load. With 4000 rpm fan speed, a maximum 20.51 kW input heat load is obtained. There is not enough load in terms of the standard. Figure 4.31 shows the variation graph of Q_c when changing the air-gas equivalence ratio (φ) for 5500 rpm. Only two air-gas equivalence ratios (0.70 and 0.75) provide the target nominal input heat load. The 0.75 φ is the initial design point highlighted with yellow in Table 4.8. The 0.65 φ does not provide enough input load. Therefore, 0.70 φ provides better CO, NO and NO_2 emission with the desired nominal input heat load highlighted in green in Table 4.8.

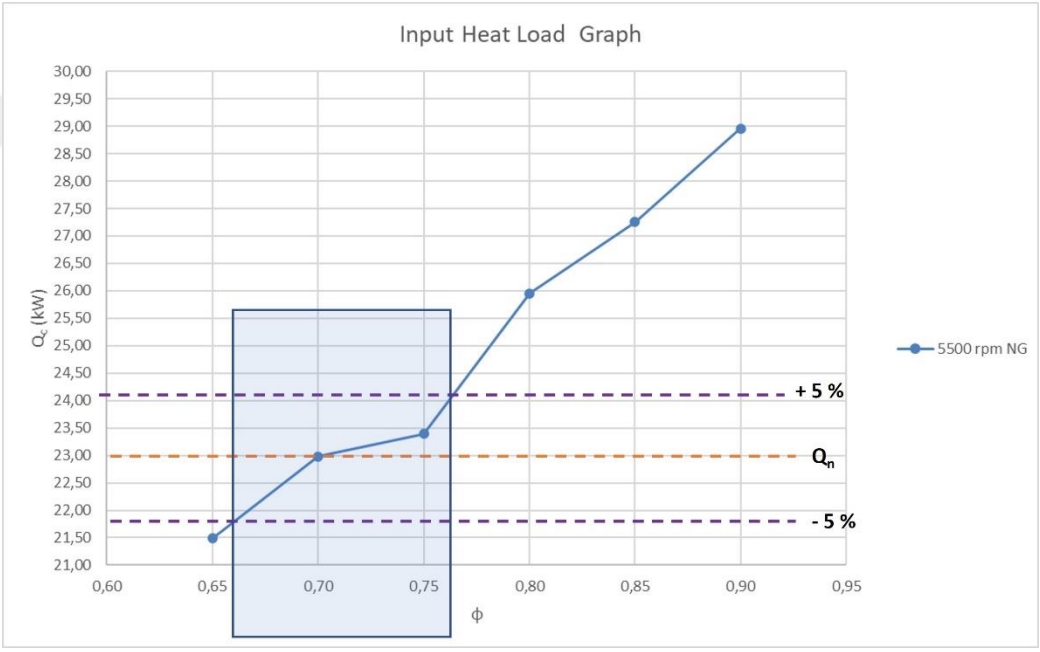


Figure 4.31 The variation graph of Q_c when changing the air-gas equivalence ratio for 5500 rpm

Table 4.8 The emissions for the variation of Qc when changing the air-gas equivalence ratio for 5500 rpm

φ	CO [ppm]	NO [ppm]	NO_2 [ppm]
0.65	7.25	0.63	3.47
0.70	22.49	2.93	4.72
0.75	56.42	8.73	7.54

With 2400 rpm fan speed, a minimum 8.95 kW input heat load is obtained. There is not enough load in terms of the standard (6 kW ± 5%). Figure 4.32 shows the variation graph of Qc when changing the air-gas equivalence ratio (φ) for 1700 rpm. Only two air-gas equivalence ratios (0.65 and 0.70) provide the target minimum input heat load. The 0.75 φ is the initial design point highlighted with yellow in Table 4.8. The 0.65 and 0.70 φ provide better CO, NO and NO_2 emission with the desired minimum input heat load. The best values are measured with 0.65 φ highlighted in green in Table 4.8.

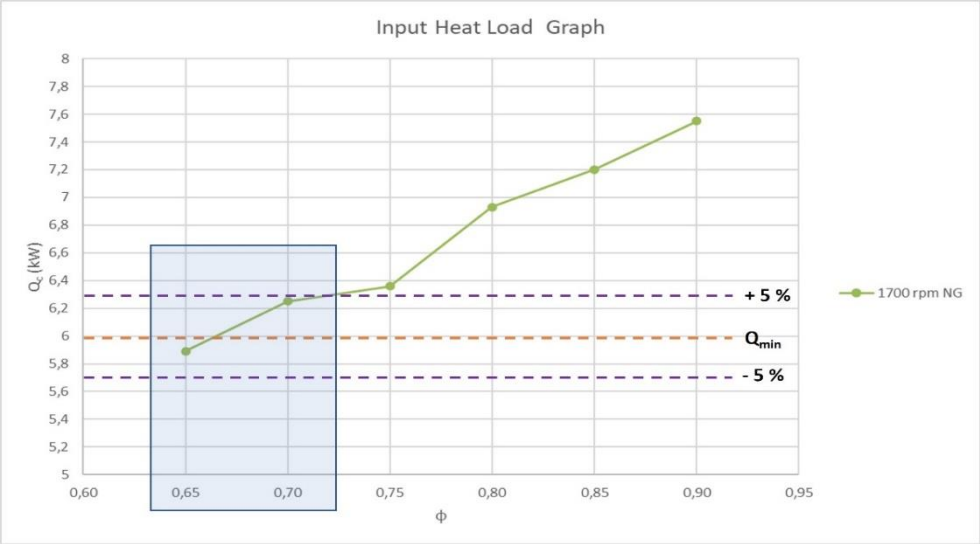


Figure 4.32 The variation graph of Q_c when changing the air-gas equivalence ratio for 1700 rpm

Table 4.9 The emissions for the variation of Qc when changing the air-gas equivalence ratio for 1700 rpm

φ	CO [ppm]	NO [ppm]	NO_2 [ppm]
0.65	0.00	2.60	2.59
0.70	0.00	5.46	3.91
0.75	0.00	6.87	4.74

The selected new air-gas equivalence ratios comply with Figure 4.29 and Figure 4.30 results. The experimental results of the initial and optimum design points are given in Table 4.10. Green highlighted values in the table show the optimum results. 22.98 kW maximum input heat load are achieved with the 0.70 air-gas equivalence ratio (φ), 5500 rpm fan speed and natural gas. This value is 23.06 kW with G20 gas.

5.89 kW minimum input heat load are achieved with the 0.65 air-gas equivalence ratio (φ), 1700 rpm fan speed and natural gas. This value is 5.87 kW with G20 gas.

Table 4.10 Experimental results of initial and optimum design points

Exp. No.	Gas Type	φ	Fan Speed [rpm]	CO [ppm]	NO [ppm]	NO_2 [ppm]	Modulation [%]	Q_c [kW]
2	NG	0.70	5500	2249	2.93	4.72	22.98	100%
3	NG	0.75	5500	56.42	8.73	7.54	23.39	102%
14	NG	0.65	1700	0.00	2.60	2.59	5.89	26%
13	NG	0.75	1700	0.00	6.87	4.74	6.36	28%
8	G20	0.70	5500	20.81	3.46	5.77	23.06	100%
9	G20	0.75	5500	74.29	10.84	8.91	24.03	104%
20	G20	0.65	1700	0.00	2.52	2.93	5.87	26%
19	G20	0.75	1700	0.00	7.54	5.14	6.41	28%

Table 4.11 compares emissions and input heat loads between initial and optimum design points. For the nominal input heat load condition, natural gas consumption is decreased by 2%, adjusted as 0.70 instead of 0.75 air-gas equivalence ratio (φ). Decreasing only 0.05 air-gas equivalence ratio can provide more efficient combustion with the current 5500 rpm fan speed. It means that less natural gas can be consumed with more air. CO, NO and NO_2 emissions are respectively decreased as 60%, 66% and 37%.

Table 4.11 The comparison of emissions and input heat loads between initial and optimum design points

Nominal Input Heat Load	**CO [ppm]**	**NO [ppm]**	**NO_2 [ppm]**	**Q_c [kW]**
Initial Design Case	56.42	8.73	7.54	23.39
Optimum Design Case	22.49	2.93	4.72	22.98
Absolute Difference	33.93	5.80	2.82	0.41
Ratio of Percentage Change	60%	66%	37%	2%
Minimum Input Heat Load	**CO [ppm]**	**NO [ppm]**	**NO_2 [ppm]**	**Q_c [kW]**
Initial Design Case	0.00	6.87	4.74	6.36
Optimum Design Case	0.00	2.60	2.59	5.89
Absolute Difference	0.00	4.27	2.15	0.47
Ratio of Percentage Change	-	62%	45%	7%

For the minimum input heat load condition, natural gas consumption is decreased by 7% with an adjusted 0.65 instead of 0.75 air-gas equivalence ratio (φ). Decreasing only 0.1 air-gas equivalence ratio (φ) can provide more efficient combustion with the current 1700 rpm fan speed. It means that less natural gas can be consumed with more air. NO and NO2 emissions are respectively decreased as 62% and 45%.

Finally, the NO_x emissions are calculated for the initial and optimum design points according to the EN15502 standard. The initial NO_x emission is 35.26 mg/kWh. As a result of the improvements in emissions with the selected air-gas equivalence ratio (φ), new NO_x emissions are calculated as 19.06 mg/kWh. This optimum design has less than 46% NO_x emission according to the EN15502 standard. This result is crucial to creating an environmental product that only adjusts the air-gas equivalence ratio (φ) at the same fan speeds.

4.4 The 153 kW Condensing Boiler Experiments

This study aims to prototype a new wall-hang condensing boiler with a big output capacity developed with the results of numerical and experimental studies presented in this thesis. The first step of developing a condensing heat engine is determining the boiler's maximum and minimum input loads. These input loads can indicate the modulation range of the boiler, as well. The maximum input load is 153 kW, and the minimum is 31 kW for the developing condensing boiler. The modulation range is determined as 20%.

Most wall-hang condensing boilers have a premix combustion unit, pneumatic gas/air mixing system (Figure 4.10) and heat exchanger. The heat exchanger is designed to reach the 153 kW maximum input load. The optimum design parameters were determined with numerical analyses in Chapter 3.4. The optimum design parameters of the finned tube heat exchanger are given in Table 3.17. The aluminium heat exchanger is designed and manufactured according to the optimized fin details (Figure 4.33). The fin height is 10 mm, the fin thickness is 0.5 mm, and the fin spacing is 3.5 mm.

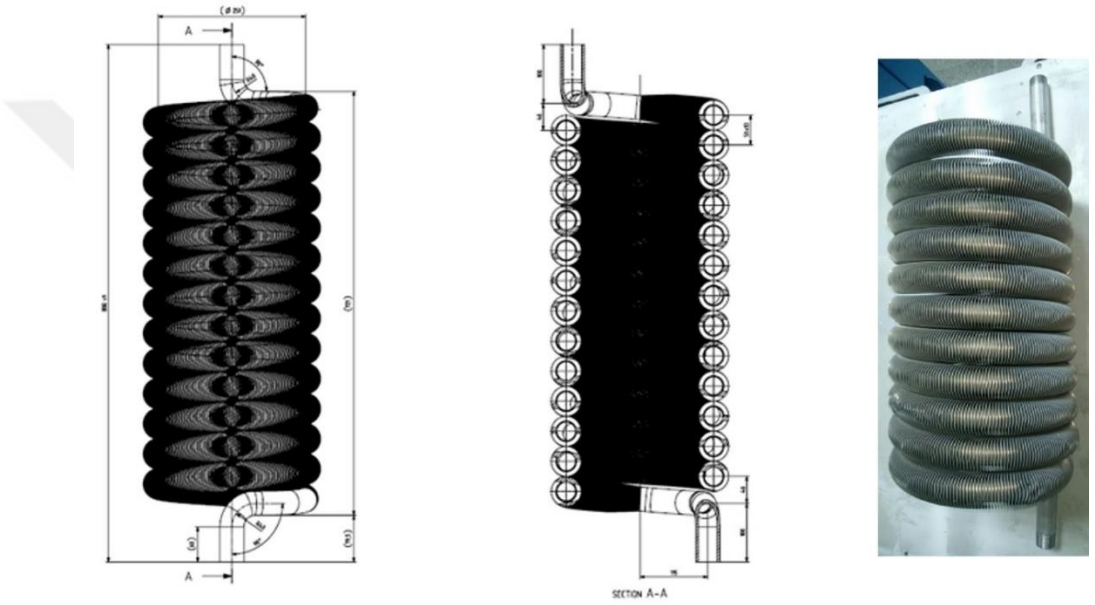


Figure 4.33 The aluminium heat exchanger for 153 kW wall-hang condensing boiler

A three-dimensional general view of the heat engine unit is given in Figure 4.34. All parts used in the heat engine unit are designed for the first time, consisting of parts such as the burner door, electrodes, burner, outer shield, and condensing collector. As seen in Figure 4.34, the cold-water inlet is designed to be on the lower side of the heat engine and the hot water outlet is located on the burner door. After the flue gas is formed in the combustion area, it is discharged from the outlet area modelled on the condensing collector. The outlet area is designed to discharge the condensed water on the bottom collector safely. The cross-sectional view of the heat engine unit and its essential parts is given in Figure 4.34. An insulation part is suitably designed for the

geometry of the burner door to prevent the burner door from high temperatures due to the flue gas formed in the combustion area.

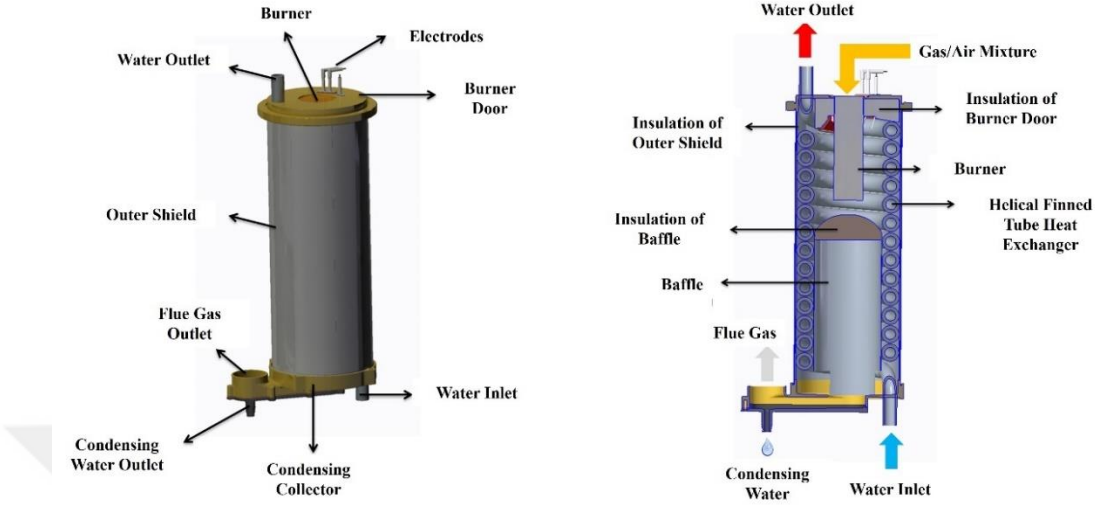


Figure 4.34 The design of the heat engine for the 153 kW wall-hang condensing boiler

A multi-hole cylindrical burner made of stainless-steel material with a similar type used in the 23 kW wall-mounted condensing boiler is used as the burner shown in Figure 4.35. The general dimensions of the burner are determined according to the form of the finned tube aluminium helical heat exchanger and the height of the condensation zone. In order to provide a thermal load of 153 kW, burner prototypes with a diameter of 80 mm and a length of 297 mm made of stainless steel are manufactured.

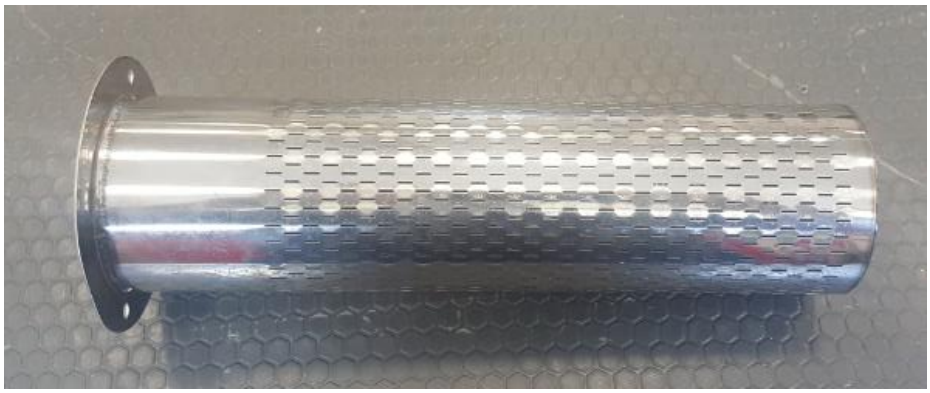


Figure 4.35 The prototype of the designed burner

The part that separates the internal volume of the heat engine from the ambient air is the outer shield. The insulation sheet, which has a 2 mm thickness, is assembled between the heat exchanger and outer shield to prevent heat loss from the outer shield to the ambient air.

The baffle part is designed to provide the flue gas entering the condensate region and to prevent discharging the flue gas at high temperatures from the outlet of the condensing collector. This baffle consists of a dome-shaped insulation material and a cylindrical sheet metal part in a stainless-steel sleeve.

The condensing collector shown in Figure 4.34 ensures the discharge of the flue gas whose temperature has decreased while ensuring that the condensed water is safely removed from the heat engine unit. With the pull slots designed in the condensing collector and the burner door, the heat engine is assembled as fully tightness.

Insulation parts' prototypes, which are resistant to high flue gas temperatures and provide a thermal barrier, are manufactured from calcium-magnesium-silicate material.

Convenient details are designed for assembling many parts (burner, fan, gas valve, electrodes, high-temperature thermostat and so on) on the burner door. Since the burner door is close to the high-temperature region, its prototype is manufactured from aluminium.

The condensing collector has two main functions. It is the safe removal of low-temperature flue gas and condensate water from the heat engine. It should be manufactured from materials resistant to acidic condensation water and flue gas temperatures of 120 °C. The prototype of the condensing collector is produced with a three-dimensional printer.

After the prototype production of other parts of the combustion unit is completed, the assembly processes of the heat engine are carried out. Figure 4.36 shows the internal volume of the heat engine's high-temperature region. The magnesium-calcium-silicate materials shown in Figure 4.36 are insulation parts. The burner part enters the volume formed with the heat exchanger.

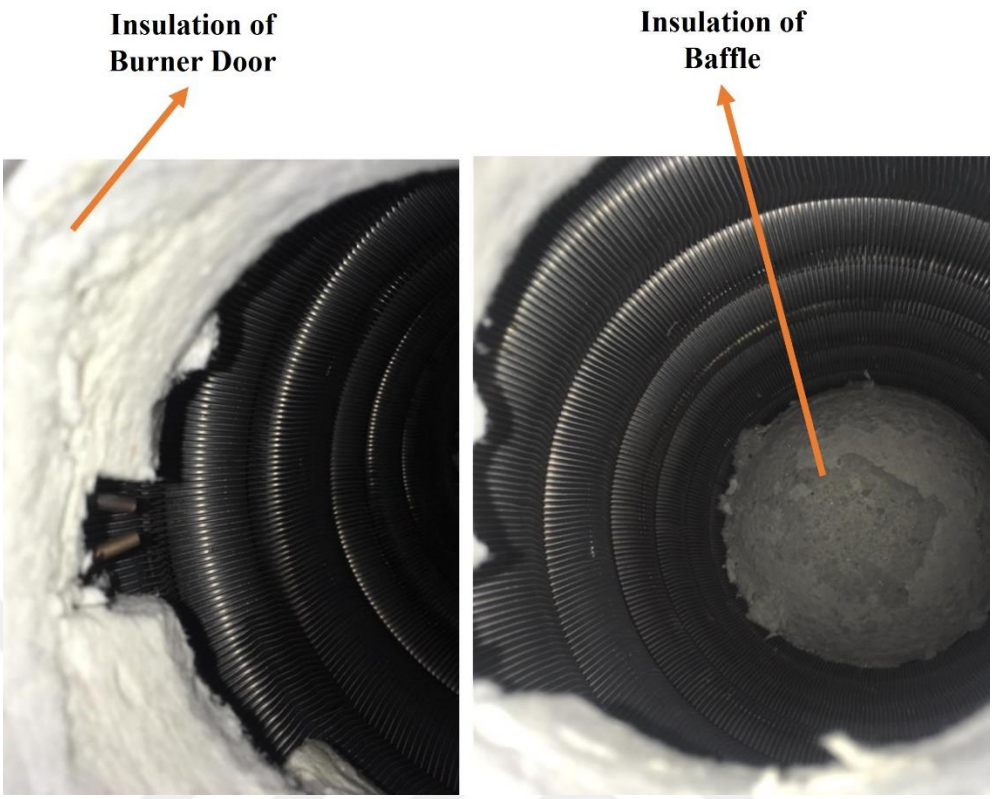


Figure 4.36 The internal view of the heat engine's prototype

After the assembly of the heat engine, the fan, gas valve, venturi, electronic card, electronic safety equipment and all other parts that can provide a thermal load of 153 kW are selected and supplied. Thus, the prototype of the functional wall-hang condensing boiler with a capacity of 153 kW, shown in Figure 4.37, is manufactured.



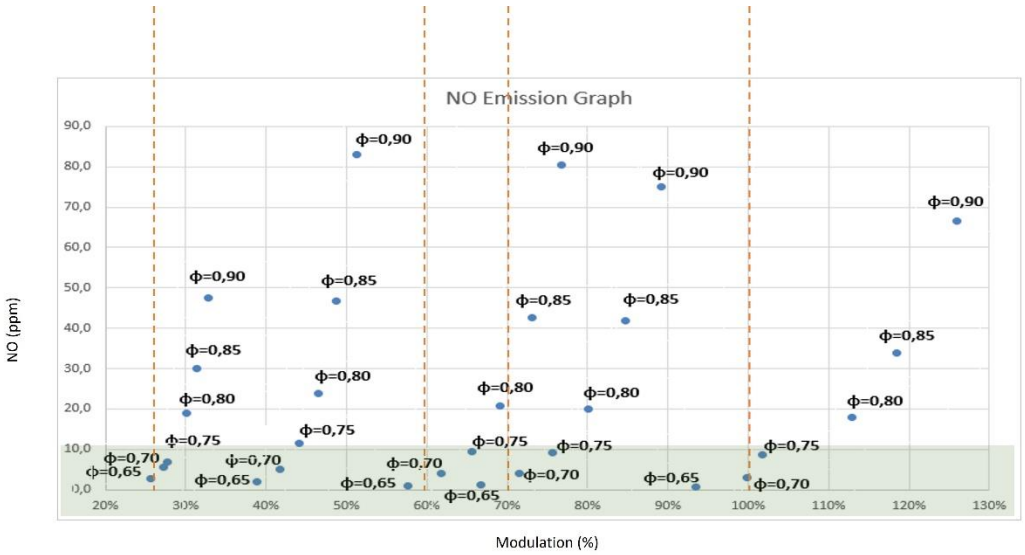
Figure 4.37 The internal view of the heat engine's prototype

The wall-hang condensing boiler shown in Figure 4.37 is installed on a fully equipped and calibrated test rig. First, the water and gas connections of the functional prototype are done. The water pressure in the test rig and the boiler is pressurised to be 6 bars. After waiting for 20 minutes, all parts are checked, and the water leakage test is completed successfully. Then, 20 mbar of G20 gas was supplied to the gas line, and all gas connections were checked with a gas leakage detector while the electrical connection of the boiler was off. After completing the gas leakage test, the prototype boiler is ready for the first ignition.

With the heat demand for the boiler, the high-capacity wall-hang condensing boiler is fired for the first time and development tests are started.

When starting development tests, it is important to determine the appropriate air-gas equivalence ratio (φ) for the device's nominal and minimum input loads. The wall-hang condensing boiler was investigated experimentally in the previous experimental study, which has small capacity (23 kW input load). The optimum operating points were determined to provide the best emission values with desired input loads. These equivalence ratios determine the desired input loads and affect the formation of NO and NO_2 emissions. The emission distribution graphs given in Figure 4.38 for the 23 kW wall-hang condensing boiler were examined experimentally in the previous section. The green area on the graphs indicates a low emission zone for all modulation ratios when the air-gas equivalence ratio (φ) is adjusted below 0.75. Since the combustion system is similar in scalability, the information obtained here has guided the development tests of the preliminary prototype of the 153 kW wall-hang condensing boiler.

According to the information obtained from all the experimental and numerical studies conducted within the scope of the thesis, the optimum parameters of the combustion values that provide the 153 kW maximum input load have been determined with a few trials.



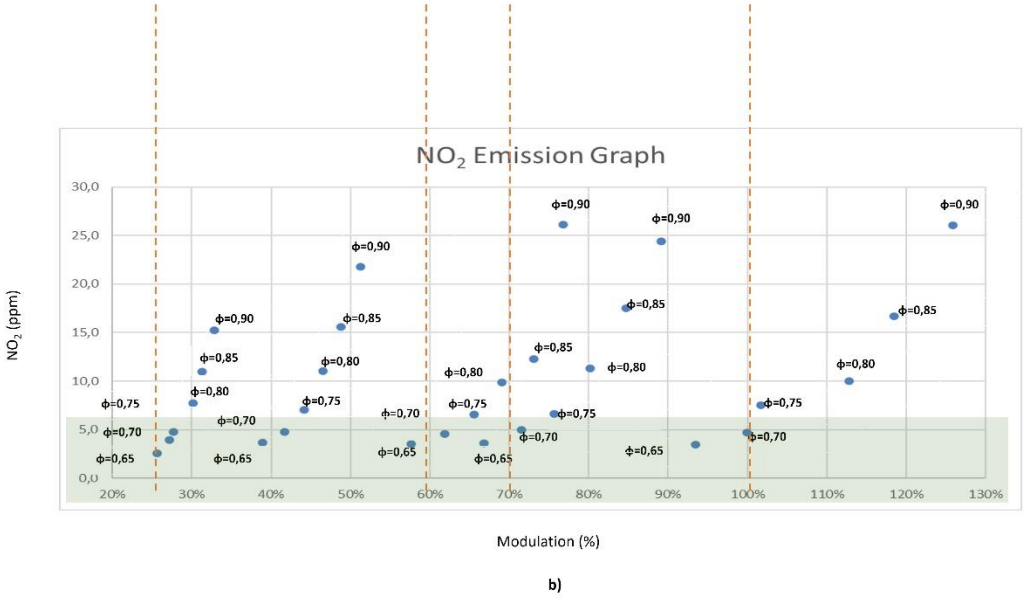


Figure 4.38 The variation graph of emissions when changing the modulation ratio of 23 kW wall-hang condensing boiler a) NO emission b) NO_2 emission

The functional prototype's air-gas equivalence ratio (φ) at the maximum input load (nominal input load, Q_n) is selected as 0.75. Emission and performance values of this working point are given in Table 4.12. The functional prototype has a maximum input load of 153.15 kW. Operating at this nominal condition, 8.70% CO_2, 180 ppm CO, 14.63 ppm NO and 7.29 ppm NO_2 emission values are measured.

Table 4.12 The performance and emission values for maximum input load (nominal input load, Q_n)

Maximum Input Load	**Q_n [kW]**	**Modulation Ratio [%]**	**CO_2 [%]**	**CO [ppm]**	**NO [ppm]**	**NO_2 [ppm]**	**$T_{flue\ gas}$ [°C]**
	153.15	100	8.70	180	14.63	7.29	54.34

The functional prototype's air-gas equivalence ratio (φ) at the minimum input load (Q_{min}) is selected as 0.72. Emission and performance values of this working point are given in Table 4.13. The functional prototype has a minimum input load of 30.60 kW. Operating at this minimum condition, 8.30% CO_2, 38 ppm CO, 4.43 ppm NO and 2.98 ppm NO_2 emission values are measured.

Table 4.13 The performance and emission values for minimum input load (Q_{min})

Minimum Input Load	**Q_n [kW]**	**Modulation Ratio [%]**	**CO_2 [%]**	**CO [ppm]**	**NO [ppm]**	**NO_2 [ppm]**	**$T_{flue\ gas}$ [°C]**
	30.60	20	8.30	38	4.43	2.98	32.98

While the nominal 153 kW input load is operating, the temperature measurements are performed from the outer shield surface on the heat engine and burner door (Figure 4.39). The highest temperature is measured as 66.6 °C on the burner boor. The designed insulation parts inside the heat engine minimise the thermal losses transferred to the ambient.



Figure 4.39 Combustion unit surface temperature measurements at rated operating condition

The nominal input load value of 153 kW, which is the high-capacity value targeted within the scope of this thesis, is achieved. Experimental measurements are carried out according to EN 15502 standards to determine the NO_x value of the developed boiler prototype. In these experimental measurements, besides the functional boiler prototype's nominal and minimum operating conditions, the emission values at modulation rates of 70%, 60%, and 40% are also important. The experimental results measured during the relevant operating conditions are given in Table 4.14

Table 4.14 The NO_x measurement results according to EN15502

Modulation Ratio [%]	T_{gas} [°C]	P_{gas} [mbar]	$P_{ambiant}$ [mbar]	V_{gas} [m3/h]	Input Load [kW]	$T_{water\ outlet}$ [°C]	$T_{water\ inlet}$ [°C]	$T_{flue\ gas}$ [°C]	CO [ppm]	CO_2 [%]	NO [ppm]	NO_2 [ppm]
100, Q_n	22.6	19.5	933	16.07	153.1	79.2	59.1	54.34	180	8.70	14.63	7.29
70	22.6	19.5	933	11.12	107.1	63.5	47.9	51.11	156	8.63	12.07	5.75
60	22.6	19.5	933	9.52	91.8	57.5	44.15	51.05	104	8.60	12.02	5.83
40	22.6	19.5	933	6.44	61.2	46.7	36.4	42.56	65	8.35	12.01	4.45
20, Q_{min}	22.6	19.5	933	3.17	30.6	32.1	28.47	32.98	38	8.30	4.43	2.98

The NO_x value of the developed boiler prototype with the measurement results obtained at the end of the experiment is determined as 31.45 mg/kWh. The prototype of the high-capacity and low-emission wall-hang condensing boiler targeted within the scope of this thesis has been completed.

CHAPTER FIVE
OPTIMIZATION STUDIES OF CONDENSING BOILER

Experimental studies and computational fluid dynamics and heat transfer (CFDHT) simulations have been essential for modelling, predicting, and optimising fluid behaviour and heat transfer in thermal engineering and scientific applications. Although different, these two methods have a mutually beneficial connection. CFDHT simulations provide cost-effective and rapid insights into fluid behaviour and heat transfer, while experimental studies validate these results and offer real-world data. In recent years, integrating artificial intelligence methods has significantly improved the accuracy, efficiency, and reliability of CFD simulations and experimental studies. Artificial neural networks (ANNs) are one of the artificial intelligence methods.

ANNs can enhance predictive accuracy in CFD simulations and experiments. CFD simulations often rely on simplified mathematical models that may not fully capture fluid dynamics' complex and nonlinear case. On the other hand, artificial neural networks are great at modelling complex data relationships and can learn from large amounts of available CFD and experimental data. Training artificial neural networks on these datasets can improve the accuracy of predictions, which can inform better decisions in engineering and research.

The nature of CFD simulations demands significant computational resources and time. ANNs provide an effective tool to reduce these costs. Artificial neural networks, when trained, can quickly and accurately simulate complex thermal systems in real time. This efficiency accelerates the decision-making and optimization process.

In experimental studies, ANNs play an important role in data analysis. They can recognise complicated correlations in experimental data that might be avoided from traditional statistical methods. This ability is very useful for performing experiments as it helps extract meaningful insights from complex datasets, ensuring accurate and reliable results.

Condensing boilers have gained widespread usage in recent years due to their energy efficiency and reduced environmental impact. It is necessary to consider a complex interplay of variables to achieve the best performance, efficiency, and low emissions. This chapter presents how artificial neural networks (ANNs) can be employed for optimization studies of condensing boilers with numerical and experimental datasets.

In the following section of this chapter, the optimization of design parameters of the finned tube heat exchangers by artificial neural networks for the condensing boilers and the optimization of the performance and emissions of the whole condensing boiler by artificial neural networks with real-time data are discussed.

5.1 Optimization of Design Parameters of the Finned Tube Heat Exchangers by Artificial Neural Networks for the Condensing Boilers

The demand for optimized heat exchangers in condensing boilers is increasing due to the focus on energy efficiency and sustainability in the heating industry. These boilers are important for heating systems as they gain maximum heat from flue gases. The design of heat exchangers, particularly finned tube heat exchangers, is crucial to the performance of condensing boilers due to their central role in heat transfer. Achieving the highest possible thermal performance while minimising material usage and pressure drops is the primary goal of the optimization phase. Using numerical simulations has become an effective method for studying and enhancing heat exchanger designs. These simulations thoroughly investigate finned tube heat exchangers' complex heat transfer mechanisms under various operating conditions. By utilising Artificial Neural Networks (ANNs) in this computational approach, we can effectively improve the performance of condensing boilers.

In this chapter, we explore how to optimize the design parameters of finned tube heat exchangers for condensing boilers using numerical simulation data. Our research uses artificial neural networks to optimize finned tube heat exchangers' design parameters for condensing boilers and bridge the literature gap between numerical simulations and machine learning.

Three hundred fifty design cases were created according to the design parameters of the finned tube heat exchanger used in the condensing boiler and simulated numerically in Chapter 3.4. The numerical results of these design cases are used in artificial neural network modelling. The selected design parameters of the aluminium heat exchanger are fin height (h_f), fin thickness (t_f), and fin spacing (s). The values of these parameters are given in Table 3.14. Total heat transfer (Q_T) on the inner surface of the tube, the maximum temperature on the fins (T_{max}), the pressure drop (ΔP) between the inlet and outlet of internal volume and the total heat transfer ($\bar{Q}_T$) per unit volume of the heat exchanger are also used as output parameters for ANN modelling.

Due to the complexity of fluid dynamics, many thermal problems involving fluids are solved using experimentally derived correlations between input and output parameters. These correlations can be highly nonlinear, making it challenging to predict system performance accurately. Artificial neural networks offer a fast and effective way to model these complex systems and make accurate predictions. Multiple ANN configurations should be developed, and the optimal structure should be selected to predict the performance of finned tube heat exchangers for condensing wall hang boilers accurately.

This study used a feed-forward backpropagation network with a tangent sigmoid activation function for the hidden layer and a linear transfer activation function for the output layer to estimate output values. The Levenberg-Marquardt algorithm is used to determine the weighting coefficients during training. The ANN model's performance depends on the network's topology, including the number of hidden layers and neurons in each layer. These are selected through a trial-and-error process based on input/output parameters, dataset size, and past experiences. The relative error of each output is determined using the method proposed by Kreith and Wang (Kreith, 2000 and Wang, 2000).

$$Er = \frac{|A^t - A^p|}{A^t} \times 100\% \tag{5.1}$$

The neural network's performance is evaluated by comparing predicted results (A_p) to target data (A_t) using root-mean-square (RMS) values defined during training with N data sets (Kreith, 2000; Wang, 2000).

$$\text{rms} = \sqrt{\frac{1}{N}\sum_{i=1}^{N}\left(\frac{A^t - A^p}{A^t}\right)^2} \quad (5.2)$$

The size and topology of a network affect its prediction performance. The selection process of the ANN structure aims to minimise prediction error. Trained network performance is evaluated by comparing its prediction with a separate testing dataset. An ANN model is created for the internal volume of a heat engine using data sets consisting of 345 input-output pairs, as listed in Table 5.1. 95% of the data set was randomly assigned as the training set, while the remaining 5% was used for testing and validating the network.

Table 5.1 shows seven network topologies implemented in MATLAB. The standard deviation of the relative error in predictions (σ) and the average accuracy of predictions (R) are considered (Kreith, 2000; Wang, 2000), as shown in Table 5.2 to evaluate the performance of the ANNs. After the evaluation, topology 3-6-12-8-4 is chosen for testing due to its best performance with a small value of σ=0.01285 and R=1.00018 and a maximum relative error of approximately 9.16%. Most errors are less than 2%, as illustrated in Figure 5.1.

Table 5.1 The comprasion of performance by different ANN topologies

Topology	Error in the training process		Error in the test process	
	Er (%)	rms	R	б
3-3-4	125.16	0.28136	0.97793	0.21220
3-6-4	70.06	0.11330	1.01211	0.16805
3-9-4	41.94	0.06619	1.00486	0.07081
3-12-4	38.34	0.07149	1.00346	0.07410
3-12-8-4	23.47	0.02252	1.00011	0.02319
3-3-6-8-4	16.35	0.02716	1.00043	0.02724
3-6-12-8-4	9.16	0.01263	1.00018	0.01285

Note: the Er (%) is the maximum value among the errors of the two output variables.

$$R = \frac{1}{N}\sum_{i=1}^{N} R_i = \frac{1}{N}\sum_{i=1}^{N} \frac{A^t}{A^p} \tag{5.3}$$

$$\sigma = \sqrt{\sum_{i=1}^{N} \frac{(R-R_i)^2}{N}} \tag{5.4}$$

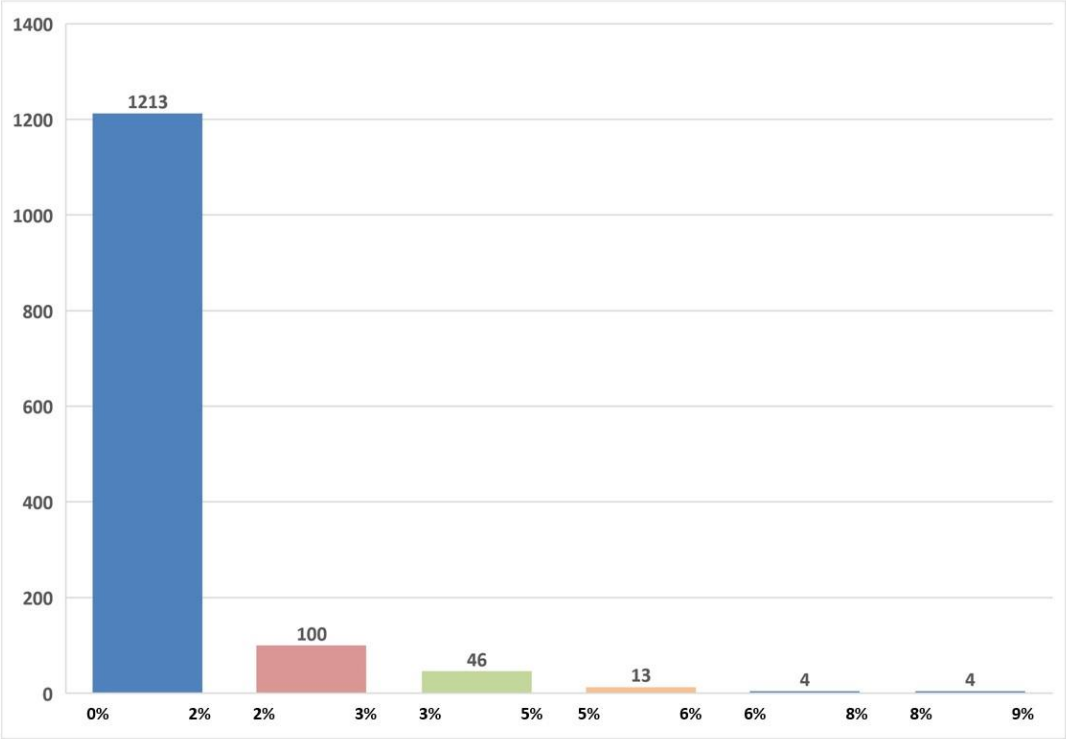


Figure 5.1. The histogram graph of relative errors in the training of the artificial neural network

The best ANN topology with four layers is shown in Figure 5.2. The input parameters for the structure are fin height, thickness, and spacing, with their manufacturing values listed in Table 3.14. The network has three hidden layers, with six, twelve, and eight neurons and four output parameters.

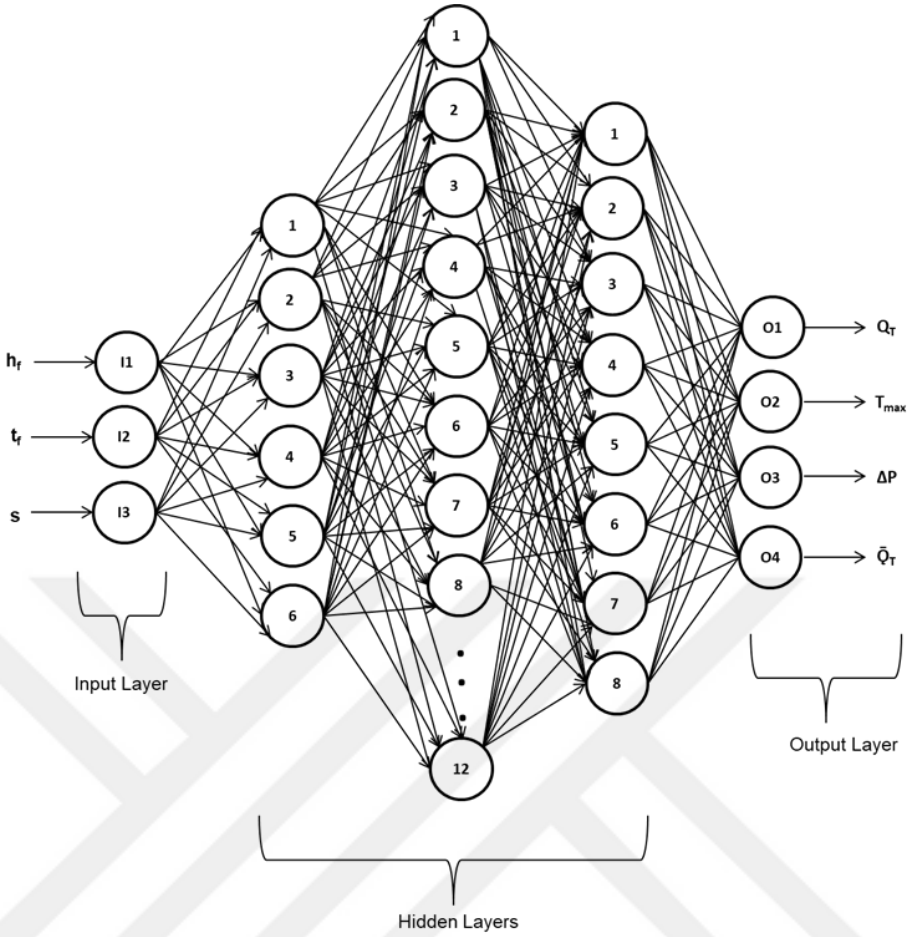


Figure 5.2 The structure selected for ANN modelling

5.1.1 The Results and Discussion of the Optimization of Design Parameters of the Finned Tube Heat Exchangers by Artificial Neural Networks for the Condensing Boilers

The ANN method is used to quickly estimate the output parameters of the finned tube heat exchanger in condensing wall-hang boilers' heat engines. After network training and validation, it can estimate new outputs for different design cases. Five design cases are not used for training, so the network never knows these data sets. Table 5.2 shows the input values of the estimation dataset.

Table 5.2 The input values of the estimation dataset

Estimation Data	h_f [mm]	t_f [mm]	s [mm]
Set 1	1	2.0	2.5
Set 2	4	0.5	1.5
Set 3	5	2.5	3.5
Set 4	6	1.5	4.0
Set 5	10	1.0	2.0

The ANN model produced results within seconds while computing outputs numerically would have taken at least 7 hours.

Artificial neural network predictions are compared to numerical results for total heat transfer (Q_T) on a tube's inner surface in Table 5.3. The maximum absolute difference in predicted values of Q_T is 0.58 W, with a maximum relative error of less than 1.10%. The deviation range of relative errors is 0.09-1.08%, and the prediction accuracy range is 0.99590 - 1.01099. A scatter plot in Figure 5.3 compares numerical and ANN results for Q_T. Three lines are marked on the graph, with the black line indicating an accurate estimation, while the purple and red lines indicate a potential error margin of ±15%. The optimal network topology determines R, MRE, and mean absolute difference as 1.00283, 0.48%, and 0.29 W, respectively.

Table 5.3 The comparison of results for total heat transfer (Q_T) on the inner surface of the tube

Q_T of Estimation Data	Numerical Result	ANN Result	Absolute Difference	Er	R
Set 1	45.13 W	45.09 W	0.04 W	0.10 %	1.00097
Set 2	37.82 W	37.41 W	0.41 W	1.08 %	1.01096
Set 3	83.84 W	83.91 W	0.07 W	0.09 %	0.99912
Set 4	83.27 W	83.62 W	0.34 W	0.41 %	0.99590
Set 5	81.04 W	80.47 W	0.58 W	0.71 %	1.00718

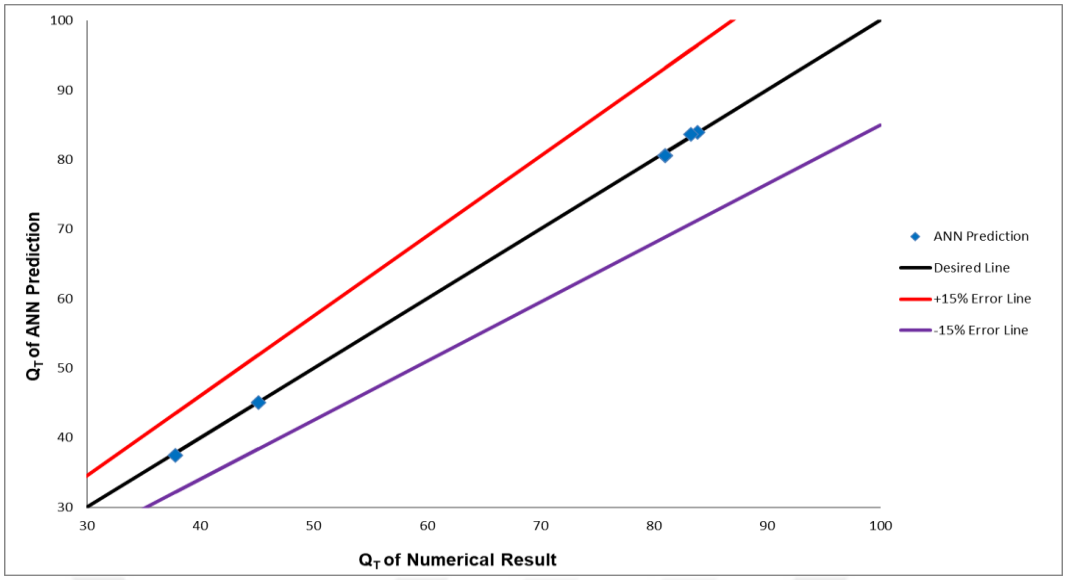


Figure 5.3 The scatter plot of the total heat transfer (Q_T) on the inner surface of the tube

Artificial neural network predictions are compared to numerical results for the maximum temperature on the fins (T_{max}) in Table 5.4. The maximum absolute difference in predicted values of T_{max} is 0.31 ℃, with a maximum relative error of less than 0.33%. The deviation range of relative errors is 0.03 – 0.32%, and the prediction accuracy range is 0.99797 – 1.00321. A scatter plot in Figure 5.4 compares numerical and ANN results for T_{max}. The optimal network topology determines R, MRE, and mean absolute difference as 1.00018, 0.13% and 0.12 ℃, respectively.

Table 5.4 The comparison of results for the maximum temperature on the fins (T_{max})

T_{max} of Estimation Data	**Numerical Result**	**ANN Result**	**Absolute Difference**	**Er**	**R**
Set 1	73.14 ℃	73.11 ℃	0.03 ℃	0.04 %	1.00040
Set 2	95.51 ℃	95.20 ℃	0.31 ℃	0.32 %	1.00321
Set 3	83.14 ℃	83.16 ℃	0.02 ℃	0.03 %	0.99973
Set 4	87.90 ℃	88.08 ℃	0.18 ℃	0.20 %	0.99797
Set 5	115.76 ℃	115.81 ℃	0.05 ℃	0.04 %	0.99958

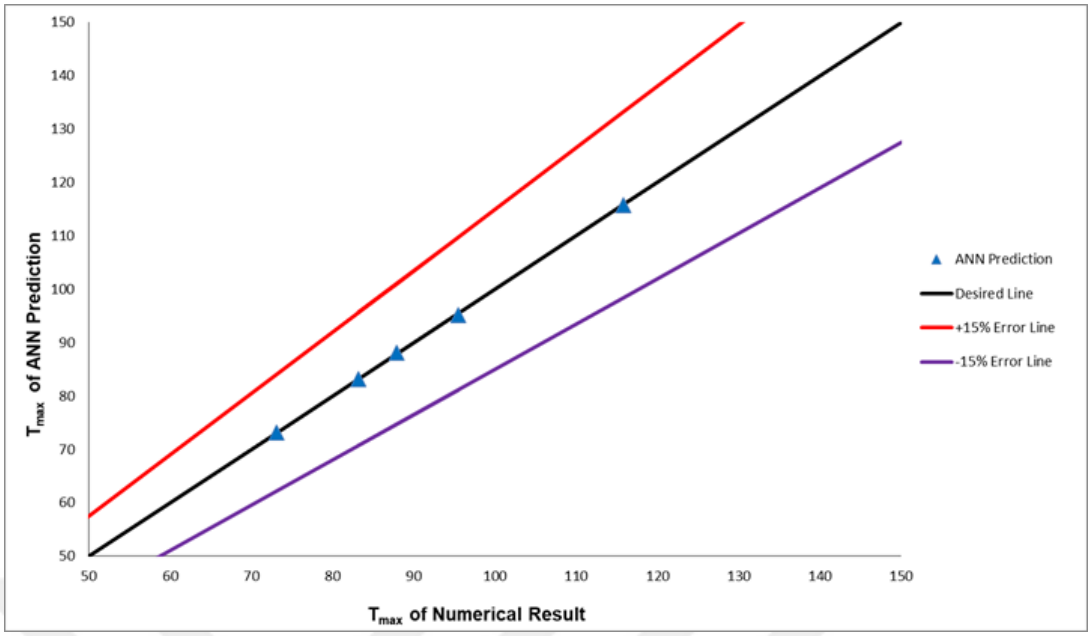


Figure 5.4 The scatter plot of the maximum temperature on the fins (T_{max})

Artificial neural network predictions are compared to numerical results for the total heat transfer ($\bar{Q}_T$) per unit volume of the heat exchanger in Table 5.5. The maximum absolute difference in predicted values of $\bar{Q}_T$ is 0.28 W/mm^3, with a maximum relative error of less than 0.90%. The deviation range of relative errors is 0.10 – 0.87%, and the prediction accuracy range is 0.99534 – 1.02268. A scatter plot in Figure 5.5 compares numerical, and ANN results for $\bar{Q}_T$. The optimal network topology determines R, MRE, and mean absolute difference as 1.00123, 0.44% and 0.11 W/mm^3, respectively.

Table 5.5 The comparison of results for the total heat transfer ($\bar{Q}_T$) per unit volume of heat exchanger

$\bar{Q}_T$ of Estimation Data	**Numerical Result**	**ANN Result**	**Absolute Difference**	**Er**	**R**
Set 1	22.09 W/mm^3	22.11 W/mm^3	0.02 W/mm^3	0.10 %	0.99901
Set 2	32.35 W/mm^3	32.07 W/mm^3	0.28 W/mm^3	0.87 %	1.00875
Set 3	16.72 W/mm^3	16.76 W/mm^3	0.04 W/mm^3	0.22 %	0.99781
Set 4	20.32 W/mm^3	20.42 W/mm^3	0.10 W/mm^3	0.47 %	0.99534
Set 5	22.08 W/mm^3	21.97 W/mm^3	0.12 W/mm^3	0.52 %	1.00525

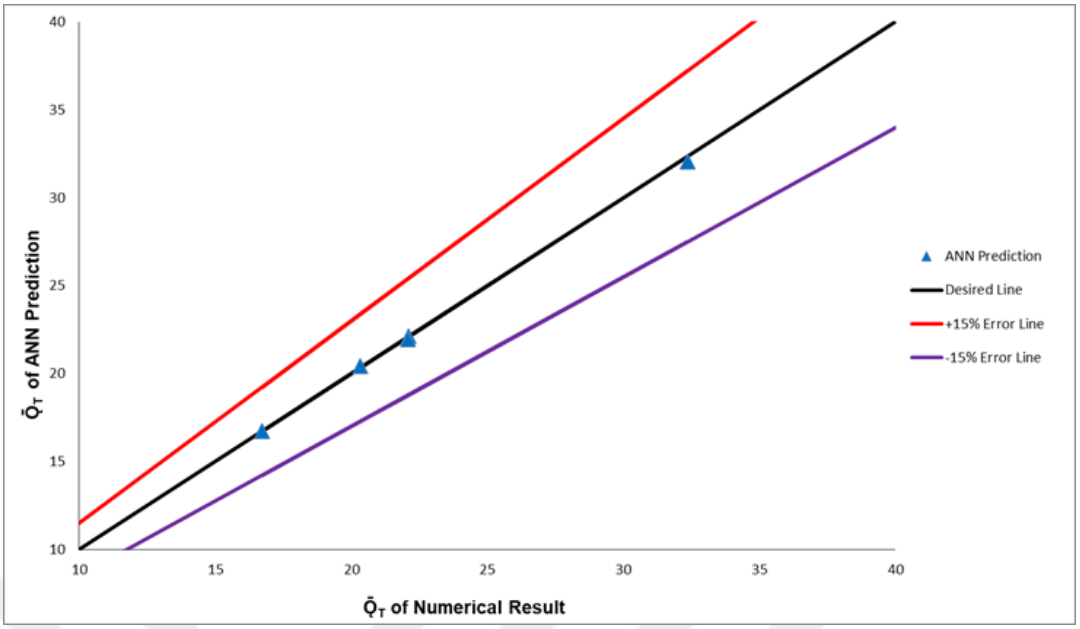


Figure 5.5 The scatter plot of the total heat transfer ($\bar{Q}_T$) per unit volume of the heat exchanger

Artificial neural network predictions are compared to numerical results for the pressure drop (ΔP) between the inlet and outlet of internal volume in Table 5.6. The maximum absolute difference in predicted values of ΔP is 0.03 Pa, with a maximum relative error of less than 2.60%. The deviation range of relative errors is 0.02 – 2.56%, and the prediction accuracy range is 0.97501- 1.02268. A scatter plot in Figure 5.6 compares numerical and ANN results for ΔP. The optimal network topology determines R, MRE, and mean absolute difference as 1.00152, 1.65% and 0.02 Pa, respectively.

Table 5.6 The comparison of results for the pressure drop (ΔP) between the inlet and outlet of internal volume

ΔP of Estimation Data	**Numerical Result**	**ANN Result**	**Absolute Difference**	**Er**	**R**
Set 1	4.14 Pa	4.13 Pa	0.01 Pa	0.24 %	0.99980
Set 2	1.34 Pa	1.31 Pa	0.03 Pa	2.19 %	1.02243
Set 3	1.13 Pa	1.14 Pa	0.01 Pa	1.25 %	0.98767
Set 4	0.74 Pa	0.73 Pa	0.02 Pa	2.22 %	1.02268
Set 5	0.80 Pa	0.83 Pa	0.02 Pa	2.56 %	0.97501

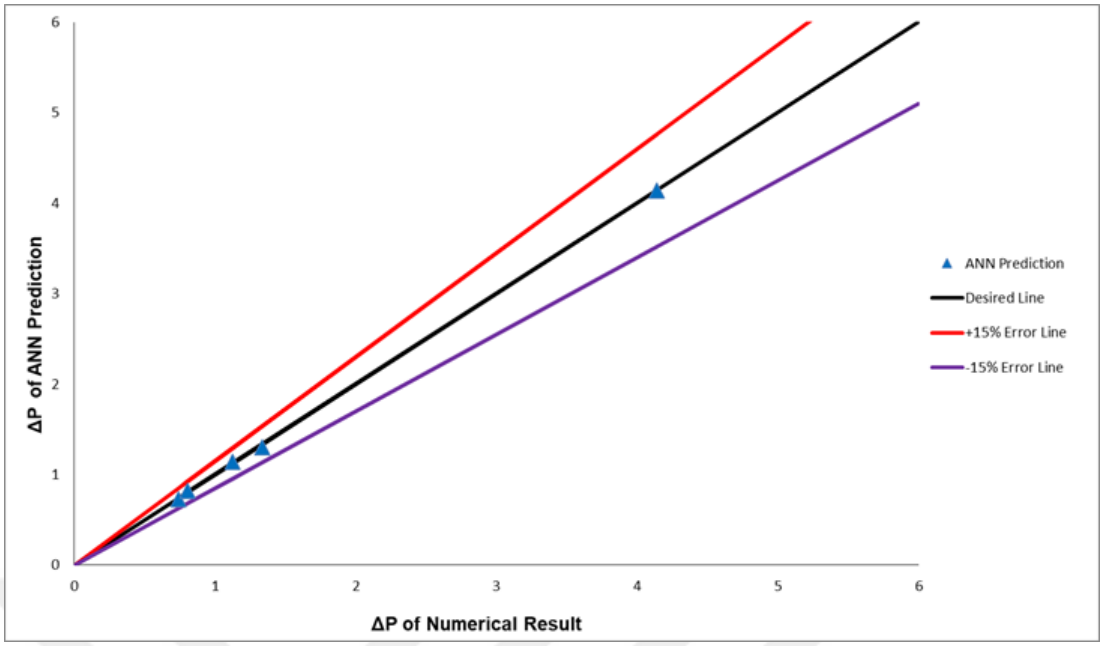


Figure 5.6 The scatter plot of the pressure drops (ΔP) between the inlet and outlet of the internal volume

The optimal values of the design case were determined in Chapter 3.4.1 using the parametric method and estimated with the selected network topology. Table 5.7 compares the ANN estimation and parametric result for the optimum design case. The maximum relative error for output values of the optimum design is less than 0.40%.

Table 5.7 Comparison of the parametric result evaluated numerically and using ANN model for best design case

Optimum Design Case	Parametric Result	ANN Estimation	Absolute Difference	Er [%]
Q_T [W]	90.00	90.01	0.01	0.01
T_{max} [°C]	122.70	122.67	0.03	0.02
$\bar{Q}_T$ [W/mm^3]	32.80	32.82	0.02	0.07
ΔP [Pa]	0.520	0.522	0.002	0.39

This study examines the effect of design variables on the output characteristics of an aluminium heat exchanger used in a condensing wall-mounted boiler. It illustrates optimal design scenarios based on criteria and demonstrates the feasibility of using artificial neural networks (ANNs) to model the finned tube heat exchanger of such boilers. An ANN structure is developed to predict various output parameters of the heat exchanger's internal volume, and the effects of selected design parameters on these output parameters are analysed using a commercial simulation program. The

resulting data is used to train and validate the ANN model, which shows to be satisfactory with an average accuracy of 1.00018 and a maximum relative error of 9.16%

This study presents a novel approach for predicting the performance of finned tube heat exchangers employed in condensing wall-mounted boilers. The method combines numerical simulation and artificial neural network techniques and has significant implications for heat exchanger design and analysis. The proposed method has the potential to enhance the design process, making it more expeditious and cost-effective and ultimately leading to improved efficiency and effectiveness in the overall heat engine system. Finally, it shows that thermal designers and engineers can use a numerical approach and ANN prediction method as a tool in the R&D process.

5.2 Optimization of the Emission and Performance Parameters of the Wall-Hang Condensing Boiler by Artificial Neural Networks Trained with Real-world Data

Reducing greenhouse gas emissions and increasing energy efficiency is becoming more urgent. The wall-hung condensing boilers significantly impact energy consumption and environmental sustainability. However, balancing minimising emissions and optimising performance in these boilers requires innovative approaches beyond traditional engineering methods. This study uses artificial neural networks trained with real-world data to improve wall-hung condensing boilers' emission and performance parameters.

In Chapter 4.3, the output parameters of performance and emissions for the whole wall-hang condensing boiler were experimentally investigated. This condensing boiler had a premix combustion unit and a stainless-steel heat exchanger. The fan speed (rpm value) and the air-gas equivalence ratio (φ) are the main parameters to determine the performance of a condensing wall hang boiler. The air-gas equivalence ratio plays a significant role in emissions (CO, NO and NO_2), and the fan speed can adjust most of the input heat load of the boiler. The gas type is also used as another design parameter.

The schematic view of the experimental setup is shown in Figure 4.11. Experimental tests were performed at a fully equipped and calibrated test rig.

The values of input parameters are given in Table 4.6. According to the variation of design parameters, sixty different design points were performed experimentally, and their results were recorded. Twenty design points were measured per one working day at the test laboratory (Figure 4.12).

Table 4.6 shows sixty design cases for five different fan speeds, six different air-gas equivalence ratios (φ) and two different gas types. The experimental results are given in Table 4.7. The table gives the input heat load (Q_c), modulation ratio (%), CO, NO and NO_2 emissions (ppm) for each design point. The bold highlighted results show the initial condition of the condensing boiler. This experimental data set is used for creating the structures of artificial neural networks.

The CO_2, CO, NO, NO_2 emissions, input load (Q_c) and output power (P_{ch}) of the condensing boiler are selected as output parameters for ANN structures. The experimental studies take so much time and have so many operating costs. Therefore, this data set was obtained within five working days. The collected real-world data sets from the experimental studies are divided into the training, and the testing sets to model the ANN for the performance of the whole condensing boiler. The data sets consist of 57 input-output pairs. While 95% of the data set was randomly assigned as the training set, the remaining 5% was used for the testing and validation of the network.

Due to the limited data set, multiple ANN structures are created with the same input parameters to estimate the output parameters of the boiler. If the six output parameters are used to be trained in the single ANN structure, the wide range of output values cannot be predicted with high accuracy.

5.2.1 The Artificial Neural Network Study for the Estimation of CO_2 Emission of the Condensing Boiler with Real-world Data

The first ANN structure is created for estimating the CO_2 emission of the condensing boiler with the real-world data set. Two different ANN configurations were carried out by using the MATLAB program. When Table 5.8 is analysed, the best configuration 3-2-1 is selected for testing, with the smallest σ=0.022143 and R=1.00021 together, and the maximum relative error is about 3.71%. The ANN structure of the CO_2 emission is well-trained in the second trial. The selected architecture of the ANN has three layers and is schematically illustrated with the names of input and output parameters in Figure 5.7. There is only one hidden layer and two neurons.

Table 5.8 Comparison of errors by different ANN configurations of CO_2 emission

Configuration	**Train error**		**Test error**	
	Er [%]	**RMS**	**R**	**σ**
3-1-1	4.01	0.00672	0.99991	0.022945
3-2-1	3.71	0.00637	1.00021	0.022143
Note: The error is the maximum value among the errors of the two output variables.				

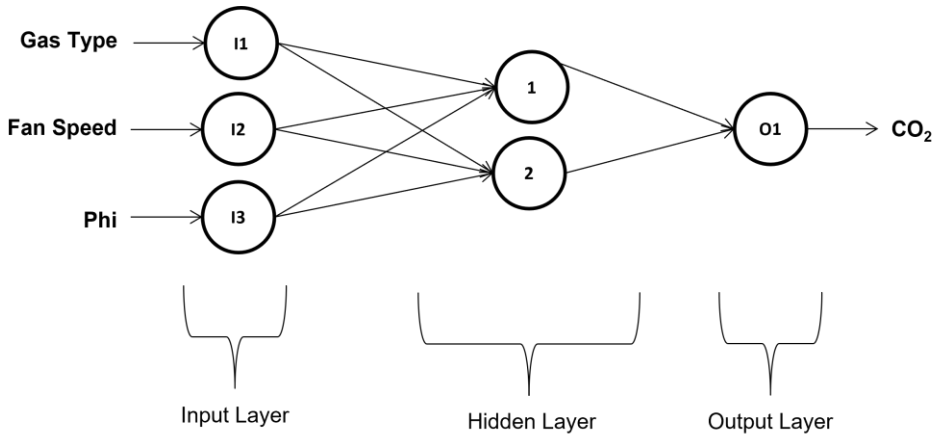


Figure 5.7 The selected structure for ANN modelling of the CO_2 emission

5.2.2 The Artificial Neural Network Study for the Estimation of CO Emission of the Condensing Boiler with Real-world Data

The second ANN structure is created for estimating the CO emission of the condensing boiler with the real-world data set. However, current input and output values cannot provide adequate training. The range of CO emission varies between 0 to 679 ppm, and there are only 57 data sets to train and test the ANN. Therefore, data normalisation is applied to the data sets to train the CO emission. One of the most common tools is used to obtain better results with data normalisation. There are many types of data normalisation. Data normalisation can also accelerate training time by starting the training process for each feature within the same scale (Priddy and Keller, 2005). Statistical or Z-core Normalization technique is used for that.

$$x_i' = \left[\frac{(x_i - \mu_i)}{\sigma_i}\right] \tag{5.5}$$

Figure 5.8 shows the diagram of decision flow when the normalisation method is needed to apply to the data set. If the size of the data set is not big enough to estimate the complex input and output parameters, the normalisation methods are applied to the data set. Firstly, the ANN is created simple-structured, and learning rules are defined as a starting point for training by trial and error. Suppose the network performance parameters do not reach the defined targets during the training and validation phases. In that case, the backpropagation algorithm changes the parameters of learning rules, or the new network structure is created more complex to reach the target values. Ultimately, the network structures and learning rules become more complex, and ANN models cannot be trained. After normalisation, the normalization methods are applied to a data set, and the data and learning processing are reestablished.

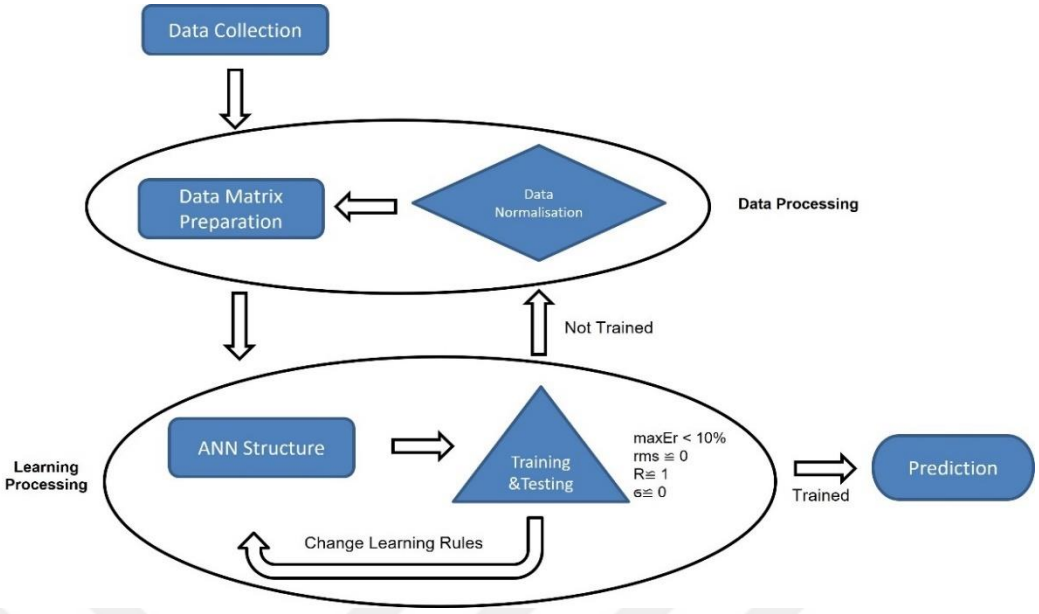


Figure 5.8 The decision flow diagram of the usage of the normalisation method to the data set

According to Equation 5.5, the data sets of the CO emission are normalised, and ANN configurations are carried out. When Table 5.9 is analysed, the best configuration 3-6-3-1 is selected for testing, with the smallest σ=0.010765 and R=0.99993 together, and the maximum relative error is about 0.09%. The ANN structure of the CO emission is well-trained with the data normalisation technique. The selected architecture of the ANN has four layers and is schematically illustrated with the names of input and output parameters in Figure 5.9. There are only two hidden layers, six and three neurons.

Table 5.9 Comparison of errors by different ANN configurations of CO emission

Configuration	**Train error**		**Test error**	
	Er [%]	**RMS**	**R**	**σ**
3-1-1	91127.98	17937.01	0.79844	0.614399
3-1-1 (z-core)	59.29	77.36000	0.43583	5.153342
3-2-1 (z-core)	44.99	0.392439	0.77215	1.795942
3-3-1 (z-core)	38.39	0.320067	0.91256	0.816366
3_3_1_1 (z-core)	24.05	0.777427	1.00001	0.157249
3_3_3_1 (z-core)	16.63	1.601183	0.97032	0.128806
3_6_3_1 (z-core)	0.09	0.011060	0.99993	0.010765
Note: The error is the maximum value among the errors of the two output variables.				

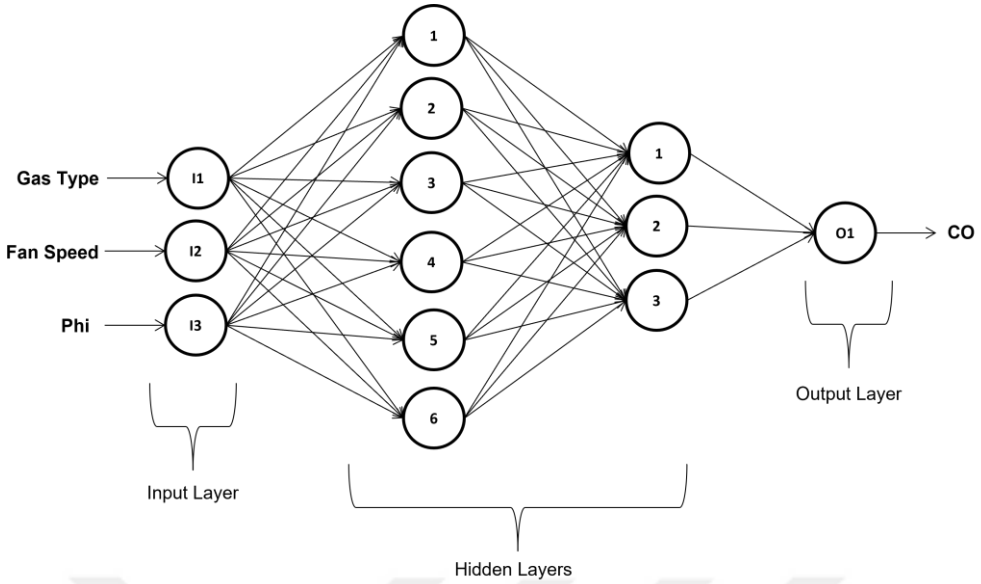


Figure 5.9 The selected structure for ANN modelling of the CO emission

5.2.3 The Artificial Neural Network Study for the Estimation of NO Emission of the Condensing Boiler with Real-world Data

The third ANN structure is created for estimating the NO emission of the condensing boiler with the real-world data set. When Table 5.10 is analysed, the best configuration 3-6-1 is selected for testing, with the smallest σ=0.036534 and R=1.00652 together and the maximum relative error is about 8.82%. The ANN structure of the NO emission is well-trained in the fourth trial. The selected architecture of the ANN has three layers and is schematically illustrated with the names of input and output parameters in Figure 5.10. There is only one hidden layer and six neurons.

Table 5.10 Comparison of errors by different ANN configurations of NO emission

Configuration	**Train error**		**Test error**	
	Er [%]	**RMS**	**R**	**σ**
3-2-1	202.76	0.400633	0.99727	0.277436
3-3-1	315.72	0.566129	0.98767	0.276772
3-4-1	126.17	0.298566	0.71033	1.711877
3-6-1	8.82	0.036534	1.00652	0.036550
Note: The error is the maximum value among the errors of the two output variables.				

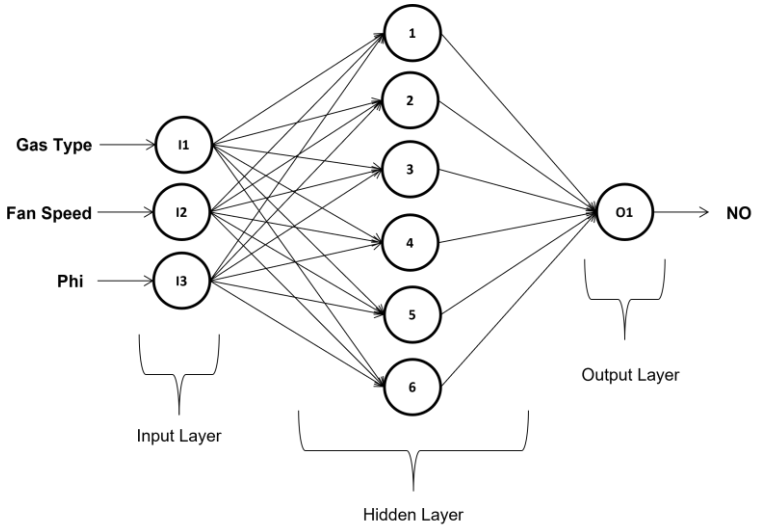


Figure 5.10 The selected structure for ANN modelling of the NO emission

5.2.4 The Artificial Neural Network Study for The Estimation of NO_2 Emission of The Condensing Boiler with Real-world Data

The fourth ANN structure is created for estimating the NO_2 emission of the condensing boiler with the real-world data set. Eight different ANN configurations are carried out. When Table 5.11 is analysed, the best configuration 3-9-6-3-1 is selected for testing, with the smallest σ=0.010490 and R=0.99888 together, and the maximum relative error is about 6.36%. The ANN structure of the NO_2 emission is well-trained in the eighth trial. The selected architecture of the ANN has five layers and is schematically illustrated with the names of input and output parameters in Figure 5.11.

Table 5.11 Comparison of errors by different ANN configurations of NO_2 emission

Configuration	**Train error**		**Test error**	
	Er [%]	**RMS**	**R**	**σ**
3-1-1	33.94	0.137677	0.99755	0.141610
3-2-1	32.04	0.130201	1.00174	0.135874
3-3-1	31.42	0.099934	1.00032	0.099361
3-4-1	29.40	0.102598	1.00225	0.102642
3-6-1	23.40	0.077962	1.00466	0.078263
3-3-1-1	20.41	0.086132	0.99735	0.087011
3-6-1-1	17.08	0.067835	0.99628	0.068626
3-9-6-3-1	6.36	0.010936	0.99888	0.010490
Note: The error is the maximum value among the errors of the two output variables.				

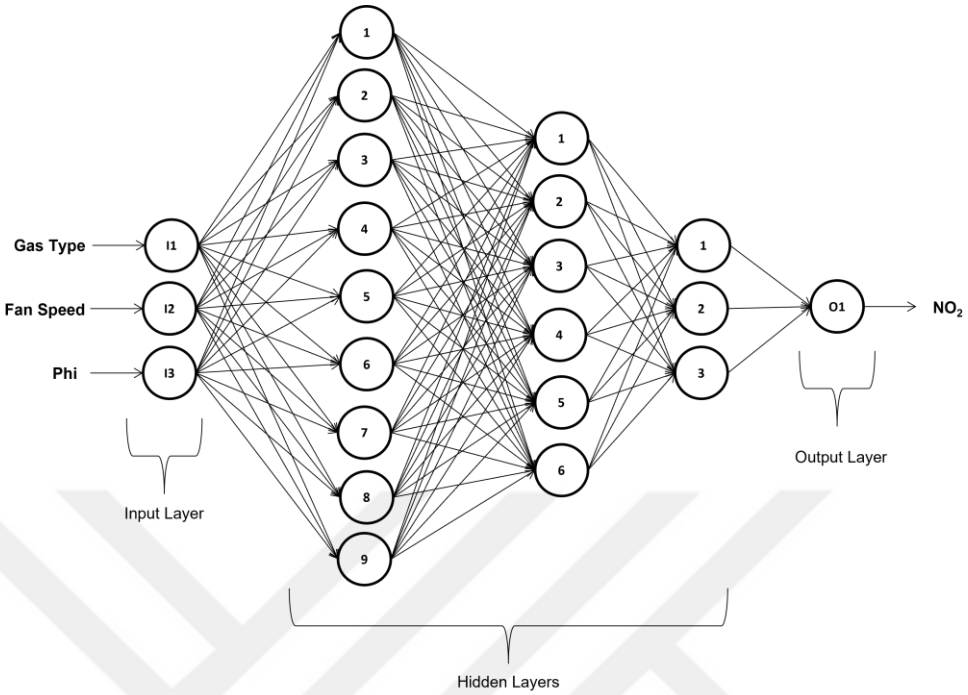


Figure 5.11 The selected structure for ANN modelling of the NO_2 emission

5.2.5 The Artificial Neural Network Study for the Estimation of Q_c and P_{ch} Performance of the Condensing Boiler with Real-world Data

The last ANN structure of this reporting term is created for estimating the Q_c and P_{ch} of the condensing boiler with the real-world data set. Three different ANN configurations are carried out. When Table 5.12 is analysed, the best configuration 3-3-2 is selected for testing, with the smallest σ=0.011791 and R=1.00037 together, and the maximum relative error is about 5.66%. The ANN structure of the Q_c and P_{ch} is well-trained in the third trial. The selected architecture of the ANN has three layers and is schematically illustrated with the names of input and output parameters in Figure 5.12.

Table 5.12 Comparison of errors by different ANN configurations of Q_c and P_{ch}

Configuration	Train error		Test error	
	Er %	RMS	R	σ
3-1-2	23.80	0.068030	1.00214	0.063972
3-2-2	12.13	0.028895	1.00080	0.027975
3-3-2	5.66	0.011892	1.00037	0.011791
Note: The error is the maximum value among the errors of the two output variables.				

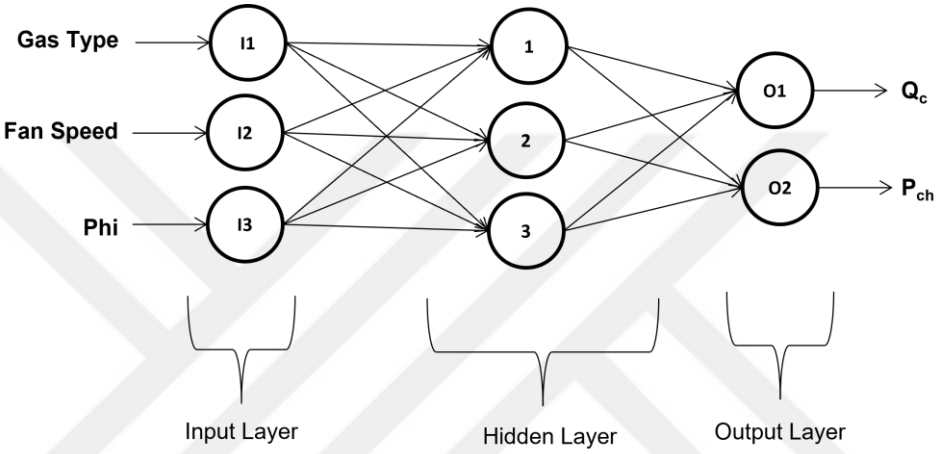


Figure 5.12 The selected structure for ANN modelling of the Q_c and P_{ch}

Different artificial neural network structures are created for each output parameter except the Q_c and P_{ch}. Five artificial neural networks train six output parameters with the same input parameters. These networks are developed and operated as a cascade system (Figure 5.13). All networks can individually predict their output/outputs in the common cascade system. According to Figure 5.14, the maximum relative error is about 8.82%, with most being less than 2% at the training phase for the five artificial neural networks' structures.

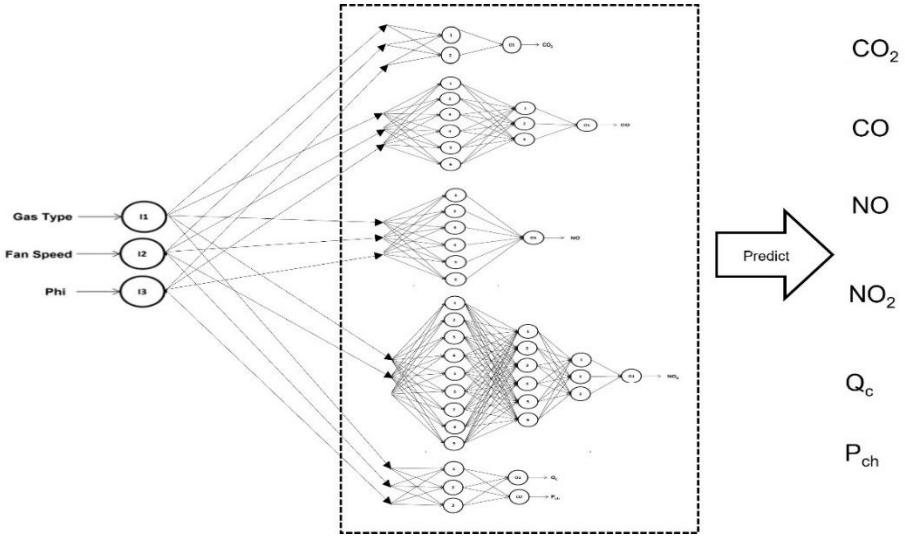


Figure 5.13 The cascade structure for ANN modelling for the wall-hang condensing boiler

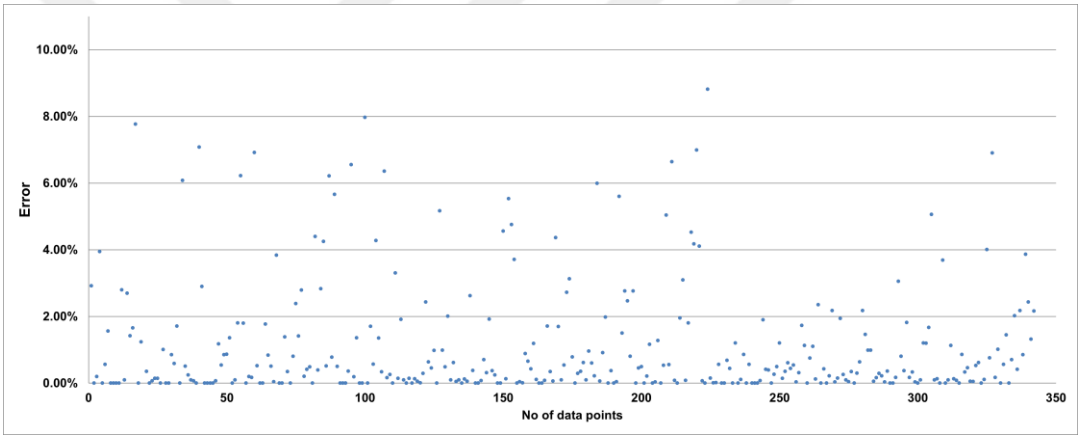


Figure 5.14 The scatter plot of relative error at the training process for the cascade operation of artificial neural networks

5.2.6 The Results and Discussion of the Cascade Structure of Artificial Neural Network Study for the Condensing Boiler with Real-world Data

The ANN method aims to quickly estimate the output parameters of the condensing wall hang boilers.

After the training and validation of the networks, the developed cascade ANN structure is ready to use to estimate new outputs for different design cases. Three design cases are not used for training the network process. So, the networks know

those data sets never. The input parameters values of estimation data are shown in Table 5.13

Table 5.13 The input parameters and values of estimation data sets

Estimation Data	Gas Type	Fan Speed [rpm]	φ
Set 1	NG	5500	0.85
Set 2	NG	3500	0.90
Set 3	G20	2400	0.75

Table 5.14 compares ANN prediction and experimental results for CO_2 emissions. The maximum absolute difference is 0.36%, and the maximum relative error is less than 0.42%. It can be estimated that the relative error values are in the range of 0.12 – 0.41%, and the accuracy of prediction is in the range of 0.99594 - 1.00363. The ANN model can estimate CO_2 in the average accuracy of prediction (R) of 1.00024, the mean relative error (MRE) of 0.29% and the mean absolute difference of 0.03%.

Table 5.14 The comparison of results for the CO_2 emissions

Estimation Data	Experimental Result [%]	ANN Result [%]	Absolute Difference [%]	Er [%]	R
Set 1	9.88	9.92	0.04	0.41	0.99594
Set 2	10.53	10.52	0.01	0.12	1.00116
Set 3	8.54	8.51	0.03	0.36	1.00363

Table 5.15 compares ANN prediction and experimental results for CO emissions. The maximum absolute difference is 17.48 ppm, and the maximum relative error is less than 6.84%. It can be estimated that the relative error values are in the range of 4.90 – 6.83 %, and the accuracy of prediction is in the range of 0.95327 - 1.07330. The ANN model can estimate CO in the average accuracy of prediction (R) of 1.03189, the mean relative error (MRE) of 6.07 % and the mean absolute difference of 10.15 ppm.

Table 5.15 The comparison of results for the CO emissions

Estimation Data	Experimental Result [ppm]	ANN Result [ppm]	Absolute Difference [ppm]	Er [%]	R
Set 1	252.9	270.4	17.48	6.46	1.06910
Set 2	270.7	258.0	12.65	4.90	0.95327
Set 3	4.2	4.5	0.31	6.83	1.07330

Table 5.16 compares ANN prediction and experimental results for NO emissions. The maximum absolute difference is 2.20 ppm, and the maximum relative error is less than 5.18 %. It can be estimated that the relative error values are in the range of 2.73 – 5.17 %, and the accuracy of prediction is in the range of 0.95085 - 1.03788. The ANN model can estimate NO in the average accuracy of prediction (R) of 1.00561, the mean relative error (MRE) of 3.85 % and the mean absolute difference of 1.47 ppm.

Table 5.16 The comparison of results for the NO emissions

Estimation Data	Experimental Result [ppm]	ANN Result [ppm]	Absolute Difference [ppm]	Er [%]	R
Set 1	33.75	35.49	1.74	5.17	0.95085
Set 2	80.39	78.19	2.20	2.73	1.02810
Set 3	12.92	12.45	0.47	3.65	1.03788

Table 5.17 compares ANN prediction and experimental results for NO_2 emissions. The maximum absolute difference is 0.88 ppm, and the maximum relative error is less than 3.37 %. It can be estimated that the relative error values are in the range of 1.21 – 3.36 %, and the accuracy of prediction is in the range of 0.98369 - 1.03477. The ANN model can estimate NO_2 in the average accuracy of prediction (R) of 1.01022, the mean relative error (MRE) of 2.07 % and the mean absolute difference of 0.42 ppm.

Table 5.17 The comparison of results for the NO_2 emissions

Estimation Data	Experimental Result [ppm]	ANN Result [ppm]	Absolute Difference [ppm]	Er [%]	R
Set 1	16.71	16.99	0.28	1.66	0.98369
Set 2	26.10	25.22	0.88	3.36	1.03477
Set 3	8.28	8.18	0.10	1.21	1.01220

Table 5.18 shows the comparison of ANN prediction and experimental results for Q_c. The maximum absolute difference is 0.23 kW, and the maximum relative error is less than 2.26 %. It can be estimated that the relative error values are in the range of 0.27 – 2.25%, and the accuracy of prediction is in the range of 0.99280 - 1.02305. The ANN model can estimate Q_c in the average accuracy of prediction (R) of 1.00439, the mean relative error (MRE) of 1.08 % and the mean absolute difference of 0.14 kW.

Table 5.18 The comparison of results for the Q_c

Estimation Data	Experimental Result [kW]	ANN Result [kW]	Absolute Difference [kW]	Er [%]	R
Set 1	27.25	27.32	0.07	0.27	0.99733
Set 2	17.67	17.80	0.13	0.73	0.99280
Set 3	10.24	10.01	0.23	2.25	1.02305

Table 5.19 shows the comparison of ANN prediction and experimental results for P_{ch}. The maximum absolute difference is 0.13 kW, and the maximum relative error is less than 1.41 %. It can be estimated that the relative error values are in the range of 0.30 – 1.40%, and the accuracy of prediction is in the range of 0.99649 - 1.01419. The ANN model can estimate P_{ch} in the average accuracy of prediction (R) of 1.00256, the mean relative error (MRE) of 0.68 % and the mean absolute difference of 0.09 kW.

Table 5.19 The comparison of results for the P_{ch}

Estimation Data	Experimental Result [kW]	ANN Result [kW]	Absolute Difference [kW]	Er [%]	R
Set 1	23.48	23.55	0.07	0.30	0.99699
Set 2	15.54	15.59	0.06	0.35	0.99649
Set 3	9.01	8.88	0.13	1.40	1.01419

CHAPTER SIX
CONCLUSIONS

The thesis investigated the effects of the design parameters of the wall-hang condensing boiler and its essential components, especially the heat engine and heat exchangers, on thermal performance, flow characteristics of flue gas and flue gas emissions. Within the scope of the thesis, the performance and emission parameters for the condensing boiler and components were investigated in detail by experimental, numerical, and artificial neural network methods. The main aim of this study was to determine the design parameters of the whole condensing boiler and its heat exchanger and to optimized them to reach the target values and to develop a new condensing boiler in order to maximise performance and minimise the flue gas emission according to the standards and regulations.

Firstly, the literature survey was evaluated for the condensing boilers and their essential components. The application of condensing boilers and their main components were explained in detail. The working principle and boundary diagrams were determined, and the mathematics of computational fluid dynamics and heat transfer were given for numerical simulations.

In the numerical investigation chapter, the internal air volume of the combustion unit of the condensing unit was modelled numerically at first. The flow and temperature distributions of the flue gas (modelled as air domain) were investigated in detail. According to the first study result, the combustion unit's main components (heat exchanger type, baffle design, etc.) affected the flue gas movement inside the heat engine. In the second numerical study, the fin length and fin thickness of the aluminium finned tube heat exchanger used in the combustion units' condensing zone were chosen as the design parameters. The effects of the determined design parameters on the pressure drop and flow characteristics in the combustion unit were investigated in detail using the ANSYS program. The third numerical study investigated the effects of modelling the flue gas domain as air or combustible gas mixture on the results of numerical analyses. Ans also, experimental studies verified the numerical flue gas and air domain models using controlled experimental setups and control volumes. In this way, it was found that the flue gas domain should be modelled as the fluid type for the

numerical studies of the combustion units used in the condensing boiler and heating appliances. After validating the flue gas domain used in numerical analyses of a condensing boiler's combustion unit or heat engine, the impact of heat exchanger design parameters on heat engine performance was investigated in the fourth numerical study. The input design parameters of the finned tube heat exchanger were selected as fin height, thickness, and space to determine the total heat transfer on the inner surface of the tube, the maximum temperature on the fins, the total heat transfer per unit volume of the heat exchanger, and the pressure drop between the inlet and outlet of the internal volume. The study created 350 design cases to complete the parametric study with numerical results. The numerical results were also used for the artificial neural network modelling. The design cases were found to optimize the outputs according to the target criteria. The last numerical study was related to determining the effect of the heat exchanger designs on thermal performance with different numbers of internal channels of the finned tube heat exchanger. After the numerical simulations, the eight channels model was manufactured and compared to the real results with the base single-channel model.

In the next section, experimental studies were presented. The first experimental study clarified and validated the modelling of the fluid domain as air or flue gas for the combustion unit of a condensing boiler with a heat recovery device. Two basic control volumes were modelled and prototyped for the internal flue gas. The experimental setups were created with these control volumes, and performed the tests with air and flue gas domains. Experimental results showed that when the fluid was modelled as air and flue gas for the close volumetric flow rates, there were huge differences in pressure drops. In the studies carried out with air and the flue gas in the control volume made of perforated stainless plates, different pressure drops close to 3 times were obtained for the same volumetric flow conditions. The second experimental study was performed to clarify the effect of the heat exchanger's internal channel on the condensing boiler's thermal performance. Therefore, two heat engines were designed and prototyped with heat exchangers manufactured with single and eight internal channels. These heat engines had the same outer dimensions. Only heat exchangers were different for both heat engines. As a result, 63% more output power and 92.4% seasonal efficiency were gained with the same heat engine volume used

with numerical simulations. In the third experimental study, the whole 23 kW wall-hang boiler was experimentally investigated to evaluate the performance and emissions output parameters with real-world data. Each design parameter was evaluated in detail on the boiler's performance and CO, NO, and NO_x emissions. The optimum working points were determined for the 23 kW wall-hang condensing boiler. In the last experimental study, a new 153 kW wall hang boiler was developed and manufactured according to the results of numerical and experimental studies presented in this thesis. The development tests were given in detail. Finally, a few trials have determined the optimum parameters of the combustion values that provide the 153 kW maximum input load with 31.45 mg/kWh NOx emission. The prototype of the high-capacity and low-emission wall-hang condensing boiler targeted within the scope of this thesis has been successfully completed.

In the last section, the artificial neural networks studies were presented. Three hundred fifty design cases were created according to the design parameters of the finned tube heat exchanger used in the condensing boiler and simulated numerically. The numerical results of these design cases were used in artificial neural network modelling in the first ANN study. The selected design parameters of the aluminium heat exchanger were fin height (h_f), fin thickness (t_f), and fin spacing (s). Total heat transfer (Q_T) on the inner surface of the tube, the maximum temperature on the fins (T_{max}), the pressure drop (ΔP) between the inlet and outlet of internal volume and the total heat transfer ($\bar{Q}_T$) per unit volume of the heat exchanger were also used as output parameters for ANN modelling. The best-created ANN topology, 3-6-12-8-4, was trained with σ=0.01285, R=1.00018, and a maximum relative error of 9.16%. The outputs of the optimum design case were sensitively estimated with an average accuracy of 1.00018 and a maximum relative error of 9.16%. The second ANN study was related to estimating the performance and emissions of condensing boilers with real-world experimental data. The new cascade training method was applied due to the limited data set. In the end, the emissions were estimated under the maximum relative error of 7%.

In future work, real-world data sets can be collected from IoT devices, and these data can be processed and monitored. The real-time control systems can be developed

for operating condensing boilers. The emissions and performance of boilers can always be kept at desired values.

REFERENCES

Alimoradi, A., Olfati, M., & Maghareh, M. (2017). Numerical investigation of heat transfer intensification in shell and helically coiled finned tube heat exchangers and design optimization. *Chemical Engineering and Processing: Process Intensification, 121*, 125-143. https://doi.org/10.1016/j.cep.2017.08.0

Antonescu, N., & Stanescu, P.D. (2017). Computational model for a consensing boiler with finned tubes heat exchanger. *Energy Procedia, 112*, 555-562. https://doi:10.1016/j.egypro.2017.03.1116.

Balanescu D.T., & Homutescu V.M. (2017). Experimental study on the combustion system optimization in the case of a 36 kW condensing boiler. Procedia Engineering, 181, 706-711. https://doi:10.1016/j.proeng.2017.02.453

Balanescu D.T., & Homutescu V.M. (2018). Experimental investigation on performance of a condensing boiler and economic evaluation in real operating conditions. *Applied Thermal Engineering, 143*, 48-58. https://doi.org/10.1016/j.applthermaleng.2018.07.082

Bilirgen, H., Dunbar, S., & Levy E.K. (2013). Numerical modelling of finned heat exchangers. *Applied Thermal Engineering, 61*: 278-288. https://doi:10.1016/j.applthermaleng.2013.08.002

Blazek, J. (2001). *Computational fluid dynamics: Principles and applications*. (1st ed.). Netherlands: Elsevier Science Ltd.

Cao, W., & You, X. (2017) Effects of Wall Fins Patterns on the Flue Gas Performance of Condensing Heat Exchanger, Procedia Engineering, 205, 2281 - 2288. https://doi.org/10.1016/j.proeng.2017.10.081

Cheng Y., Huang Y., Pang B., & Zhang W. (2018). ThermalNet: A deep reinforcement learning-based combustion optimization system for coal-fired boiler. *Engineering Applications of Artificial Intelligence. 74,* 303-311. https://doi:10.1016/j.engappai.2018.07.003

Cumbul A.Y., (2018). *Evaluation of energy efficiency of a power-plant using energy analysis* [Unpublished master dissertation]. University of Dokuz Eylül.

Dhumal, G.S, & Havaldar, S.N. (2021). Numerical investigation of heat exchanger with inserted twisted tape inside and helical fins on outside pipe surface.*Materials Today: Proceedings,46*,2557-2563. https://doi.org/10.1016/j.matpr.2021.01.837

Du, Y.J., & Wang, C.C. (2000). An experimental study of the air side performance of superslit fin and tube heat exchangers. International Journal of Heat and Mass Transfer, 43, 4475-4482. https://doi.org/10.1016/S0017-9310(00)00082-X

Duan, L., Ling, X., Peng, H. (2018). Flowand heat transfer characteristics of a double-tube structure internal finned tube with blossom shape internal fins. *Applied Thermal Engineering, 128,* 1102-1115. https://doi.org/10.1016/j.applthermaleng.2017.09.026

Ecodesign and Energy Labelling, (2019). Ecodesign and energy labelling directive 2009/125/EC and Regulation (EU) 2017/1369, European Committee for Standardization.

EN 15502 -1:2012+A1:2015, (2015). Gas-fired heating boilers Part 1: General requirements and tests-TC109 (Issue February), European Committee for Standardization.

Energy-related Products, (2009). The energy-related products directive (ErP) 2009/125/EC, European Committee for Standardization.

Gas Appliances Regulation, (2016). Legal framework: Regulation (EU) 2016 on appliances burning gaseous fuels, European Committee for Standardization.

Giannetti N., Redoo M.A., Sholahudin, Jeong J., Yamaguchi S., Saito K., & Kim H. (2020). Prediction of two-phase flow distribution in microchannel heat exchangers using artificial neural network. *International Journal of Refrigeration. 111,* 53-63. https://doi:10.1016/j.ijrefrig.2019.11.028

Incropera, F.P., Dewitt, D.P. (1996). Fundamentals of Heat and Mass Transfer, John

Wiley & Sons.

Iqbal, Z., Syed, K.S., & Ishaq M. (2015). Fin design for conjugate heat transfer optimization in double pipe. *International Journal of Thermal Sciences, 94,* 242-258. https://doi.org/10.1016/j.ijthermalsci.2015.03.011

Joo, Y., Kim, S.J. (2016). Thermal optimization of vertically oriented, internally finned tubes in natural convection. *International Journal of Heat and Mass Transfer, 93,* 991-999. https://doi.org/10.1016/j.ijheatmasstransfer.2015.10.034

Kamsuwan C., Wang X., Seng L.P., Xian C.K., Piemjaiswang R., Piumsomboon P., Pratumwal Y., Otarawanna S., & Chalermsinsuwan B., (2023). Simulation of nanofluid micro-channel heat exchanger using computational fluid dynamics integrated with artificial neural network. *Energy Reports, 9,* 239-247. https://doi:10.1016/j.egyr.2022.10.412

Karaaslan, S., Çalışır T., Yılmazoğlu M.Z., Yılmaz T.O., & Başkaya Ş. (2013). *19. Ulusal Isı Bilimi ve Tekniği Kongresi*, 732-737.

Keawkamrop, T., Asirvatham, G.D., Dalkılıç, A.S., Ahn, H.S., Mahian, O., & Wongwises, S. (2021). An experimental investigation of the air-side performance of crimped spiral fin-and-tube heat exchangers with a small tube diameter. International Journal of Heat and Mass Transfer, 178, 121571 https://doi.org/10.1016/j.ijheatmasstransfer.2021.121571

Kiatpachai, P., Keawkamrop, T., Asirvatham, L.G., Mesgarpour, M., Dalkılıç, A.S., Ahn, H.S., Mahian, O., & Wongwises, S. (2022). An experimental study of the air-side performance of a novel louver spiral fin-and-tube heat exchanger. *Alexandria Engineering Journal, 61,* 9811-9818. https://doi.org/10.1016/j.aej.2022.02.056

Kim N.H., Youn B., Webb R.L. (1999). Air side heat transfer and friction correlations for plain fin and tube heat exchangers with staggered tube arrangements, ASME. Journal of Heat Transfer, 121(3), 662-667. https://doi.org/10.1115/1.2826030

Kim, D.K.. (2016). Thermal optimization of internally finned tube with variable fin thickness. *Applied Thermal Engineering, 102,* 1250-1261. https://doi.org/10.1016/j.applthermaleng.2016.04.060

Kreith K. (2000). The CrcHandbook of Thermal Engineering. Crc Press, Boca Raton.

Lee, S., Kum, S.M. M., & Lee, C.E. E. (2011a). An experimental study of a cylindrical multi-hole premixed burner for the development of a condensing gas boiler. Energy, 36(7), 4150–4157. https://doi.org/10.1016/j.energy.2011.04.029

Lee, S., Kum, S.M., & Lee, C.E. (2011b). Performances of a heat exchanger and pilot boiler for the development of a condensing gas boiler. *Energy, 36(7),* 3945–3951. https://doi.org/10.1016/ j.energy.2011.05.018

Maghsoudali, Y., Rastegarkoutenaei, A., Sahami, M., & Bandpy, M.G. (2023). Experimental investigating the thermal and hydraulic performance of heat exchangers with helix wire finned tube. Applied Thermal Engineering, 231, 1359-4311. https://doi.org/10.1016/j.applthermaleng.2023.120919

Mohanraj M., Jayaraj S., & Muraleedharan C. (2015). Applications of artificial neural networks for thermal analysis of heat exchangers – A review. *International Journal of Thermal Sciences. 90,* 150-172. https://doi:10.1016/j.ijthermalsci.2014.11.030

NASA report SP-3001. (2018, June 22). Computer Program for Calculation of Complex Chemical Equilibrium Compositions and Applications. https://ntrs.nasa.gov/archive/nasa/casi.ntrs.nasa.gov/19630013835.pdf

Pacheco-Vega A., Diaz G., Sen M., Yang K. T., & Mcclain R. L. (2001). Heat rate predictions in humid air-water heat exchangers using correlations and neural networks. Journal Heat Transfer. 123, 348-354. https://doi:10.1115/1.1351167

Perrotin T., & Clodic D., (2003). Fin efficiency calculation in enhanced fin and tube heat exchanger in dry conditions. 21st International Congress of Refrigeration: Serving the Needs of Mankind. ISBN: 2913149324

Priddy, K.L., Keller, P.E. (2005). Artificial neural networks: an introduction. SPIE Press. ISBN 9780819459879

Satyavada, H., & Baldi, S. (2018). Monitoring energy efficiency of condensing boilers via hybrid first-principle modelling and estimation. *Energy.142*, 121-129. https://doi: 10.1016/j.energy.2017.09.124

Seban, R.A., & McLaughlin, E.F. (1963). Heat transfer in tube coils with laminar and turbulent flow. *International Journal of Heat and Mass Transfer. 6,* 387-395. https://doi:10.1016/0017-9310(63)90100-5

Shang Z. (2005). Application of artificial intelligence CFD based on neural network in vapor-water two-phase flow. *Engineering Applications of Artificial Intelligence. 18,* 663-671. https://doi: 10.1016/j.engappai.2005.01.007

Singh V., Aute V., & Radermacher R. (2009). A heat exchanger model for air-to refrigerant fin-and-tube heat exchanger with arbitrary fin sheet. *International Journal of Refrigeration. 32,* 1724-1735. https://doi:10.1016/j.ijrefrig.2009.05.011

Specchia, S., & Toniato, G. (2009). Natural gas combustion catalysts for environmental-friendly domestic burners. Catalysis Today, 147(SUPPL.), S99–S106. https://doi.org/10.1016/j.cattod.2009.07.033

Ramirez, R.A., & Taglioni, J.A. (2023). Parametric analysis based on energy and exergy balances of a condensing boiler. *Journal of Mechanical Science and Technology, 37,* 1463-1471. https://10.1007/s12206-023-0232-0

Riello. (2023a, September 01). *The wall-hang condensing boiler*. https://www.riello.com/north-america/news/products/riello-high-efficiency-wall-hung-boilers

Riello. (2023b, September 01). *The floor-standing condensing boiler*. https://www.riello.com/north-america/products/commercial-boilers?range=42BJHLSNRF

Rostami, A.K., & Ganji., D.D. (2023). Selecting superior fin geometry among four suggested geometries for shell and helically coiled finned tube heat exchangers with numerical simulation and experimental validation, Results in Engineering, 17, 100867. https://doi.org/10.1016/j.rineng.2022.100867

Tutar, M., & Akkoca, A. (2004). Numerical analysis of fluid flow and heat transfer characteristics in three-dimensional plate fin and tube heat exchanger. *Numerical Heat Transfer, Part A: Applications, 46:3*, 301-321. https://doi:10.1080/10407780490474762

Türkeri A., (2007). Bireysel ve merkezi ısıtma sistemlerinin tanıtımı ve karşılaştırılması. 8. Ulusal Tesisat Mühendisliği Kongresi, 181–188.

Vidyadhar H. I., Mahesh S., Malpani R., Sapre M., & Kulkarni A. J. (2019). Adaptive range genetic algorithm: A hybrid optimization approach and its application in the design and economic optimization of shell-and-tube heat exchanger. *Engineering Applications of Artificial Intelligence*, *85*, 444-461. https://doi:10.1016/j.engappai.2019.07.001

Wais, P. (2010). Fluid flow consideration in fin-tube heat exchanger optimization. *Archives of Thermodynamics*, *31*, 87–104. doi:10.2478/v10173-010-0016-7

Wang. B.X. (2000). Heat Transfer Science and Technology, Higher Education Press.

Wang C.C., Lee W.S., & Sheu W.J. (2001). A comparative study of compact enhanced fin and tube heat exchangers. International Journal *of Heat and Mass Transfer, 44*, 3565-3573. https://doi.org/10.1016/S0017-9310(01)00011-4

Wang, Q.W., Lin, M., & Zeng M. (2009). Effect of lateral fin profiles on turbulent flow and heat transfer performance of internally finned tubes. *Applied Thermal Engineering, 29,* 3006-3013 https://doi.org/10.1016/j.applthermaleng.2009.03.016

Wu Z.G., Zhang J.Z., Tao Y.B., He Y.L., & Tao W.Q. (2008). Application of artificial neural network method for performance prediction of gas cooler in a CO_2 heat pump. International Journal of Heat Mass Transfer. 51, 5459-5464.

https://doi:10.1016/j.ijheatmasstransfer.2008.03.009

Xie C., Yan G., Ma Q., Elmasry Y., Singh P.K., Algelany A.M., & Wae-hayee M. (2022). Flow and heat transfer optimization of a fin-tube heat exchanger with vortex generators using response surface methodology and artificial neural network. *Case Studies in Thermal Engineering, 39,* 102445. https://doi:10.1016/j.csite.2022.102445

Yılmaz, S., Kumlutaş, D., Yücekaya, U.A., & Cumbul, A.Y. (2021). Prediction of the equilibrium compositions in the combustion products of a domestic boiler. *Energy, 233,* 121-123. https://doi: 10.1016/j.energy.2021.121123

Zhang, T. H., Liu, F. G., & You, X. Y. (2014). Optimization of gas mixing system of premixed burner based on CFD analysis. *Energy Conversion and Management, 85,* 131–139. https://doi.org/10.1016/j.enconman.2014.05.055

Zhang T., Chen L., & Wang J. (2023). Multi-objective optimization of elliptical tube fin heat exchangers based on neural networks and genetic algorithm. *Energy, 269,* 126729. https://doi:10.1016/j.energy.2023.126729

Zoebiry N., & Humfeld K.D. (2021). A physics-informed machine learning approach for solving heat transfer equation in advanced manufacturing and engineering applications. Engineering Applications of Artificial Intelligence. 101: 104232. https://doi:10.1016/j.engappai.2021.104232